Investigation of the whole-brain effect of hippocampal deep brain stimulation using fMRI

Julie Ottoy

Supervisors: Prof. dr. Roel Van Holen, Prof. Christian Vanhove

Counsellors: Ir. Nathalie Van Den Berge, Dr. ir. Vincent Keereman (UGent), Dr. ir. Pieter van Mierlo

Master's dissertation submitted in order to obtain the academic degree of Master of Science in Biomedical Engineering

Department of Electronics and Information Systems
Chairman: Prof. dr. ir. Rik Van de Walle
Faculty of Engineering and Architecture
Academic year 2014-2015

UNIVERSITEIT GENT

Preamble

For Nathalie Van Den Berge, thank you for teaching me how to conduct simultaneous DBS fMRI experiments and for pushing me to achieve my highest goals.

For professor Christian Vanhove and Pieter van Mierlo, thank you for your guidance and words of wisdom.

For my parents, thank you for supporting me when I lost the light at the end of the tunnel. You have made me the woman I am today.

No one said it would be easy
They only said it would be worth it
~ B. Marley

I give permission to make this master dissertation available for consultation and to copy parts of this master dissertation for personal use.
In the case of any other use, the copyright terms have to be respected, in particular with regard to the obligation to state expressly the source when quoting results from this master dissertation.
08/06/2015

Investigation of the whole-brain effect of hippocampal deep brain stimulation using fMRI

Julie Ottoy
Supervisor(s): Nathalie Van Den Berge, Vincent Keereman, Roel Van Holen, Christian Vanhove, Pieter van Mierlo

***Abstract*— Deep brain stimulation (DBS) is a neurosurgical procedure to treat patients with neurological and psychiatric symptoms. Despite promising results, the pathways that are affected by hippocampal DBS and the therapeutic mechanism(s) of action remain largely unknown. Electrophysiological and neurochemical studies were mainly used in the past to investigate local DBS-induced effects, but they lack information on a whole-brain scale. Currently, one of the most popular techniques to assess whole-brain activation patterns is functional Magnetic Resonance Imaging (fMRI) based on blood-oxygen-level-dependent (BOLD) contrasts. Healthy rats anesthetized with medetomidine were implanted with an MR-compatible electrode in the right hippocampus and various stimulation intensities were applied to visualize local and distal responses by means of BOLD fMRI. The determination of an optimal stimulus intensity is of clinical importance since there are still DBS non-responders. Correlation analysis revealed that unilateral Poisson distributed hDBS modulates the limbic network and that a certain DBS intensity is necessary to obtain a BOLD response in more regions of this network. In conclusion, our simultaneous DBS fMRI protocol may be a valuable tool to investigate the reproducibility of the DBS-induced effects and to evaluate the effect of various stimulation parameters and targeted brain regions.**

***Keywords*— deep brain stimulation (DBS), hippocampus, fMRI BOLD, refractory epilepsy, whole brain imaging**

I. Introduction

Recently, there is an increased interest in the implantation of stimulation electrodes in deep brain structures to modulate the brain in a therapeutic way, such as in Parkinson's disease [1,2], mood disorders [3] and refractory epilepsy [4,5]. However, the mechanism(s) of action of Deep Brain Stimulation (DBS) remain(s) largely unknown. Functional MRI (fMRI) has become an important tool in recent attempts to clarify these mechanisms. It is a non-invasive technique that utilizes neuronal DBS-induced changes in blood-oxygen-level-dependent (BOLD) responses for measuring and mapping the global spatial activation pattern of the brain.

The aim of this study is to investigate the global effect of hippocampal DBS (hDBS) in healthy rats, using fMRI as a tool to visualize the effect. In order to achieve this, an MR-compatible electrode is chronically implanted in the right hippocampus of healthy rats. The hippocampal formation is the main structure involved in seizure initiation of temporal lobe epilepsy (TLE), the most common form of refractory epilepsy [6]. To rule out the diseased brain as a possible confounder, a healthy rat brain was investigated. In order to avoid motion artefacts during imaging, the animal needs to be immobilized in the scanner. As immobilization without stress is often not possible, the use of anesthesia is required. However, anesthetics suppress neuronal activity and reduce hemodynamic responses. Medetomidine is able to preserve this BOLD response relatively well [7-9] and the effect of this alpha-2-adrenoreceptor agonist can be rapidly reversed by administration of an alpha-2-antagonist [7]. This makes it a valuable anesthetic for longitudinal fMRI in rodents that is necessary to validate the reproducibility of the effect.

To explore hDBS-induced network modulation, data were analyzed by means of two techniques: voxel-wise analysis using the General Linear Model (GLM) and seed-based Correlation Analysis. The latter technique shows the network of regions that are most strongly correlated with the seed. Compared to GLM, correlation analysis has the major advantage that it can account for individual voxel-based hemodynamic delays to peak BOLD responses [10]. In order to visualize local and distal responses to in vivo stimulation, different stimulation intensities were tested. Our results suggest that unilateral Poisson distributed hDBS modulates the limbic network and that a certain DBS intensity is necessary to obtain a BOLD response in more regions of this network.

Further research is needed in a rodent model of TLE to investigate the correlation between the whole-brain modulatory effects of hDBS at a certain stimulus intensity and its therapeutic effects. This can ultimately result in the determination of an optimal stimulation intensity for DBS (non-) responders and improve treatment efficacy in patients with refractory TLE.

II. Materials & methods

A. Subjects

In this study three adult male Sprague-Dawley rats (Janvier Laboratories, Saint Berthevin, France) were used with a body weight between 200g and 250g. All rats underwent three repeated hDBS-fMRI experiments under medetomidine and two under isoflurane. Only one rat was able to sustain our isoflurane protocol, but had to be excluded from the study due to bad headcap placement causing distortion in the fMRI acquisitions. The animals were treated according to guidelines approved by the European Ethics Committee (European Directive 2010/63/EU). The experimental procedures were approved by the Animal Experimental Ethical Committee of Ghent University Hospital (ECD 14/15). The rats were kept in a temperature-controlled room (20-23°C), using a 12h light/dark cycle. The relative humidity was approximately 50%. Food and water were available ad libitum.

B. Surgery

After the rats were anesthetised by a mixture of medical 0_2 and isoflurane (2-5%), a quadri-polar MR-compatible electrode was stereotactically implanted into the right hippocampus (AP: -5.6mm, ML: 5.2mm, DV: -7.4mm relative to Bregma). The stimulation electrode was fabricated in the lab by twisting together four PFA-coated Platinum Iridium wires (A-M Systems, WA, U.S.A.) with 140µm diameter. The two outer wires were used for stimulation purposes, while the inner wires were used for EEG recording. The connectors and wire sets were fixed in place by dental cement and were positioned

Correspondence to: Julie Ottoy; E-mail: Julie.Ottoy@UGent.be

as posterior as possible (**Figure 1**). Additionally, a ground electrode was fabricated, with a diameter of 125µm and made from polyimide coated stainless steel (Bilaney, Germany). The ground electrode was implanted subcutaneously in the neck. The impedance of the electrodes was checked immediately before implantation and did not exceed 70 kΩ. Rats were allowed 1 week of post-surgical recovery before conducting the actual BOLD-fMRI experiments.

Figure 1: (left) Placement of electrode by use of a stereotactic frame, (right) fixation of headcap.

C. Deep Brain Stimulation

All rats were stimulated unilaterally in the right hippocampus with a Poisson distributed stimulation paradigm. The paradigm consisted of a series of bipolar, biphasic, charge-balanced square-wave pulses with a pulse duration of 100µs and an inter-stimulus duration that varied according to a Poisson distribution with mean and variance 1/130 seconds. The electrical stimulation was divided into 5 blocks of 60 seconds, of which 40 seconds OFF and 20 seconds ON.

For each rat, different stimulus intensities were determined individually (i.e., thresholding) based on their seizure threshold. This threshold was assessed by augmenting the stimulation intensity in steps of 25 µA until ictal discharges were observed on the EEG. The thresholding was conducted one day after the post-surgical recovery period. Final stimulation intensities were set at 10, 30, 50, 70 and 90 percent of the individual seizure threshold.

D. BOLD-fMRI acquisition

All MR images were acquired on a Pharmascan 7T (Bruker BioSpin, Ettlingen, Germany) with a bore diameter of 160mm. A Rat Head/Mouse Body volume coil with an inner diameter of 40mm and an outer diameter of 75mm was used to transmit and receive the RF signals. A volume coil was used in order to obtain BOLD responses from subcortical brain structures, such as the hippocampus. The rat was restrained in the scanner using a tooth bar, adhesive tape and two flexible cushions on the two sides of the head. Body temperature was held constant by using a water-circulated heating pad at ± 37°C.

Before starting the BOLD-fMRI data acquisition, the magnetic field homogeneity of the acquisition site was improved by shimming. Global first- and second order shims were applied on the global volume, followed by second order local shimming on an isotropic voxel of 4x12x6mm³. The BOLD-fMRI data acquisition itself was performed using multi-slice single shot gradient-echo echo planar imaging (GE-EPI). The acquisition geometry was adjusted to cover the fourteen coronal slices of interest, with TE=20ms, slice thickness= 1.2mm, matrix size=80x80, pixelsize=0.313x0.312mm^2, FOV=2.5x2.5cm^2. During 5 minutes, 150 EPI's were recorded with a TR of 2 seconds. This GE-EPI run was repeated ten times (two times for each intensity; 5 intensities in total) in randomized order with a 5 minutes rest-period between each run to allow neurovascular recovery and to minimize contribution of heating and tissue damage as can be introduced by DBS [7,8]. Anatomical images were acquired using a Turbo RARE sequence with slice thickness=0.6mm, matrix size =276x320, pixelsize=0.109x0.109mm^2, FOV=3x3.5cm^2. These T2-weighted images provide information about anatomical reference and electrode position verification.

E. Data-analysis

First, the optimal pre-processing steps were determined and systematically applied on all acquired EPI's using SPM8 implemented in Matlab (The Mathworks, Inc., version 7.12.0 (R2011b)). These steps include: 1) realignment to the first image of the first session, 2) coregistration to the anatomical MR, 3) in-plane smoothing using a Gaussian kernel with FWHM of 1mm, and 4) band-pass filtering between [0.01-0.08] Hz using the toolbox REST. Detrending with the toolbox LMGS did not add any value to the pre-processing method but, on the contrary, resulted in increased activations in unexpected regions at the periphery of the brain.

Statistical analysis was performed by means of two techniques: statistical parametric mapping using the general linear model (GLM) and correlation analysis using own scripts written in Matlab. Datasets were averaged over all fMRI runs to perform within-subject analysis. The GLM-based technique quantifies the "goodness of the fit" between the epoched time series of all brain voxels and an a-priori defined stimulation paradigm. Activation plots were generated by means of an F-test, using a multiple comparisons correction method based on Random Field Theory and cluster-based thresholding. The second technique, seed-based correlation analysis, correlates the mean time series of an a-priori defined region-of-interest with the time series of all voxels throughout the brain. Connectivity maps were generated using a correlation coefficient (CC) threshold of 0.3-0.4. Appropriate seeds were chosen based on significant functional activations from our initial GLM analysis.

III. RESULTS

A. General Linear Model

First, analysis of session 1 of rat 1 (with a seizure threshold of 550µA) was performed, since this session shows highly significant results. For low current intensity, different regions such as hippocampal structures and piriform cortex are activating. With increasing stimulation intensity (30-70% of the threshold), additional activating structures include several cortical limbic structures (such as the entorhinal, ectorhinal and perirhinal cortex), thalamic structures, septal nuclei and hypothalamic mammillary bodies. At 90% of the threshold, a bilateral BOLD response in hippocampal, thalamic and cortical limbic structures was detected. Hence, increasing the stimulation intensity goes together with more contralateral hippocampal tissue activation. Furthermore, our findings show that higher stimulation intensity leads to more activating hippocampal volume at the ipsi- and contralateral side, whereby the amount of activating voxels at the ipsilateral HC stays higher (**Figure 2**).

The analysis of averaged sessions in rat 1 and 2 shows rather inconsistent results and no trends as seen in session 1 of rat 1 could be derived by GLM. This is probably due to several constraints that are imposed by GLM, such as the a-priori insertion of our stimulation paradigm. Eventually, we found

for both rats that the intensity (i.e. amplitude) of the BOLD response is largely independent from stimulation intensity.

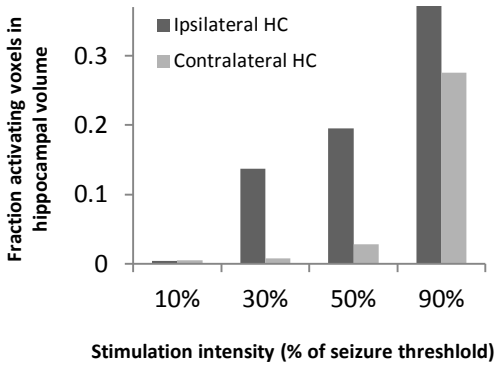

Figure 2: Relation between the stimulation intensity during hDBS and the spatial extent of the hDBS-induced BOLD responses in the ipsi- and contralateral hippocampal formation (HC).

B. Correlation Analysis

Seed-based correlation analysis was first performed for session 1 of rat 1. For 90% of the seizure threshold, the seeds include the medial/lateral ventral part of the septal nuclei (AP: Bregma+0.72mm), hypothalamic medial/lateral mammillary bodies (AP: Bregma-4.7mm) and left hippocampus (AP: Bregma-6.24mm). They were correlated with all other voxels in the brain using a CC threshold of 0.4. Negative CC's (i.e. anti-correlation) were very low and thus not considered as significant. Our findings showed that both mammillary bodies and the septal nuclei have relatively strong connections with each other, as well as with left and right hippocampal structures, anterior thalamic structures (to a rather limited extent), cingulate cortex and entorhinal and perirhinal cortex. Connectivity maps at lower stimulation intensities (30-70% of the threshold) show similar results, but modulation of limbic cortical structures and contralateral hippocampal structures seems to decrease. Also the extent of correlated hippocampal structures decreases with decreasing stimulation intensities. **Figure 3** makes a comparison between connectivity maps for 10% and 90% of the seizure threshold, using the left HC (AP: Bregma-6mm) as a fixed seed. It is seen that there is a widespread bilateral response at 90%, whereas responses at 10% are very small and rather located ipsilaterally.

In order to compare results between the averaged sessions of rat 1 and rat 2, fixed seeds at exactly the same locations were applied in both rats. For stimulation at 90% of the seizure threshold, the first seed corresponds to the contralateral lateral-medial zone of the hypothalamus (i.e. tuberomammillary nuclei and medial/lateral mammillary bodies) (AP: Bregma-4.20mm) and the second seed corresponds to ectorhinal/perirhinal cortex (EcC/PC) (AP: Bregma-6.36mm). Correlation maps with a CC threshold of 0.3 show strong correlation between mammillary bodies and septal nuclei, ipsi- and contralateral hippocampal structures and limbic cortical structures such as ectorhinal, perirhinal, entorhinal, (amygdalo-) piriform and cingulate cortex. The second seed additionally shows connection with the amygdalohippocampal area and cortical/medial amygdaloid nuclei. Results from the second rat were largely similar, but thalamic connections (especially the anterior nucleus of the thalamus) were more clear.

At lower stimulation intensities, there was a trend of seeds being less connected with hippocampal, (hypo)thalamic and limbic cortical structures. Still, thalamic connections remained most clear in the second rat.

Conclusions about the relation between the extent of correlated regions on the one hand, and stimulation intensities on the other hand, were drawn by taking two fixed seeds (left and right HC, resp. -6mm and -7mm from Bregma) for all stimulation intensities. At 10% of the seizure threshold, there is almost no correlation of brain regions with either the left or right HC. At 30%, 50% and 70% of the seizure threshold, there is not much difference between the amount and extent of correlated regions, but there is certainly more correlation than at 10%. At 90% of the seizure threshold, there is a strong increase in the amount and extent of correlated regions compared to lower stimulation intensities. There is also a clear bilateral response detected.

IV. DISCUSSION

Statistical analysis of fMRI data reveals that unilateral Poisson distributed hDBS influences the oxidative metabolism in different structures of the limbic system, including the hippocampal formation, (hypo)thalamic nuclei, amygdala, septal areas and the limbic cortex. With this study, our aim was to investigate whole-brain BOLD responses to hDBS in healthy rats anesthetised with medetomidine and to characterize the responses of different stimulation intensities. Using healthy rats eliminates brain pathology as a possible confounder. Furthermore, using medetomidine as the anesthetic minimizes the suppressive effect on neuronal activity and hemodynamic BOLD responses.

A. Whole-brain BOLD response of DBS

The current study reveals whole-brain effects in the hippocampal formation and other limbic structures that are anatomically connected with the hippocampus. This points out that hDBS not only causes local interaction at the site of stimulation but also in remote limbic pathways. Hippocampal-thalamic responses were especially detected in the second rat. Remarkably, its electrode was implanted more posteriorly in the brain, close to the pre-, para- and postsubicular areas (**Figure 4**). These findings correspond to those of Swanson et al. [12], who declared that the projection to the anterior nuclear complex of the thalamus arises more posteriorly in the pre- and/or parasubiculum and the postsubicular area of the rat hippocampal formation. Additional electrode mapping experiments could be useful to investigate the true difference between a more anterior and more posterior implanted electrode.

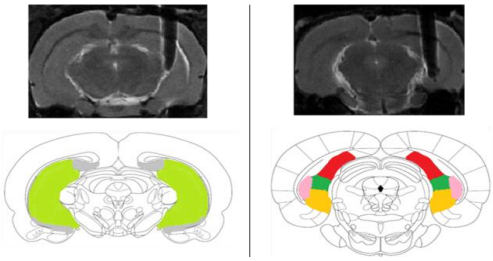

Figure 4: Above: Structural MR of rat 1 (AP: -5.2 mm) and rat 2 (AP:-7mm); below: Axial slice from rat brain atlas [1] with light green corresponding to the hippocampal formation (CA I/II/III, DG), grey to the ventral/dorsal sub, red to postsub, green to presub, yellow to parasub and pink to transition area of sub. It is seen that in rat 2 the electrode is implanted more posteriorly in the brain, close to the pre-, para- and postsubiculum.

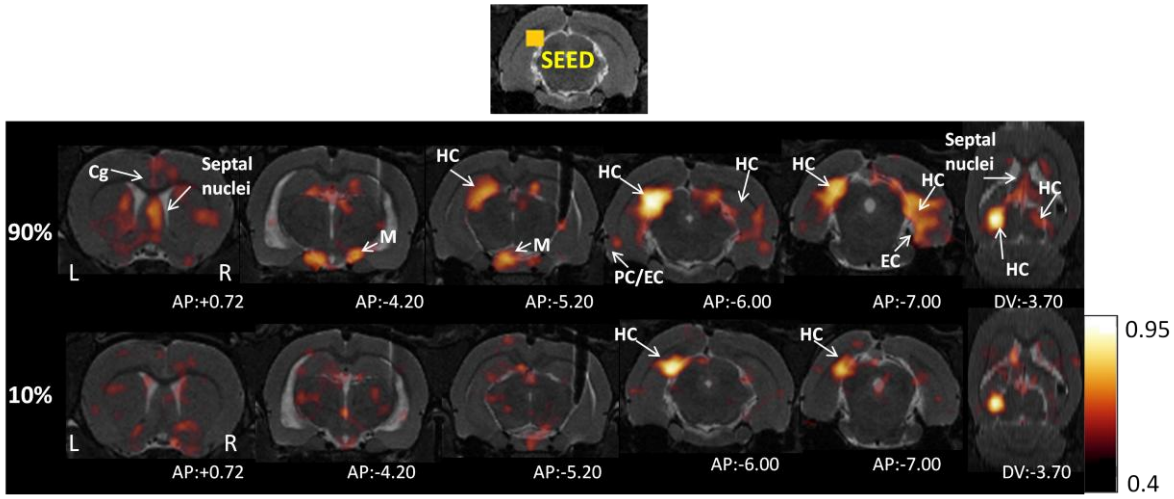

Figure 3: Comparison of correlation maps between stimulation at 90% (above) and 10% (below) of the seizure threshold (550µA in this rat) for a fixed seed (left hippocampus, AP: Bregma-6mm). The hippocampal structures (HC), entorhinal cortex (EC), perirhinal cortex (PC), mammillary bodies (M), septal nuclei and Cg (cingulate cortex) are labelled with white arrows. Network activity is more extended for stimulation at 90%.

In addition, our results indicate not only local and distal effects induced by hDBS, but also indicate a bilateral nature of this effect, depending on the stimulation intensity. Bilateral synchrony of fMRI signals is detected especially in limbic brain regions which are characterized by strong interhemispheric commissural connections such as the hippocampus [13]. These findings are concordant with previous resting-state fMRI studies of the healthy rat brain [14-16].

Finally, our results indicate that the volume of the effect is dependent of the stimulus intensity. We were able to detect robust bilateral BOLD responses by means of Correlation Analysis (CC > 0.3-0.4) when a stimulation intensity corresponding to 90% of the seizure threshold was used. Differences in BOLD responses at lower stimulus intensities (i.e. 30%, 50% and 70% of the seizure threshold) were less clear, but compared to 90% the overall responses seemed less widespread and rather located ipsilaterally from the DBS electrode. Additional research on a larger group of animals is needed to develop a dose-response curve. Stimulation at 10% of the seizure threshold did not result in remarkable regions of increased connectivity. Taken together, our results suggest that a certain DBS intensity is required for visualisation of not only a local, but a whole-brain effect. Depending on the subject, below such a DBS intensity the BOLD response is very small or insignificant. Stimulation above this intensity results in robust bilateral and widespread responses, probably mediated by commissural fibers. Previous rodent studies revealed also a positive BOLD response in different areas of the hippocampal formation [17-20], as well as an increase in spatial extent of the response with increasing stimulation intensity [17]. No correlation was found between the amplitude of the BOLD response and the stimulus intensity, which supports the findings of [21] and [22].

The current study also investigates the reproducibility of whole-brain DBS-induced effects by using chronically implanted MR compatible electrodes. It is seen that the BOLD responses from 3 repeated DBS-fMRI experiments with the same DBS parameters remain largely consistent. Other advantages of using chronically implanted electrodes, compared to direct stimulation applied in previous simultaneous hDBS fMRI studies, are less tissue inflammation due to a post-surgical recovery period of one week and less displacements of the electrode during image acquisition due to fixations with dental cement.

B. Seed-based Correlation Analysis vs. GLM

Seed-based correlation analysis showed consistent responses (CC > 0.3-0.4) in different structures of the limbic system above 10% of the seizure threshold. Strong and bilateral responses were visually detected at 90%. With GLM on the other hand, those limbic regions occasionally display BOLD responses above 10% stimulation, but this was never consistent between different rats and/or different sessions. The distinct findings between these two analysis techniques are probably due to the fact that correlation analysis is a typical reflection of functional integration (i.e., which brain regions are connected and interact with each other), whereas statistical mapping based on GLM is rather used to describe functional specialization (i.e., which regions respond to a particular, a-priori inserted experimental input). The a-priori insertion of a HRF with a fixed shape and time delay across subjects and brain regions in the GLM model is likely to underestimate BOLD responses. Compared to GLM, correlation analysis can directly account for individual voxel-based hemodynamic delays to peak BOLD responses.

C. Physiological meaning

Because the hippocampal formation is considered as the main structure involved in seizure initiation of refractory TLE, hippocampal depth stimulation has been successfully put forward as a treatment procedure of TLE [23,24]. Despite promising results, the pathways that are affected by hDBS as well as its exact mechanism(s) of action remain largely unknown. In epilepsy, four main hypotheses have been proposed to explain these therapeutic mechanism(s): (a) depolarization blockade [25], (b) synaptic inhibition [26], (c) homeostatic downscaling of intrinsic excitability [27] and (d) glial-neuronal interactions leading to a wide range of activation and inhibition effects in the whole brain network [28]. The latter hypothesis supports an important role for the astrocytes in synaptic transmission. When astrocytes are activated, they can signal further astrocytes through long-distance Ca2+-waves across large networks, contributing to our observed distal (ipsilaterally) effects induced by hDBS. The observed bilateral effects, however, are more likely to be

explained by the presence of strong commissural connections between both hemispheres in the rat. It remains unclear whether these bilateral effects of hDBS will be as strong in humans [29]. The other hypotheses are far more difficult to link with our DBS-induced activation patterns, since fMRI is rather agnostic regarding the direction of modulation (i.e., excitation or inhibition) [30,31]. Additional cellular studies, such as optogenetics combined with DBS, could provide more insight in what happens on neuronal level during stimulation.

D. Limitations

The study has a number of limitations. First of all, fMRI may not be able to adequately resolve temporally dynamic DBS-induced changes in cellular activity, due to its rather limited temporal resolution. In order to provide complimentary information about the coupling between electrical local field potentials (LFP's) and BOLD responses, electrophysiological recordings in conjunction with fMRI are suggested [32]. Secondly, the determination of the stimulation intensity based on the seizure threshold of the individual rat (i.e. thresholding) may act as a confounder since it requires induction of ictal activity. Despite the fact that each DBS-fMRI experiment was repeated three times for each subject, thresholding itself was performed only once. Repeated electric stimulation of limbic structures might result in progressive development of seizure activity in a non-epileptic brain. Thirdly, using fMRI as the analyzing technique can result in a small underestimation of the actual effect induced by hDBS around the site of the electrode. Despite the MR-compatible nature of PtIr, there is still an MR-artefact induced by the electrode and to a lesser extent by the headcap. This results in suppressed responses at the ipsilateral and posterior side of the electrode. A fourth limitation of the study is the small amount of subjects that were used, leading to less statistical power. Eventually, deviations in electrode placement smaller than the spatial resolution of the MR images may produce large differences in BOLD responses. Adequate electrode positioning in the hippocampus could be verified with the aid of (post-mortem) high-resolution anatomical MR images.

V. CONCLUSION

Our results suggest that unilateral Poisson distributed hDBS modulates different brain regions of the limbic network notably the hippocampal formation, (hypo)thalamic nuclei, amygdala, septal areas and the limbic cortex. This means that hDBS exerts both local and distal effects due to neuroanatomical and interhemispheric connections between the structures. Moreover, our results suggest that a certain DBS intensity is required to visualise the effect in more brain regions of the network. Depending on the subject, below such a DBS intensity the BOLD response is very small or insignificant. Stimulation above this intensity results in robust bilateral and widespread responses, probably mediated by commissural fibers.

Further research is necessary in a rodent model of TLE to investigate the correlation between the whole-brain modulatory effects of DBS at a certain stimulus intensity and its therapeutic effects. The determination of an optimal stimulus intensity is of clinical importance since there are still DBS non-responders. Moreover, some responders might benefit from lower stimulation intensities, which is advantageous for the battery life of the pulse generator. In conclusion, our simultaneous DBS fMRI protocol may be a valuable tool to investigate the reproducibility of the DBS-induced effects and to evaluate the effect of various stimulation parameters and targeted brain regions. With regard to data analysis techniques, it is concluded that seed-based correlation analysis is a valuable alternative for GLM to visualize DBS-induced network activity, since it can account for individual voxel-based hemodynamic delays to peak BOLD responses.

ACKNOWLEDGEMENTS

This work is funded by iMinds and Ghent University. Prof. dr. Roel Van Holen is supported by the Research Foundation Flanders, Belgium (FWO). Prof. dr. Christian Vanhove is supported by the GROUP-ID consortium of Ghent University.

REFERENCES

[1] Arantes PR, Cardoso EF, Barreiros MA, Teixeira MJ, Goncalves MR, Barbosa ER, Sukwinder SS, Leite CC, Amaro E Jr. (2006) **Performing functional magnetic resonance imaging in patients with Parkinson's disease treated with deep brain stimulation.** Mov. Disord., 21 (2006), pp. 1154–1162

[2] Albaugh DL, Shih YY (2014) **Neural circuit modulation during deep brain stimulation at the subthalamic nucleus for Parkinson's disease: what have we learned from neuroimaging studies?** Brain Connect, 2014;4:1–14

[3] Ressler KJ, Mayberg HS (2007) **Targeting abnormal neural circuits inmood and anxiety disorders: From the laboratory to the clinic.** Nat Neurosci, 2007;10:1116–24

[4] Boon P, Vonck K, De Herdt V et al. (2007) **Deep brain stimulation in patients with refractory temporal lobe epilepsy.** Epilepsia 48: 1551–1560

[5] Cukiert A, Cukiert C.M, Burattini JA & Lima AM (2014) **Seizure outcome after hippocampal deep brain stimulation in a prospective cohort of patients with refractory temporal lobe epilepsy.** Seizure 23, 6–9

[6] Kwan P, and Brodie MJ (2000**) Early identification of refractory epilepsy.** New England Journal of Medicine 342: 314–319

[7] Weber R, Ramos-Cabrer P, Wiedermann D, van Camp N & Hoehn M (2006) **A fully noninvasive and robust experimental protocol for longitudinal fMRI studies in the rat.** Neuroimage 29, 1303–1310

[8] Zong X, Fukuda M, Vazquez A, Kim S-G (2013) **Effects of the a2-adrenergic receptor agonist dexmedetomidine on neural, vascular and BOLD fMRI responses in the somatosensory cortex.** Salt Lack City, 2013 20–26 April

[9] Williams KA, Magnuson M, Majeed W, Peltier SJ, LaConte SM, Keilholz SD, Hu X (2010) **Comparison of α-chloralose, medetomidine, and isoflurane anesthesia for functional connectivity mapping in the rat.** Magn. Reson. Imaging 28, 995–1003

[10] Handwerker DA, Ollinger JM, & D'Esposito M (2004) **Variation of BOLD hemodynamic responses across subjects and brain regions and their effects on statistical analyses.** Neuroimage, 21(4), 1639-1651

[11] Pawela CP, Biswal BB, Hudetz AG, Schulte ML, Li R, Jones SR & Hyde JS (2009) **A protocol for use of medetomidine anesthesia in rats for extended studies using task-induced BOLD contrast and resting-state functional connectivity.** Neuroimage, 46(4), 1137-1147

[12] Swanson LW & Cowan WM (1977) **An autoradiographic study of the organization of the efferet connections of the hippocampal formation in the rat.** Journal of Comparative Neurology, 172(1), 49-84

[13] Buchhalter JR, Fieles A, Dichter MA (1990) **Hippocampal commissural connections in the neonatal rat.** Dev Brain Res 56:211–216

[14] Becerra L, Pendse G, Chang PC et al (2011) **Robust reproducible resting state networks in the awake rodent brain**. PLoS One 6(10):e25701

[15] Jonckers E, Van Audekerke J, De Visscher G et al (2011) **Functional connectivity of the rodent brain: comparison of functional connectivity networks in rat and mouse.** PLoS One 6(4):e18876

[16] Zhang N, Rane P, Huang W, Liang Z, Kennedy D, Frazier JA & King, J (2010) **Mapping resting-state brain networks in conscious animals.** Journal of neuroscience methods, 189(2), 186-196

[17] Canals S, Beyerlein M, Murayama Y, Logothetis N.K (2008) **Electrical stimulation fMRI of the perforant pathway to the rat hippocampus.** Magnetic Resonance Imaging, 26, 2008, pp. 978-986

[18] Krautwald K, Min H-K, Lee KH, Angenstein F (2013) **Synchronized electrical stimulation of the rat medial forebrain bundle and perforant pathway generates an additive BOLD response in the nucleus accumbens and prefrontal cortex.** NeuroImage.

[19] Alvarez-Salvado E, Pallare´s V, Moreno A, Canals S (2014) **Functional MRI of long-term potentiation: imaging network plasticity.** Philosophical Transactions of the Royal Society B: Biological Sciences 369: 20130152
[20] Canals S, Beyerlein M, Merkle H, Logothetis NK (2009) **Functional MRI evidence for LTP-induced neural network reorganization.** Current Biology 19: 398–403
[21] Van Den Berge N, Keereman V, Vanhove C, Van Nieuwenhuyse B, van Mierlo P, Raedt R & Van Holen R (2014) **Hippocampal Deep Brain Stimulation Reduces Glucose Utilization in the Healthy Rat Brain**. Molecular Imaging and Biology, 1-11
[22] Klein J, Soto-Montenegro ML, Pascau J, et al. (2011) **A novel approach to investigate neuronal network activity patterns affected by deep brain stimulation in rats.** Jour of Psych Res 45: 927-930
[23] Vonck K, Boon P, Claeys P, Dedeurwaerdere S, Achten R (2005) **Long-term deep brain stimulation for refractory temporal lobe epilepsy.** Epilepsia, 46 (Suppl 5) pp. 98–99
[24] Velasco AL, Velasco M, Velasco F, Menes D, Gordon F, Rocha L, Briones M, Marquez I (2000) **Subacute and chronic electrical stimulation of the hippocampus on intractable temporal lobe seizures: preliminary report.** Archives of Medical Research, 31 pp. 316–328
[25] Beurrier C, Bioulac B, Audin J, Hammond C (2001) **High-frequency stimulation produces a transient blockade of voltage-gated currents in subthalamic neurons.** J Neurophysiol 2001;85:1351–6
[26] Dostrovsky JO, Levy R, Wu JP, Hutchison WD, Tasker RR, Lozano AM. (2000) **Microstimulation-induced inhibition of neuronal firing in human globus pallidus.** J Neurophysiol 2000;84:570–4
[27] van Welie I, van Hooft JA, and Wadman WJ (2004) **Homeostatic scaling of neuronal excitability by synaptic modulation of somatic hyperpolarization-activated I-h channels.** Proc Natl Acad Sci (USA) 101: 5123-5128
[28] Vedam-Mai V, van Battum EY, Kamphuis W, et al. (2012) **Deep brain stimulation and the role of astrocytes.** Mol Psych 17: 124–131
[29] Supekar K, Musen M, Menon V (2009) **Development of large-scale functional brain networks in children.** PLoS Biol. 2009 Jul; 7(7):e1000157
[30] Heeger DJ & Ress D (2002) **What does fMRI tell us about neuronal activity?** Nature Reviews Neuroscience, 3(2), 142-151
[31] Logothetis NK (2008) **What we can do and what we cannot do with fMRI.** Nature, 453(7197), 869-878
[32] Huttunen JK, Gröhn O & Penttonen M (2008) **Coupling between simultaneously recorded BOLD response and neuronal activity in the rat somatosensory cortex.** Neuroimage, 39(2), 775-785

Contents

List of abbreviations

AP	Anterior posterior
B_0	Static magnetic field
BOLD	Blood oxygen level dependent
CBF	Cerebral blood flow
CC	Correlation coefficient
DV	Dorsoventral
(h)DBS	(hippocampal) Deep brain stimulation
EEG	Electroencephalography
FID	Free induction decay
fMRI	Functional magnetic resonance imaging
FOV	Field of view
FWHM	Full width at half maximum
GE-EPI	Gradient-echo echo planar imaging
GLM	General linear model
HRF	Hemodynamic response function
ML	Mediolateral
MRI	Magnetic resonance imaging
PDS	Poisson distributed stimulation
PtIr	Platinum Iridium
RF	Radio frequency
RFT	Random field theory
ROI	Region of interest
SE	Spin-echo
SNR	Signal-to-noise ratio
SPM	Statistical parametric mapping
TE	Echo time
TLE	Temporal lobe epilepsy
TR	Repetition time

Chapter 1

Introduction

Recently, there is an increased interest in the implantation of stimulation electrodes in deep brain structures to modulate the brain in a therapeutic way, such as in Parkinson's disease [1,2], mood disorders [3] and refractory epilepsy [4,5]. However, the mechanism(s) of action of Deep Brain Stimulation (DBS) remain(s) largely unknown. Functional MRI (fMRI) has become an important tool in recent attempts to clarify these mechanisms. It is a non-invasive technique that utilizes neuronal DBS-induced changes in blood-oxygen-level-dependent (BOLD) responses for measuring and mapping the global spatial activation pattern of the brain. fMRI has been used in task-related [6,7] and resting-state experiments [8,9] to investigate the functional connectivity [10,11] of the brain, as well as in several brain plasticity experiments [12,13].

The aim of this study is to investigate the global effect of hippocampal DBS (hDBS) in healthy rats, using fMRI as a tool to visualize the effect. In order to achieve this, an MR-compatible electrode is implanted in the right hippocampus of healthy rats. The hippocampal formation is the main structure involved in seizure initiation of temporal lobe epilepsy (TLE), the most common form of refractory epilepsy [14]. To rule out the diseased brain as a possible confounder, a healthy rat brain was investigated. In order to avoid motion artefacts during imaging, the animal needs to be immobilized in the scanner. As immobilization without stress is often not possible, the use of anesthesia is required. However, anesthetics suppress neuronal activity and reduce hemodynamic responses. Medetomidine is able to preserve this BOLD response relatively well [10,15,16] and the effect of this alpha-2-adrenoreceptor agonist can be rapidly reversed by administration of an alpha-2-antagonist [15]. This makes it a valuable anesthetic for longitudinal fMRI in rodents that is necessary to validate the reproducibility of the effect.

To explore hDBS-induced network modulation, data were analyzed by means of two techniques: voxel-wise analysis using the General Linear Model (GLM) and seed-based Correlation Analysis. The latter technique shows the network of regions that are most strongly correlated with a seed. Compared to GLM, correlation analysis has the major advantage that it can account for individual voxel-based hemodynamic delays to peak BOLD responses [17]. In order to visualize local and distal responses to in vivo stimulation, different stimulation intensities were tested. Our results suggest that unilateral Poisson distributed hDBS modulates the limbic network and that a certain DBS intensity is necessary to obtain a BOLD response in more regions of this network. No relationship was found between the amplitude of the BOLD response and the stimulation intensity.

Further research is needed in a rodent model of TLE to investigate the correlation between the whole-brain modulatory effects of hDBS at a certain stimulus intensity and its therapeutic effects. This can ultimately result in the determination of an optimal stimulation intensity for DBS (non-) responders and improve treatment efficacy in patients with refractory TLE.

Chapter 2

Literature study

2.1 Structural imaging techniques

2.1.1 Magnetic Resonance Imaging (MRI)

Magnetic Resonance Imaging (MRI) is a non-invasive, non-ionizing medical imaging technique that uses a strong magnetic field and radiofrequent electromagnetic waves to make images of internal body structures. The images are produced based on spatial variations in the phase and frequency of the energy that is absorbed and emitted by the imaged object. More in specific, it is the MR signal from the hydrogen nuclei within fat and water that is primarily imaged by MRI. The technique is especially sensitive for soft tissues such as organs and muscles, compared to x-ray examinations. The purpose of MRI-imaging is to visualize parts of the body in order to assist doctors in diagnosing diseases and evaluating injuries. In this study, MRI scans are used to acquire high-resolution anatomical images of the rat brain as a structural underlay for functional images with lower spatial resolution. Moreover, structural MRI's give the possibility to visualize the exact location of the electrode tract.

2.1.1.1 Physics behind MRI

Imagine a compass needle that is placed in a magnetic field created by a powerful magnet. After a short period of time, the needle will point in the direction of the magnetic field. The magnetic needle is said to be "in equilibrium". If the needle is given a small push perpendicular to the magnetic field (i.e. rotation), it will oscillate [1] and gradually dampen again. The number of oscillations per second is called the resonance frequency. As long as the needle oscillates, radio waves are emitted with the same frequency as that of the needle's oscillation. However, the amplitude of the radio waves gradually decreases together with the oscillations and eventually the needle is realigned again with the original magnetic field.

The human body also contains such "magnetic needles", namely the hydrogen nuclei. Fat and water have many hydrogen atoms, which makes the human body approximately 63% hydrogen atoms [18]. Some fundamental differences exist between a compass needle and a hydrogen nucleus. The two properties of the NMR nucleus that are of most importance for the occurrence of the magnetic resonance phenomena are (**Figure 3**):

- An atomic nucleus rotates around its own length axis, thereby possessing an intrinsic angular momentum (or spin) l.
- An atomic nucleus possesses a permanent magnetic dipole moment:

$$\mu = \gamma \, l \tag{1}$$

  whereby l is the spin quantum number (½ for H-atoms) and γ is the gyromagnetic ratio (42.58 MHz/T for H-atoms).

1 An oscillating magnetic field is a magnetic field that changes its direction in time, also called radio waves

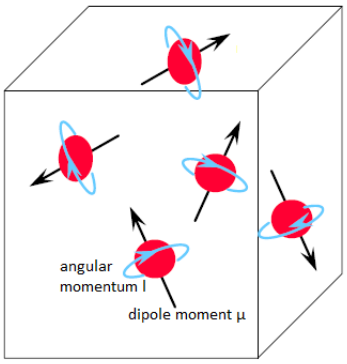

Figure 3: Hydrogen atoms in the human body rotate around their own axis (angular momentum l) and possess a dipole moment μ [19].

When the spins are placed in a stationary magnetic field (B_0), the spins will align with this field and the rotation of the spins around B_0 is called a precession movement. The precession frequency is known as the Larmor frequency:

$$w = \gamma B_0 \quad (2)$$

A 7 Tesla MRI scanner has a Larmor frequency of 298.06 MHz. However, the alignment of the spins with B_0 is only partially (**Figure 4a**). Broadly defined, they can orientate in two different directions with respect to B_0, depending on having a magnetic moment number m= + ½ (parallel with B_0) or m=-½ (anti-parallel with B_0). Most spins are found in the lower energy state (m=+½), which results in a *net* longitudinal magnetization M_0 in alignment with B_0 (parallel with the Z-axis) (**Figure 4b**).

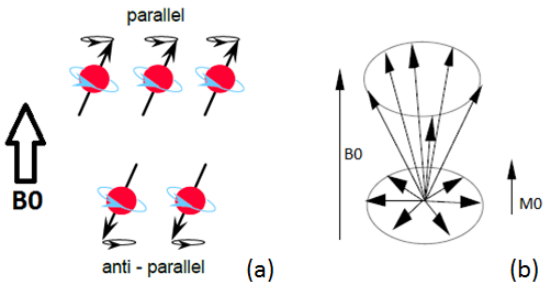

Figure 4: a) When a B_0-field is applied, the spins will align parallel or anti-parallel with this field, depending on their energy state [19]. B) Because most spins are found in the lower energy state (m=+1/2), a net longitudinal magnetization vector M_0 is created in alignment with B_0 (parallel with the Z-axis).

2.1.1.2 Relaxation times

The net magnetization along the stationary magnetic field B_0 can be brought out of equilibrium by applying a weak oscillating magnetic field perpendicular to B_0, called the B_1-field. This radiofrequency (RF) field must oscillate at the Larmor frequency ($w = \gamma B_0$) and can be applied through an RF coil subject to a current. By absorption of the resonant energy of the RF pulses, spins move from the lower to the higher energy states. The net magnetization vector is turned 90° [2] to the transversal plane (M_{xy}) (**Figure 5**) and makes precession movements in the XY-plane around the Z-axis. When the RF-pulses are stopped, relaxation of the spins takes place. This relaxation process occurs on two different time scales with two different time-constants, namely T1 and T2.

2 The flip angle (FA) is 90° in the spin-echo (SE) sequence, but can differ for other sequences (see below).

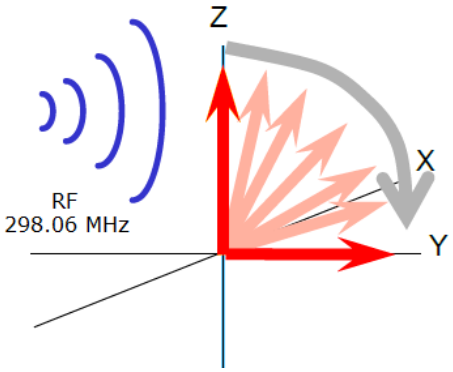

Figure 5: By applying an RF pulse at 298.06 in a 7 Tesla system, the longitudinal magnetization vector is turned to the transversal plane.

T2-relaxation T2 is the relaxation time necessary to decrease 37% of the transversal magnetization vector (M_{xy} -> M_{xy}=0) (**Figure 6**). This happens because of the loss of phase coherence due to spin-spin interactions. Each spin precesses at a slightly different Larmor frequency from the others. Magnetic dipole moments can also dephase because of small, local field inhomogeneities (meaning variation in B_0). In this case, the dephasing is small in the beginning, but increases gradually. The produced signal is called Free Induction Decay (FID) and is responsible for the T2*-relaxation.

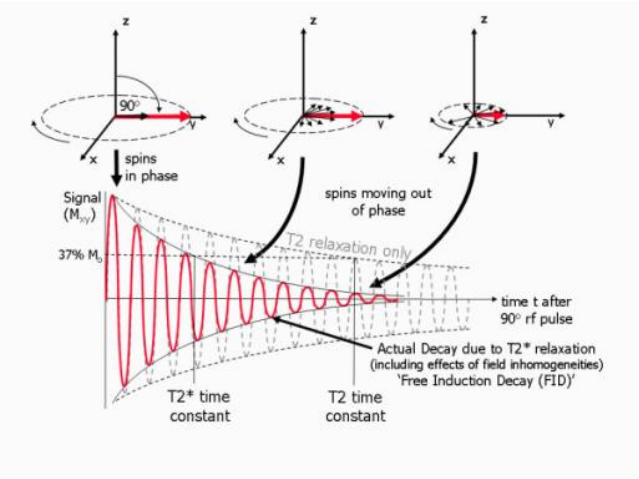

Figure 6: T2 and T2* relaxation [20].

T1-relaxation T1 is the relaxation time necessary to restore 63% of the longitudinal (equilibrium) magnetization M_0 (M_z -> M_0) (**Figure 7**). Depending on how easily the lattice absorbs the energy of the spins when they return to lower energy states (spin-lattice interactions), T1 will be shorter. All processes that result in T1-relaxation also result in T2-relaxation, hence T1 is never shorter than T2 [21].

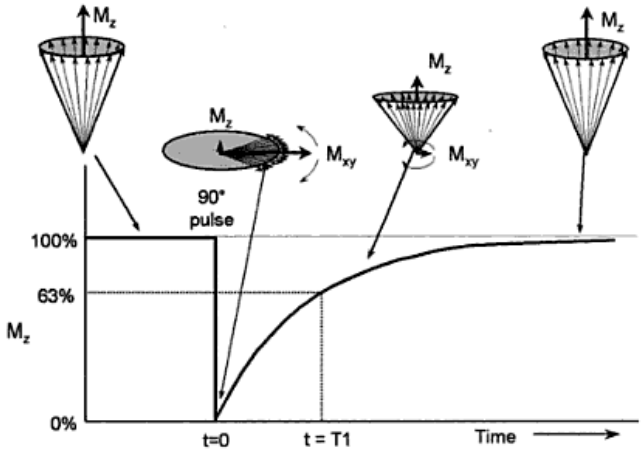

Figure 7: T1 relaxation [22].

2.1.1.3 Contrasts

T1- and T2-weighted images

T2 contrast If the image contrast mainly reflects T2-variations, one speaks about T2-weighted images (**Figure 8 middle**). In this case, tissues with a lot of fluid appear to look brighter than firm matter; their T2 relaxation time is longer (seconds instead of milliseconds). The reason behind this phenomena is that within a fluid, the high mobile spins experience constantly new neighbors. This results in a slower dephasing compared to a situation whereby the frequency of one spin is constantly altered by a persistent amount of neighbours [21].

T1 contrast If on the other hand the image contrast mainly reflects T1-variations, one speaks about T1-weighted images (**Figure 8 left**). Since T1 contrast is based on spin-lattice interactions, a tight bound hydration layer (as in very firm matter, eg. bone) or free moving particles (as in fluids) will have longer T1 (seconds). They will look dark on the MRI-image, in contrast to semi-firm matter (eg. soft and fat tissue) with intermediate bindings.

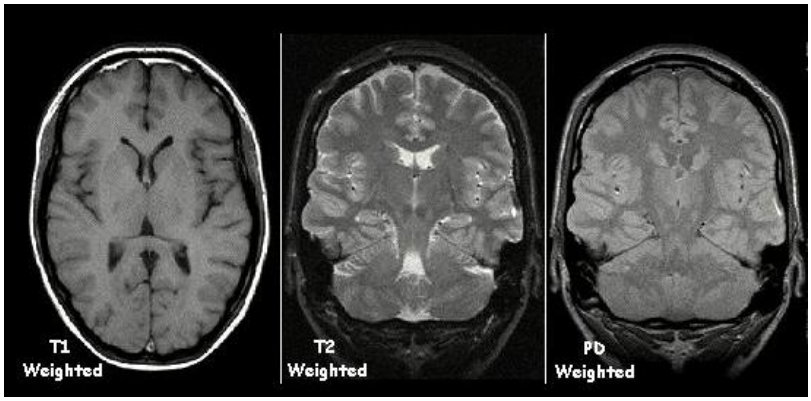

Figure 8: T1, T2 and PD weighted images.

Influence of TE and TR on contrast

The echo time (TE) is the time between a 90° excitation pulse and the subsequent echo. Hence, the TE gives T2-weighting in the images, whereby increasing TE results in a greater T2-weighting (**Figure 9a**). When T2 is approximately equal to TE, the greatest sensitivity to T2-variation is achieved. On the other hand, the repetition time (TR) is the time between two excitation pulses. If

there is enough time between two such pulses, the longitudinal magnetization can fully recover to equilibrium. Because TR is in this case longer than T1, there is no T1-contrast anymore, but a strong signal will be measured (**Figure 9b**).

Summarized, T1-weighted images are obtained by applying a short TE (T2 relaxation is then decreased) and a short TR. T2-weighted images on the other hand are obtained by a long TR and TE. When both T1- and T2- contrast are minimized, a proton density-weighted (PD) image is created (**Figure 8 right**). In this case, a high concentration of protons is required to create a strong signal. A long TR and a short TE is necessary to create a PD-weighted image.

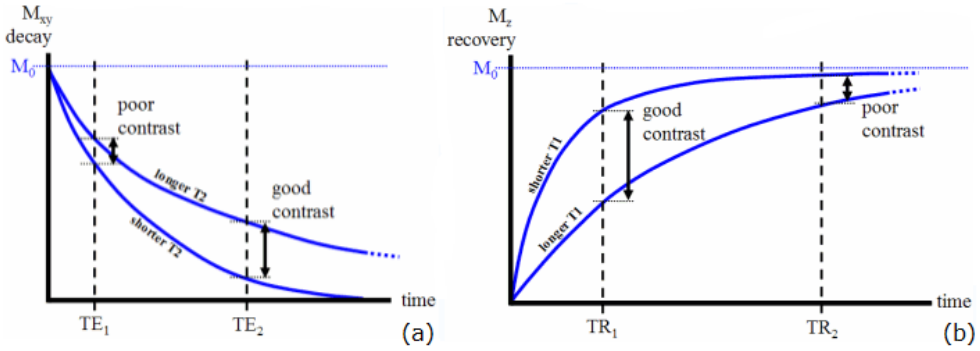

Figure 9: Influence of TE (a) and TR (b) on T1 and T2 contrasts. [23]

2.1.1.4 Spatial encoding

The purpose of MRI-imaging is to visualize parts of the body in order to assist doctors in diagnosing diseases and evaluating injuries. Contrast can be created due to the fact that protons have other relaxation times in different tissues and fluids. Localizing these protons is achieved by gradient coils. Such a coil creates a magnetic field gradient that varies linearly in one direction. A complete spatial localization (encoding) requires magnetic field gradients in three directions.

- Slice selection
  A magnetic field gradient is applied along a certain axis of the body, eg. G_z along the Z-axis (longitudinal direction). Hence, protons on different positions z will have different Larmor frequencies, because an extra field was added to B_0. A slice of thickness ΔZ can be selected by sending an RF excitation pulse of bandwidth ΔW.
- Phase encoding
  A magnetic field gradient (eg. G_y along the Y-axis) attributes a specific phase angle to the transverse magnetization vectors, depending on their positions in the Y-direction. When the phase gradient is turned off, the Larmor frequency of all the spins will be identical again. However, the applied phase shifts are maintained. For an SE-sequence with n rows, n acquisitions with each a different phase encoding gradient are applied in order to obtain a 2D-image.
- Frequency encoding (read-out)
  When the protons are excited in one slice, they emit RF waves. These signals can be localized by applying a magnetic field gradient in plane of the selected slice (eg. G_x when G_z was applied). It thus creates columns of protons which all have an identical Larmor frequency (**Figure 10**).

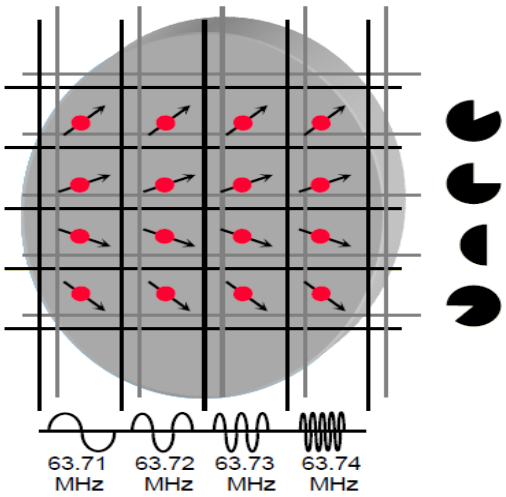

Figure 10: The end result of the spatial encoding involves 1. The Gz gradient selected an axial slice. 2. The Gy gradient created rows with different phases. 3. The Gx gradient created columns with different frequencies [19].

2.1.1.5 Influence of increasing the field strength

If B_0 increases, the Larmor frequency increases (cfr. $w = \gamma B_0$). Therefore, the number of resonant protons that are available to transfer energy to the lattice decreases. Hence, T1 is lengthened, meaning a slower regrowth of the net longitudinal magnetization vector (Z-direction). This slower recovery will need a longer TR, which leads on its turn to an increased scan time and decreased coverage. One of the major advantages of high-field imaging is the potential increase in SNR and spatial resolution.

In small animal MRI, high field strengths (3-14 Tesla) are needed to achieve a reasonable SNR [24]. Also a high spatial resolution is required in small animal imaging. Increasing the spatial resolution decreases the SNR as its cube root, hence a large imaging time is necessary to regain the SNR of the lower resolution (since the SNR only increases as the square root of imaging time). In this way, it is clear that increasing the imaging time would be an "expensive way" of increasing the SNR. Imaging at increased magnetic field strength has also some disadvantages. It goes together with an increase in cost of the magnets, an increase in RF power requirements, adverse effects on the animals and eventually, an increase in image distortions due to more susceptibility effects at higher fields. Other parameters that are field strength-dependent include the T1 and T2 relaxation times, leading to contrasts that will differ from those that are mostly used in clinical scanners (0.4-1.5 Tesla). Since the relaxation times are found to be much closer to each other at increased field strengths, the gray-white matter contrast differentiation is actually worse at higher fields [24]. Moreover, for rodents in particular it was investigated that their difference in white and gray matter T1 relaxation is smaller than in humans at each field strength [25]. This can be due to different cytoarchitecture and the use of anesthetics in animals during imaging. Eventually, increasing the field strength in solid tissues goes together with longer T1 and shorter T2 relaxation times. However, since the increasing availability of fast T2-weighted pulse sequences, a reduced T1 contrast might be less of a problem. T1-weighted pulse sequences are more used for contrast-enhanced imaging, whereby stronger T1-shortening effects may occur by using contrast agents at higher fields [26].

2.1.2 Computed Tomography (CT)

Computed tomography (CT) uses X-rays for obtaining a 3D image of the tissue density [28]. An X-beam is rotated around the body (0°-360°) and the transmitted X-rays through the patient are measured along individual projection lines (**Figure 11**). Direct analytical reconstruction from the projections at different angles is possible by using the Filtered Back Projection (FBP) reconstruction algorithm. The obtained images are scaled in Hounsfield Units (HU), determined by the ratio of the linear attenuation coefficient of a voxel to the linear attenuation coefficient of water. A bright voxel corresponds to an area of high attenuation, meaning that most of the incoming X-rays are absorbed by a relatively dense material. For water, HU equals zero. Lungs are more transparent than water, resulting in lower HU (-400 up till -600). Bone, on the other hand, is denser and has higher HU than water (+400 up till +1000). The HU of soft tissues and fat are very close to those of water; in this case, MRI is preferable over CT for obtaining good contrast. In order to acquire optimal soft tissue differentiation in structural images of the brain, MRI is prefered in this study.

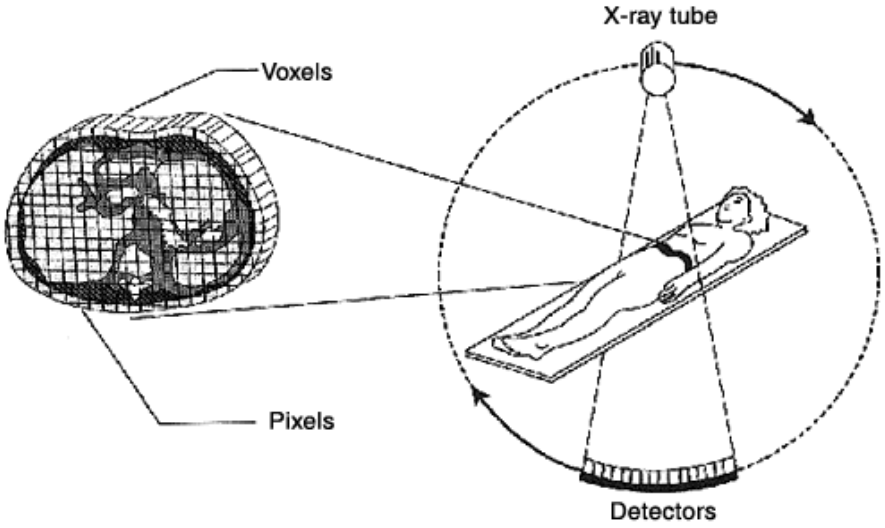

Figure 11: Geometry of the CT-scan. The x-ray tube and the detector are rotating around the axial axis of the patient [29].

2.1.2.1 Small animal CT

A micro-CT scanner is designed for higher resolution imaging. Most of the commercial micro-CT scanners use micro-focus X-ray tubes with focal spot sizes between 5-100 μm in a rotating gantry (tube and detector) design [30,31]. The spatial resolution in human CT scanners, on the other hand, is > 450 μm. Systems with a micro-focus X-ray source, as used in small animal imaging, require longer exposure times (order of minutes for small animals [32] compared to seconds for human CT [31]). This leads to increased radiation doses in order to achieve a reasonable SNR (more than >1 Gy can be reached [31]). Radiation dose also increases linearly by the 4^{th} power with an increase in spatial resolution. A resolution of 50 μm is about the limit for micro-CT, because higher radiation dose would be lethal to small animals [32]. However, the radiation dose is often high enough to affect the immune system and other biological pathways.

Recent micro-CT scanners use flat panel detectors [33,34], which offer high geometric stability and an optimized scan time, but at the cost of spatial resolution. A major challenge in CT is the low contrast between soft tissues. To increase contrast resolution, water-soluble iodinated contrast agents are used. However, they are rapidly cleared from the blood and due to the high heart rate of rodents (at least 10 times faster for mice than humans), most micro-CT systems are not capable of capturing a sufficient number of projection images during the first pass of an extracellular contrast

agent. Therefore, a new class of blood-pool contrast agent is now available [30]. Moreover, to use the diastole as the phase of the heart cycle, showing a minimum amount of motion, a temporal resolution of 50 ms is necessary, compared to 300 ms in humans [31].

2.2 Functional imaging techniques

2.2.1 Functional MRI (fMRI)

Functional Magnetic Resonance Imaging (fMRI) relies on the Blood Oxygen Level Dependent (BOLD) signal, which is known to be sensitive to variations in blood flow, blood volume and oxygen utilization. Because these variations reflect changes in neural activity in response to a stimulus, fMRI is a neuroimaging technique that can show us which regions of the brain are involved in a certain task or mental process. The widespread and successful application of BOLD fMRI to human brain imaging has been the result of the fact that it is a non-invasive technique, without the need for either exogenous contrast agents or tracers.

2.2.1.1 fMRI principles

When someone performs a certain task, there will be an increased blood flow in the brain region correlated with that task. In this way, the brain region receives more glucose as transported by the blood. Glucose serves as the brain's primary energy source, but is not stored by the brain itself. From oxidizing glucose, ATP can be formed, which is utilized in several processes. When neurons become active and action potentials arrive at the pre-synaptic cell, glutamate is released and opens ion channels at the post-synaptic cell. On the one hand, ATP is used by astrocytes for the re-uptake of glutamate from the synaptic cleft. On the other hand, ATP is used by the membrane pumps to pump out ions of the cell again in order to restore ionic gradients.

When more blood flows in to transport more glucose, there is also an increase in the oxygen supply in the form of oxygenated Hemoglobin in red blood cells. Since oxygenated Hb (oxyHb) is diamagnetic, it exerts no influence on the environment. Deoxygenated Hb (deoxyHb), on the other hand, is paramagnetic and disturbs the environment locally, resulting in a decrease in the signal compared to tissue with oxyHb. The signal decrease occurs because the T2* is shortened: the susceptibility difference between capillaries and surrounding as created by the paramagnetic Hb, creates a local magnetic field distortion that extends into the surrounding tissue and dephases the signal [35].

Summarized, when the neural activity increases locally, two phenomena occur (**Figure 12**). First, there is an increased cerebral metabolic rate for O_2 ($CMRO_2$), meaning that more oxyHb is consumed locally. Because the amount of deoxyHb is now slightly bigger compared to oxyHb, a small reduction in MRI-signal is identified. However, after some seconds, the blood flow is also increased locally, resulting in a high increase in oxyHb and a decrease in dexoyHb (**Figure 13**). In fact, the blood flow increases to a level where it overcompensates the increased O_2-demand. This results in a net increase in the oxyHb and a net decrease in the deoxyHb, meaning that the BOLD signal (=oxyHb/dexoyHb) is increased. The smaller amount of paramagnetic molecules (i.e. deoxyHb) results in a smaller distortion of the tissue environment compared to rest. Hence, the T2* is less shortened (in other words, it is increased compared to rest), creating an increased voxel signal intensity in the activated regions.

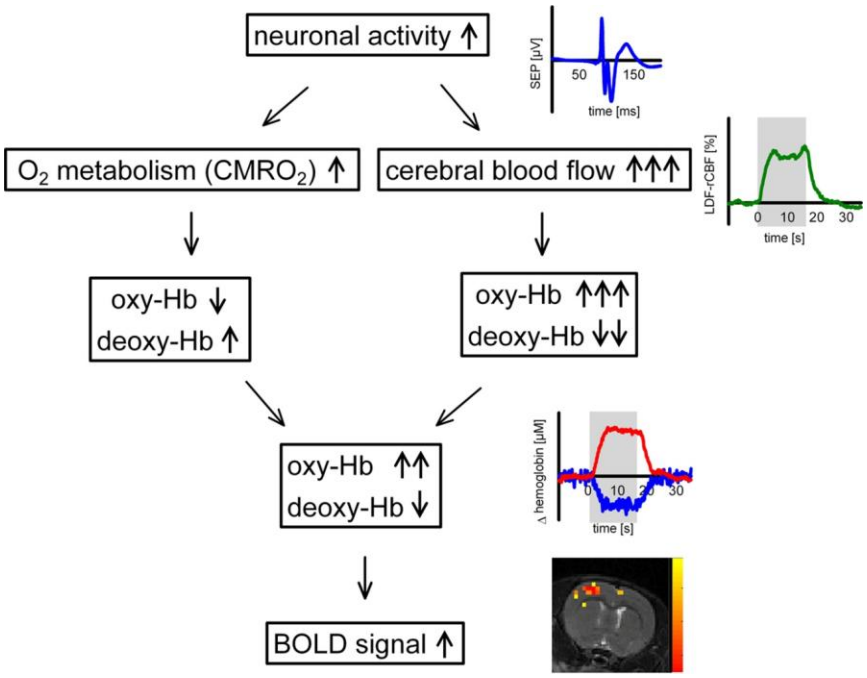

Figure 12: Physiology of the hemodynamic response during increased neural activity [36].

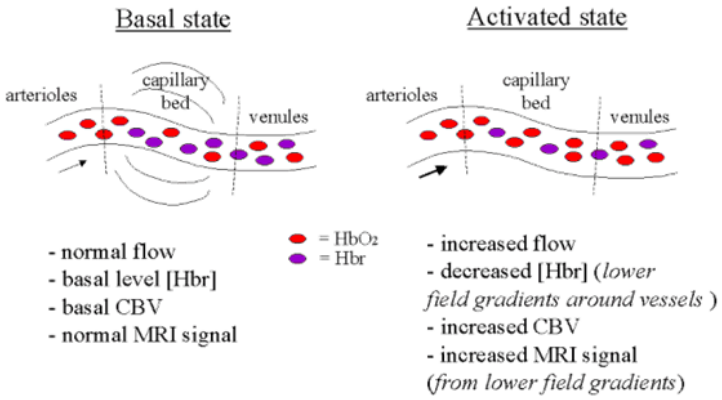

Figure 13: Overview of fMRI BOLD and the hemodynamic variables that change during neuronal activity. In the basal state, deoxyhemoglobin in the capillaries and venules causes field gradients around the vessels, resulting in a decreased signal intensity. In the activated state, the significant increase in flow in combination with a modest increase in oxygen consumption causes a lower concentration of deoxyhemoglobin in the venules and capillaries, resulting in a reduction in the field gradients. Hence, the signal intensity will be increased [37].

It is clear that due to neurovascular coupling mechanisms, neuronal activity triggers a variation in dilatation of vessels and thus in blood flow. However, the exact relationship between cerebral hemodynamic changes and the actual neuronal activation remained unknown for a long time. It was questioned whether the BOLD signal is more related to neuronal action potentials (AP's) or to local field potentials (LFP's). LFP's reflect the summation of post-synaptic potentials (be it excitatory or inhibitory) and thus represent a measure of synchronized synaptic input activity of a given neural population rather than neuronal firing rates. It is hypothesized by several studies [38,39] that BOLD seems to reflect the input to a neuronal population as well as its intrinsic processing, rather than its output (i.e. spiking activity). As an example in the rat, up to 95% of regional cerebellar blood flow increases might be dependent on postsynaptic activity [40].

Still, it remains a fundamental challenge for fMRI to interpret the magnitude of the BOLD response in a quantitative way in terms of the underlying physiological activity. Buxton et al. [41] concluded that the BOLD response alone is ambiguous, and cannot be interpreted reliably as a quantitative reflection of the underlying physiology. Calibrated fMRI needs to be used in combination with other techniques, such as Arterial Spin Labeling, in order to isolate effects of CBF and $CMRO_2$. The importance of the latter may not be underestimated since it is possible that CBF and $CMRO_2$ are acting in opposite directions (example is caffeine working on adenosine receptors [41]), resulting in an unchanged BOLD response, despite large changes in underlying physiology.

2.2.1.2 Hemodynamic Response Function

The combination of neuronal and hemodynamic effects can be represented in the Hemodynamic Response Function (HRF), which is a representation of the BOLD signal as a function of time (seconds) (**Figure 14**). After a certain stimulus is given, first an initial "dip" is seen. This dip lags the neuronal events by 1-2 seconds. It occurs because it takes that long for the vascular system to respond to the brain's needs for glucose. In a second phase, the BOLD signal rises and peaks after approximately five seconds. This is the moment when the blood flow peaks. When a stimulus would continue for a longer time, a plateau would be seen instead of a peak. When the activity stops, the BOLD signal decreases again and finally, a post-stimulus "undershoot" is remarked. This increase in deoxyHb concentration can be explained by the venous bed capacity, which tends to cause the regional blood volume normalize at a slower rate than the changes in blood flow [42].

It was shown in previous studies that the HRF of the rat is similar to the one of humans (with a response delay of approximately 2 seconds and a peak flow at approximately 5 seconds from stimulus onset) [43]. However, HRF's may differ between the awake and anesthetized rat. Martin et al. found that the HRF in awake rats rises faster, peaks earlier and returns to baseline more quickly in comparison with the anesthetized condition [44].

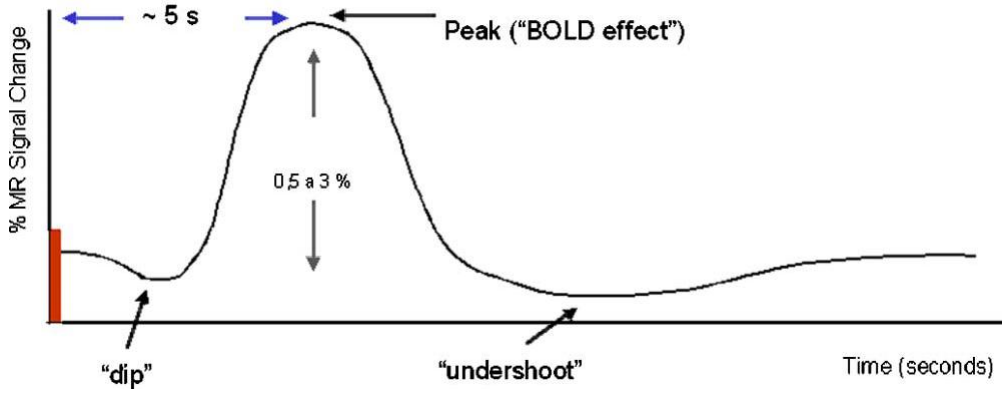

Figure 14: Hemodynamic response function from a short duration stimulus (red bar). The BOLD effect peaks at approximately 5 seconds from the stimulus [42].

2.2.1.3 Echo Planar Imaging (EPI)

Due to the rapid changes in physiologic parameters (CBF, CBV and $CMRO_2$) during brain activation, a fast imaging technique is required. The Echo Planar Imaging (EPI) technique is pointed out to be the fastest acquisition method in MRI (60-100 ms/slice) [45]. It results in a total of 10 to 16 images per second. The fact that EPI is so fast is due to the rapid gradient switching to acquire all frequency-encoding points as well as phase-encoding steps during a single pulse cycle. This means

that the entire 2D image is collected in one TR and therefore the technique is also called “single-shot”. The contrast in EPI is acquired through a GE or SE sequence.

SE sequence During the recovery period, the decaying spins emit their energy, which can be detected by RF coils. Since the measured signal is proportional to the net transversal magnetization in a SE-sequence, inhomogeneities in the magnetic field result in signal loss. Indeed, dephasing during T2-relaxation results in nuclei pointing in every direction of the transversal plane. However, signal loss can be recovered by “refocusing”, meaning a gradual re-alignment of the nuclei in the transversal plane. This is achieved by sending a 180° radio wave pulse. The slower spins will now catch up the faster ones and a maximum signal can be measured. The recovered signal is called an “echo”. A classic “spin-echo” (SE) sequence is depicted in **Figure 15**. With this type of echo, only the decay due to local field inhomogeneities is recovered and not spin-spin interactions. Hence, the T2 decay can be measured.

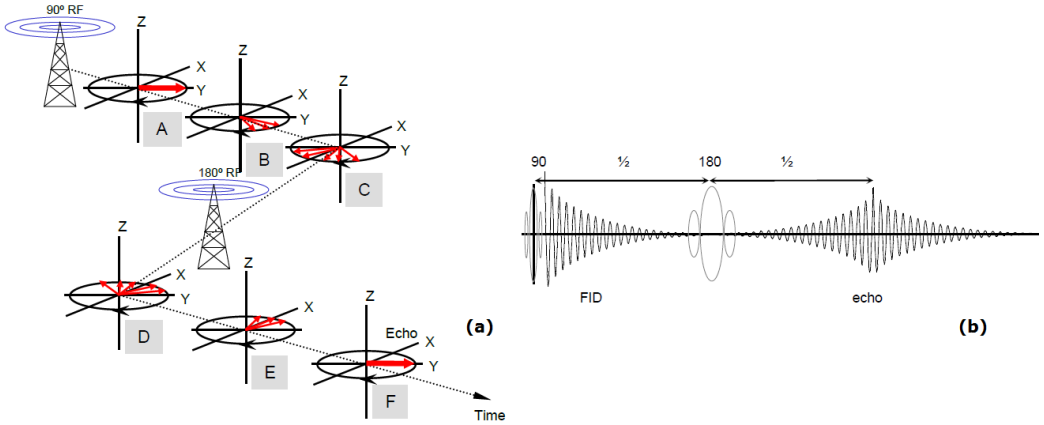

Figure 15: a) SE sequence: A. It starts with a 90º excitation pulse. The magnetization is flipped into the X-Y-plane. B. Immediately the spins dephase… C. The spins dephase a bit more… then a 180 rephasing pulse is given. D. The spins are mirrored around the Y axis. E. The spins rephase until… F. The spins are in phase again creating an “echo” [19]. b) After the 90° pulse, an 180° rephasing pulse is given, resulting in a high signal (echo).

GE sequence The sequence that will be of most use in this thesis, is a variant on the SE-sequence, namely the Gradient Echo (GE) sequence (**Figure 16**). In this case, the echo is formed by applying a flip angle (FA) between 1° and 180°, depending on the desired contrast. In order to achieve controlled, transverse dephasement of spinning protons, a negative gradient is applied. Afterwards, a positive readout gradient is applied until the dephased protons again re-align with the B_0-field. A signal can be acquired now. With this type of echo, only the decay due to the gradient field is recovered and not the spin-spin interactions nor the field inhomogeneities. Hence, the T2* decay can be measured. The echo time (TE) is of great importance in a GE sequence. T2*-contrast requires a small FA and a long TE, while it is the other way around for T1-contrast.

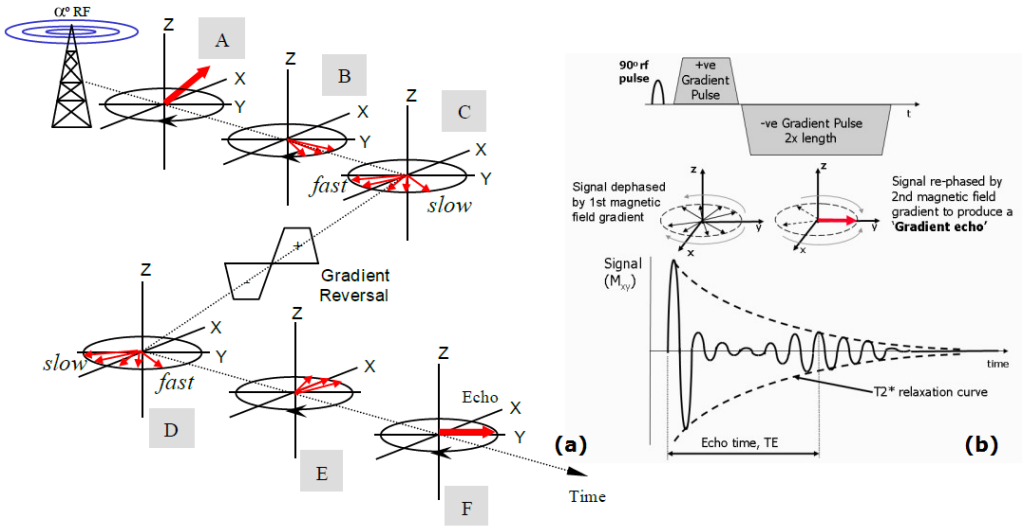

Figure 16: a) GE sequence: A. Start with a FA α. Depending on α, more or less magnetization is flipped into the X-Y plane. B. The spins are dephasing… C. And dephase a bit more until the polarity of the GRO is changed after which… D. The spins rephase… E. And rephase a bit more until… F. The spins are in-phase again [19]. b) The reversal of a magnetic field gradient can be used to generate a gradient echo [46].

In many of the functional imaging studies, GE is preferred over SE because of its increased sensitivity for both large vessels and small capillaries at 7 T and above [47,48]. However, there are also studies arguing that SE is preferable at 7 T due to its better spatial specificity, because the BOLD response originates solely from the extravascular dynamic dephasing component [49,50]. The fact that SE is thus weighted towards microvasculature makes it useful to depict changes in capillary deoxygenation in fMRI. Also, SE-EPI is less prone to geometric distortion and signal loss due to magnetic field inhomogeneities [51]. Therefore, SE-EPI would be an applicable imaging technique when electrodes are implanted in the brain, because they are susceptible to create severe signal dropout. However, an important reason of preferring GE is that it better covers the brain [52]. This means that for the same TR, it is possible to acquire more slices during a single acquisition. GE sequences have generally much shorter TR's than SE, so they have shorter scan times [53]. Furthermore, the gradients as used in GE can rephase the protons very quickly, compared to the 180° pulses in SE. This results in a shorter TE.

Slero et al.[54] have compared the spatial activation maps and time courses of the GE and SE HRF upon a short visual stimulation at 7 Tesla (**Figure 17**). The SE contrast showed clearly a reduced sensitivity. The SE and GE HRF showed similar onset time and rising slope at cortical depths > 1mm. This is the space where most of the microvasculature is located, indicating that GE-BOLD is weighted towards the microvasculature in the early phase of the response in deep gray matter. Macrovascular dynamics become observable at the later phase of the response and are predominant in the surface gray matter.

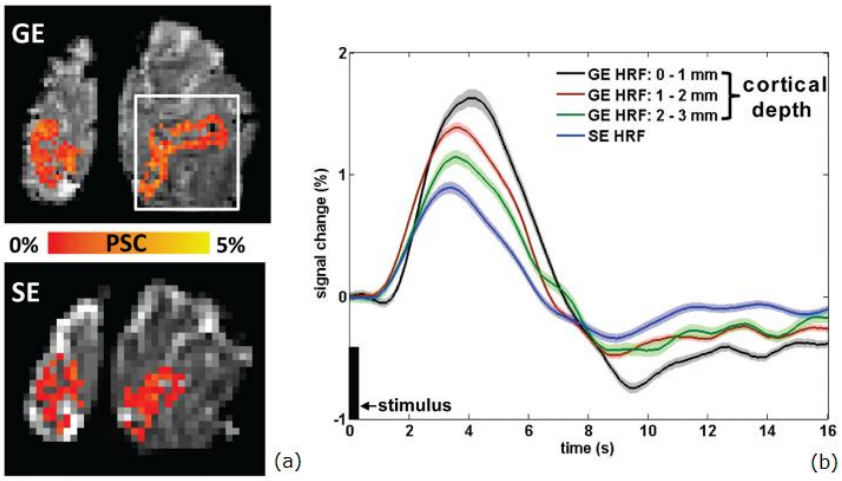

Figure 17: a) Spatial activiation maps showing the percent signal change (PCS) of the visual cortex V1 and b) time courses of the GE and SE HRF upon short visual stimulation at 7 Tesla [54].

GE fMRI produces T2*-weighting images, unlike in SE where image contrast is dedicated by T2. This can be explained by the fact that the gradient as used in GE does not compensate for magnetic field inhomogeneities [47]. The amount of T2*-weighting depends on TE (**Figure 18**). Yacoub et al.[12] have tried multiple TEs in a BOLD fMRI study (7 Tesla) of the human visual cortex. It was concluded that T2* was 25 msec and that this was also the optimal TE. Also van der Zwaag et al.[55] found that the percentage signal change between rest state and performing a motor task (7 Tesla) peaked at TE ~ T2*.

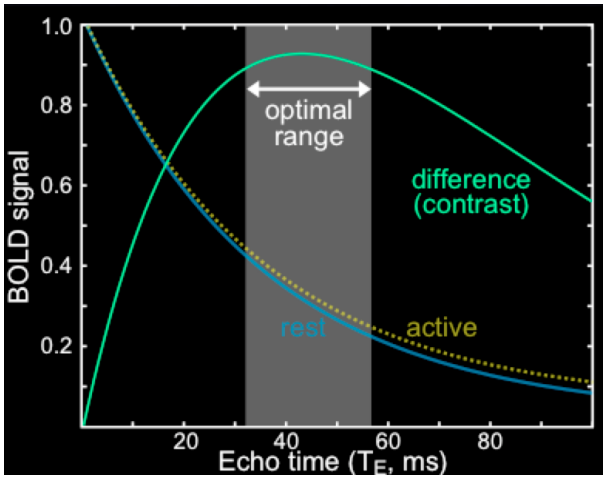

Figure 18: Contrast depends on the optimal Echo Time (TE). A greater signal change is seen for a longer delay.

2.2.1.4 Experimental design

In order to visualize certain brain regions, the patient has to fulfill a certain task (eg. fingertapping) or a stimulus can be given to the region of interest. 'Paradigm' or 'design' describes the way how tasks/stimuli are constructed or organized during the experiment. The most known designs are the block-design and the event-related design (**Figure 19**). The block-design uses two or more conditions which are alternated (eg. 30 seconds "on" and 30 seconds "off") in order to determine the differences between the active and rest state. When there is an overlap between the individual HRF's from different stimuli, the amplitude of the BOLD response increases. However,

there is also some kind of threshold related with the BOLD effect, meaning that if the frequency of the stimulus becomes too high, there is no linear increase in amplitude anymore. This indicates a saturation of the BOLD effect [62]. The other frequently used design is the event-related design. Here, discrete stimuli or responses are repeated and averaged over different trials to give a measurable response [37].

Some advantages of the block-design are a high statistical power and a relatively large BOLD signal change compared to rest. A disadvantage involves that the lack of randomization makes this design more predictable for the patient in *what* will happen *when*. Surely this can result in a decreased attenuation level across the experiment. However, this disadvantage is of no importance in this study. An event-related design, on the other hand, varies randomly in the kind of stimulus as well as in the time between two stimuli. Another major advantage is the ability to detect the HRF from a single event type, which can be analyzed in detail.

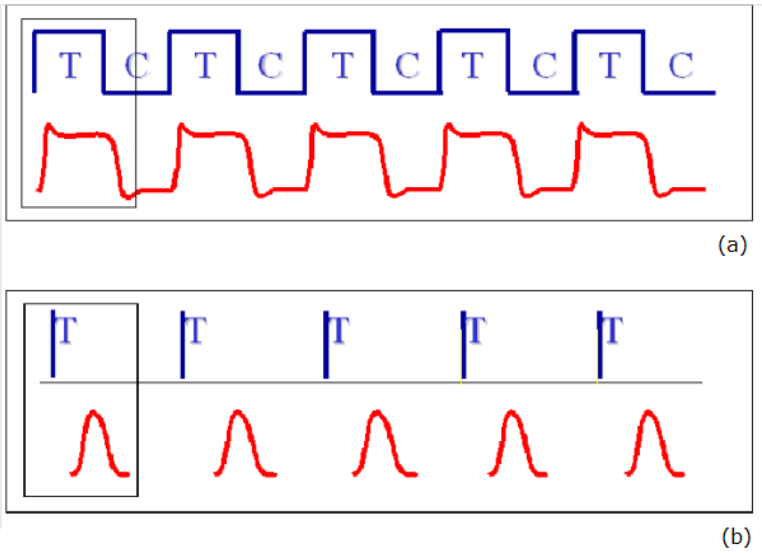

Figure 19: a) Block-design, b) Event-related design [42].

2.2.1.5 Limitations & Challenges

The BOLD technique is unfortunately also accompanied by some limitations due to the complex interplay between blood flow, volume and $CMRO_2$. The first major limitation includes the fact that the vascular response to activity is always delayed (5 seconds until the peak in the HRF). Therefore, the temporal resolution is inherently limited, corresponding to a TR that is never less than one second [42]. A TR of about 1.25 to 2 seconds at minimum would be ideal to cover the whole brain, since in this case approximately 20 slices of 5 mm thickness are required [56]. However, fMRI shows still relatively good temporal resolution compared to other functional imaging techniques such as PET, which has a temporal resolution in the range of minutes. The second limitation is caused by the existing distance between activated neurons and the vascular variation in the BOLD ratio. This results in an imprecise localization of the activation zone. Moreover, the fast collection of brain slices as achieved in EPI, goes at the expense of a large brain coverage. Hence, the trade-off between spatial and temporal resolution can be challenging.

Different parameters affect the signal-to-noise ratio (SNR) of the fMRI-images. The influence of the voxel volume (=ΔXΔYΔZ) can be illustrated with the aid of the formula for SNR:

$$\mathrm{SNR} \sim \Delta X \Delta Y \Delta Z \sqrt{NSA}\ \frac{\sqrt{Nx * Ny}}{\sqrt{v}} \qquad (3)$$

whereby ΔX and ΔY represent the voxel dimensions in x and y, ΔZ is the slice thickness, Nx and Ny represent the sampling matrix size in the x and y directions, NSA is the number of signal averages,

and v represents the acquisition bandwidth (one over the sampling rate of the data acquisition) [57]. Decreasing the FOV or increasing the matrix size[3], results in an increase of the in-plane resolution (i.e. FOV/matrix size becomes smaller) but in a decrease of the voxel volume. The latter corresponds to a decrease in SNR according to the formula. Decreasing the slice thickness also results in a decrease in SNR. In fact, the three fundamental factors that determine design and applications of MR imaging for a given contrast, are imaging speed, SNR and spatial resolution [58]. Changing one of them will affect the other two and vice versa.

Another impact factor is the magnetic field strength. Increasing the latter results in a larger initial magnetization vector and hence in a larger change of BOLD amplitude. One can conclude that a higher Tesla-system corresponds to an increased SNR [55,59]. The discovery of this fact has led to scanners with a magnetic field strength up to 9 Tesla nowadays. However, high field scanners are prevented from use in clinical practice due to increasing magnetic susceptibility artefacts. Moreover, there is an increased inhomogeneity of both the main field (B_0) and the RF transmit field (B_1), and there are more patient contraindications (increase in SAR). The field inhomogeneities cause image distortion and signal loss. They can arise at air-tissue interfaces or near sinuses, because these tissue types all interact in another way with the static magnetic field. Shimming can be applied to compensate for the susceptibility gradients at the interfaces. Active shimming involves the positioning of shim coils inside the permanent magnet that add small magnetic fields to the static magnetic field, thus making the total field more homogenous. Passive shimming, on the other hand, is done during the installation of the scanner by the positioning of steel plates around the permanent magnet. These plates get magnetized and can compensate for inhomogeneities by producing their own magnetic field. Shimming is done before data acquisition. This can be linear or higher-order shimming [60]. The corrective shim currents are calculated by minimizing the spatial standard deviation of the magnetic field and they are represented in field maps [61]. These field maps are acquired by a dual echo-time EPI sequence and depict the off-resonance frequency at each voxel.

Finally, the choice of head coil has an impact on the SNR. The RF coil acts as a transmitter of the RF excitation (B_1) and as a receiver of the produced MR signals. It is designed to confine the RF magnetic field to the imaged volume. Two types of coils are generally used: volume coils and surface coils. Volume coils are used for brain imaging and provide consistent intensity and contrast across the entire FOV (compared to surface coils) [63]. A common configuration is the birdcage coil (**Figure 20a**), which is used in this thesis for the rat brain. It consists of a number of wires along the z-direction and is able to create a highly uniform radiofrequency field. Recently, phased-array coils are more and more used in neuroimaging studies (**Figure 20b**). It is a combination of several surface coils (coil elements) with a high improvement in SNR. Increasing the number of channels (up to 32) improves the SNR even more.

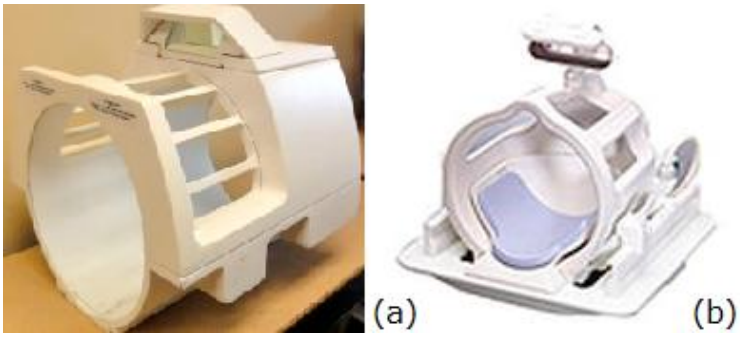

Figure 20: a) Birdcage head coil, b) phased-array head coil (8 channels).

3 The FOV corresponds to the voxel size in the x- and y-direction. The matrix size corresponds the number of phase encoding steps in the y-direction and the number of frequency encoding steps in the x-direction.

2.2.1.6 State-of-the-art

Functional magnetic resonance imaging is a non-invasive technique to measure and map global brain activity. Task-related fMRI studies attempt to find the patterns of brain activity that are associated with mental processes of interest. Statistical maps can be constructed of the task-dependent activation. Besides task-related fMRI studies, also resting-state fMRI experiments have been conducted to investigate the functional connectivity of the brain [64,65]. Functional connectivity is defined as the temporal dependency between spatially remote neurophysiologic events [66]. It was discovered by Dr. Raichle in the 90's that the brain uses approximately 20% of the entire body's energy at rest. Many functions of the brain are interlinked and not localized to one specific area. Therefore, fMRI is interesting in that it can visualize the functioning of the *whole* brain. Resting-state fMRI has been studied for the assessment of brain plasticity [67], brain ageing [68], epilepsy [69] and brain tumours [70]. Since 2003, functional connectivity analysis has been conducted, especially in patients with epilepsy [71]. It can be described by graphs with nodes and edges. Connectivity density is measured by a clustering coefficient and the distance between any two nodes is described by the characteristic path length.

The role of fMRI in cognitive neuroscience became especially important for the understanding of the brain plasticity, both in the context of normal development and in response to injury. As an example, Bedny et al.[72] have shown that congenitally blind individuals also activate the visual cortex in some verbal tasks. There was an increase in BOLD-signal in the visual cortex similar to that in the language processing areas of the brain. Indeed, the brain has the ability to adapt in the event of damage and it was concluded in the study that regions that are thought to have evolved for vision can take on language processing. Recently, the evolving understanding of psychiatric diseases as being disorders in *brain circuitry*, has led to an increased use of functional imaging also in the domain of mental illness [45,73]. Looking to the future, fMRI will play a role in defining neuromechanisms that are linked to genetic variation [74,75]. Neural systems that may mediate genetic risk in neuropsychiatric disorders, will be delineated by the aid of functional imaging.

2.2.1.7 Micro-fMRI

Animal fMRI studies suffer from decreased contrast-to-noise ratio compared to human studies, because smaller voxel sizes and smaller size of the activated areas result in a decrease in SNR, according to formula (3) [76]. In order to increase the SNR and BOLD signal change, small animal imaging is conducted at higher field strengths (7 Tesla in this study). It is also assumed that the contribution of capillaries to the BOLD effect becomes more important at higher fields (**Figure 21**) [77]. Consequently, the direct relationship between BOLD signal change and field strength holds not above 7 Tesla, because vascular contributions from the larger arterioles and venules are then decreased. The Bruker BioSpin PharmaScan (7 Tesla) (**Figure 22**) that is used in this study has a relatively high spatial resolution up to 50 μm [78]. This further enhances the BOLD amplitudes because of the smaller partial volume effects. However, resolution of fMRI is rather limited compared to MRI. A large drawback of micro-MRI is the cost. The superconducting core has to be cooled by liquid helium, which has to be replaced every several weeks [79]. Also the purchase of the scanner itself is a large cost. Another disadvantage involves the acquisition time, which can extent to a few hours due to the required high spatial resolution in small animals. This can affect rodents that are anesthetized during this time period.

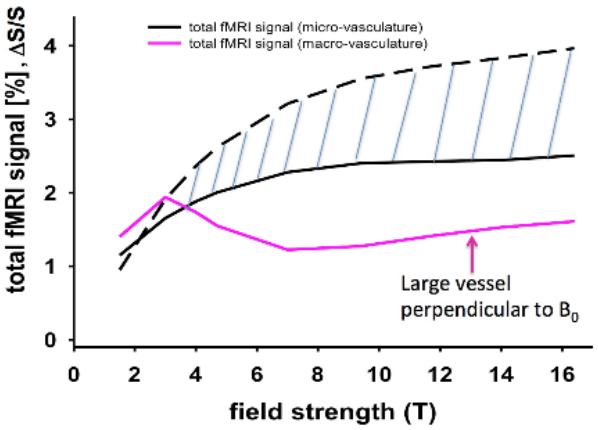

Figure 21: Simulation results for SE fMRI for TE= T2 as a function of field strength. Total fMRI signal (considering intravascular and extravascular effects) is shown in black for microvasculature assuming no stimulus induced CBV change (dashed line), and 16% microvascular CBV change. Most probable scenario is between these two extremes. Total fMRI signal for macrovasculature is shown in magenta for the extreme case of a vessel oriented perpendicularly to the static magnetic field, which causes the maximum effect. Microvascular CBV was taken to be 2.5% and was assumed to be composed of 20% arterioles (diameter = 16 µ), 40% capillaries (diameter = 5 µ), and 40% venules (diameter = 16 µ) [80].

Figure 22: Bruker BioSpin PharmaScan (7 Tesla).

A challenge specific for small animal imaging, is the need for animal immobilization by anesthesia during imaging. Anesthesia plays an important role in functional imaging because of two reasons. First, there is a great difficulty in fixing the head of a conscious animal. The absence of any movement is important to avoid motion artefacts which can blur the image or create ghostings. Secondly, the firm stereotactic positioning would induce discomfort and stress in the animal. Because the animal will suffer from increased discomfort or pain at the site of stimulation, this will lead to a more complex (widespread) and higher bilateral activation pattern compared to the anesthetised case [81]. This makes a correct interpretation of the actual effects as seen on fMRI more difficult. Moreover, the repetitive noise of gradient switching during fMRI will affect the awake animal much more than the anesthetised one. Acoustic noise can result in an increased signal intensity in the somatosensory cortex [82]. In order to exclude those factors, anesthesia has to be used during imaging.

General considerations for anesthetics include the ease of administration, the extent to which the anesthetic influences neural activity and the suitability for longitudinal use. Isoflurane is the most common anesthetic used for longitudinal, small animal imaging studies because it is safe and easy to use. However, it might be not the first choice in *functional* imaging, due to its suppressive effect on neuronal activity. Other anesthetics that have been used in the past for imaging include alpha-chloralose, medetomidine, ketamine and the more upcoming sevoflurane.

Isoflurane Isoflurane shows potential for longitudinal studies and the BOLD-response to forepaw stimulation can be detected under low levels of anesthesia [83,84]. Because it is an inhalant anesthetic, the delivery rate is constant and there is a rapid recovery possible [85,86]. Considering the influence of isoflurane on vascular responses, it acts as a strong vasodilator, thereby increasing the baseline CBF. This suppresses the BOLD signal at dosages >1 MAC (1.38%) in fMRI experiments [83]. Moreover, the response location can be very unstable. Considering the influence on neuronal activity, isoflurane shows a great difference between the awake and anesthetised state on the EEG [87]. Isoflurane stimulates the glial cells to take up more glutamate from the synaptic cleft, thereby reducing the excitatory synaptic transmission. Higher concentrations of isoflurane induce hyperpolarization of the neuronal membrane and accelerate cortical oscillations [88]. In this case, bursting activity and long silent periods of flat EEG alter each other, also called "burst suppression" (**Figure 23**). Hence, high levels of isoflurane suppress neuronal activity to a greater extent.

Alpha-chloralose Alpha-chloralose has been widely used as an anesthetic for fMRI studies in the rat. It provides a stage of deep sedation [89] while preserving hemodynamic activity and a strong BOLD-response during forepaw stimulation [90]. Moreover, alpha-chloralose sharpens the contrast between activated and non-activated units [91]. However, this anesthetic can cause acidosis and seizure-like activity [92]. Other disadvantages are the invasive intubation and catherization for intravenous delivery of the anesthetic, resulting in a very long recovery time for the animal [92,93]. These things contribute to the fact that alpha-chloralose cannot be used in survival or repeated studies [94]. Only one study has proposed a new formulation of alpha-chloralose, administered through the tail cannula, that allows repeated fMRI studies in the same animal [95]. Finally, the slow onset of activation makes it difficult to estimate the real depth of anesthesia [89].

Medetomidine Another, more recent candidate anesthetic for fMRI studies is medetomidine, particularly because of its possible use in longitudinal studies [96]. Indeed, the anesthetic is delivered subcutaneously without catherization and the animal can breathe freely without intubation [97]. Medetomidine provides a reliable sedation (rather than being under full anesthesia) as well as analgesia, muscle relaxation, and anxiolysis [98,99]. The sedative effects are mediated by binding to alpha2-adrenoreceptors primarily located in the locus coeruleus, thereby inhibiting the release of norepinephrine necessary for neurotransmission. Moreover, medetomidine exhibits a rapid distribution (order of minutes) to the brain, resulting in good control of the depth of anesthesia [100]. The animal can recover fast (2 minutes) after an intraperitoneal injection of the antagonist atipamezole [83,92]. Considering the influence on vascular responses, medetomidine acts as a vasoconstrictor of pial arteries and veins, resulting in a decrease of baseline CBF and CBV [101]. In response to stimulation, veins dilate again and there is an increase in venous CBV. This reduces the BOLD response to a certain extent, but the percent BOLD response remains higher than under isoflurane. It was stated by Chao et al.[83] that a reasonable time window for BOLD-fMRI responses is 1-2 hours when using a constant infusion rate. However, Fukuda et al.[101] have found that a constant infusion of dexmedetomidine (50 μg/kg/h, which is equivalent to 100 μg/kg/h medetomidine) for longer than 120 minutes can result in epileptic activities during forepaw stimulation. It was showed by the authors that supplemental isoflurane administration of ~0.3% again increases the seizure threshold. The fact that dexmedetomidine decreases seizure threshold and works proconvulsive has been investigated earlier by Mirski et al [102]. They have confirmed that inhibition of central noradrenergic transmission facilitates seizure expression. Pawela et al.[100] found that a constant infusion of medetomidine at 100 μg/kg/h is not sufficient to maintain sedation beyond 3 hours. They saw that by stepping the infusion dosage from 100 to 300 microgram/kg/h after 2.5 hours, experiments as long as 6 hours are possible.

Summarized, medetomidine is the preferable anesthetic during longitudinal fMRI studies in the rat, since isoflurane strongly suppresses neuronal activity and reduces hemodynamic responses, while medetomidine yields more robust hemodynamic responses.

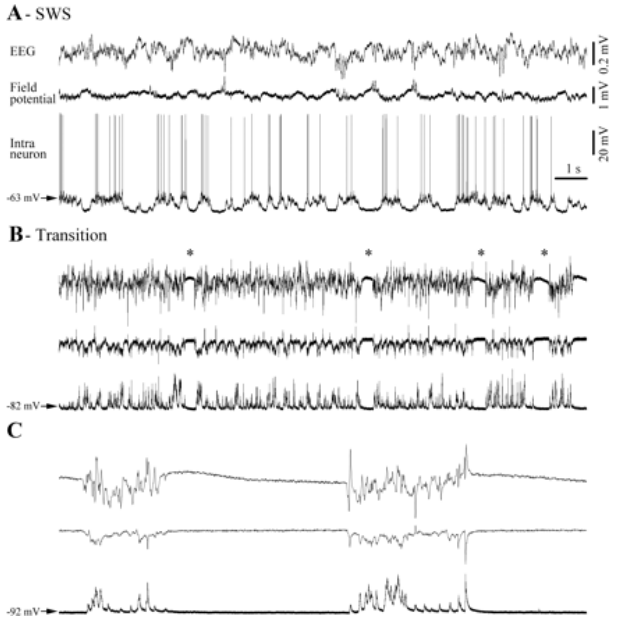

Figure 23: Progression towards a "burst suppression" (BS) pattern, as recorded on an EEG: A) Light anesthesia (1.5% isoflurane) causes slow-wave sleep-like oscillations dominated by a quasi regular slow rythm of <1 Hz. B) Transition period when going from light anesthesia to higher concentrations of isoflurane (2.5%). This induces hyperpolarization of the neuronal membrane and accelerates cortical oscillations. Some short periods of flat EEG (as depicted by *) can be detected. Those periods become longer and more frequent. C) Stabilized pattern of BS, during which bursting activity and long silent periods of flat EEG alter each other [88].

2.2.2 Positron Emission Tomography (PET)

The goal of PET-imaging is to obtain a (quantitative) image of the distribution of a certain molecule in the body [103]. In a *dynamic* PET study, the data include a time series of volumetric images that reflect the distribution of the radionuclide over time. Hence, both spatial and temporal information are acquired in a single study. Kinetic tracer models can be used to calculate clearance, metabolism, rate of accumulation, etc. [104].

PET-imaging is a non-invasive technique which enables visualization and quantification of molecular processes *in vivo*. The major strengths of PET are its high sensitivity and absolute quantification capability; however its spatial and metabolic resolution stays rather limited. The number of PET studies has steeply increased during the last decade and it has become a useful technique in the detection and follow-up of tumours.

2.2.2.1 Principles

PET is based on the tracer-principle, meaning that radionuclides (radioactive isotopes) are used to quantify physiologic parameters in the body. Biological substances are labeled with such a positron emitting radionuclide and together they form a radiotracer (or radiopharmaceutical). The most known radiotracer for PET-scans is F-18 fluorodeoxy-D-glucose (F-FDG). The amount of uptake of the tracer by certain cells or organs is reflective of the regional glucose metabolism. This is also the reason why tumour cells are good visible with PET: the malignant cells have an increased

metabolism and show a large uptake compared to healthy cells. The radiopharmaceuticals are mostly intravenously injected (non-invasive technique) and they are very specific. Another advantage of PET is that the radiopharmaceuticals do not harm the normal function of the biological substance itself.

When distributed into the body, the proton-rich isotopes may decay to a neutron, a positron ($ß^+$-particle) and a neutrino. After a short distance in tissue (i.e., the positron range, typically a few tenths of a millimeter), the positron undergoes an annihilation reaction with an electron and two gamma-rays of each 511 keV are emitted (**Figure 24**). These rays travel in opposite direction along a line of response (LOR). A pair of scintillator detectors, installed in a ring-like pattern, register both incident photons and generate a time pulse. The pulses are said to be "coincident" if they both lie within a certain short time interval. When the scanner registers multiple of these coincident lines, the emission distribution can be projected and calculated by image reconstruction techniques [103]. The "electronic collimation" technique increases the sensitivity of the detection process compared to other imaging techniques (such as "mechanical collimation" in SPECT). The image that is finally formed will quantify the concentration of a certain molecule in different parts of the body. There are no individual molecules measured in PET. In order to compensate for relatively low spatial resolution (centimetres), PET can be combined with CT or MRI [105].

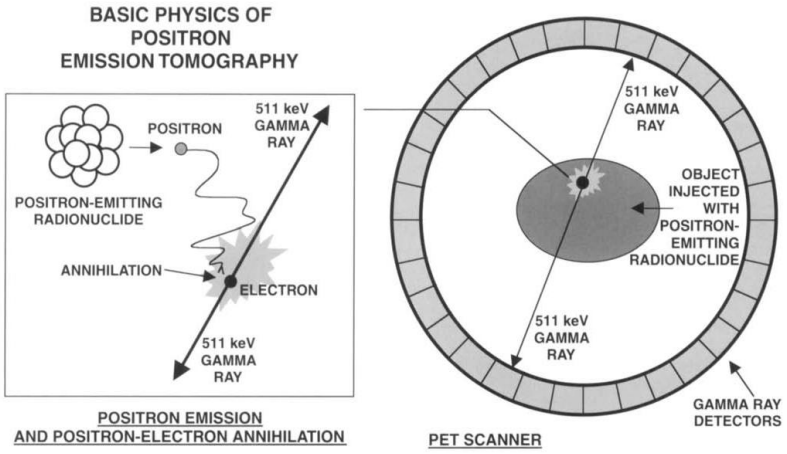

Figure 24: Basics of positron emission tomography (PET).

2.2.2.2 Quantification

PET quantification begins with knowledge about the radioactivity levels in tissue, which do not necessarily relate to the underlying tissue function [106]. This is because other factors, such as regional blood flow, binding site activity, enzyme activity,... may contribute to the local amount of radioactivity. Tracer kinetic modelling provides a link between the measured activity levels and the physiological parameters of the (function of) the tissue or organ. These models make use of compartments to describe different pathways from free tracer to the trapped product.

In animal studies, the biodistribution of radiotracers is usually expressed by percent injected dose per gram of tissue (%ID/g). This is calculated by the following formula:

$$\frac{\%\ \text{ID}}{\text{g}} = \frac{\text{activity in a gram of tissue (MBq/g)}}{\text{injected dose (MBq)}} \times 100 \qquad (4)$$

This formula does not take into account the total body weight of the animal. Different corrections have to be applied in order to achieve reliable quantitative information about the whole-body biodistribution of the tracer. Several image degrading effects are possible in PET such as attenuation, scatter and randoms, partial volume effect and dead time.

2.2.2.3 Challenges in PET

One of the challenges of using radionuclides in PET is their short half-life. Their fast decay requires that both synthesis of the radiolabelled molecule and imaging take place very rapidly. The advantage of using ^{18}F as a radioactive isotope is that no *on-site* cyclotron is required. Instead, they are available through commercial radionuclide distribution centres (within 200 km). With a short half-life of 109 minutes, ^{18}F cannot be used for in vivo imaging of biomolecules with slow pharmacokinetics. In this context, 89Zr has gained attention over the last several years. It exhibits a half-life of 3.27 days, making it an attractive radiotracer for in vivo imaging of antibodies, nanoparticles and other large bioactive molecules [107]. Besides, there is a need for some kind of universal probes that can monitor many different molecular processes. An example is the synthesis of a small DNA-segment labelled at one end. The sequence of the DNA determines what process the probe will measure. However, this approach is still in early stages of development [108].

Optimal correction of the partial volume effects, i.e. the underestimation of activity concentration due to the limited spatial resolution of PET, remains challenging. It mainly affects lesions with sizes less than 2.5 to 3 times the resolution, as well as sharp edges of an object [109]. A promising solution would be crystals with different layers or the possibility to measure the depth-of-interaction (DOI) of a photon in a detector [103]. There exists a commercial clinical PET scanner (HRRT, Siemens Medical Solutions) that can determine DOI in brain imaging [110]. Several recent studies have also tried to correct for the factors that influence spatial resolution (besides DOI), namely positron range [111,112] and acolinearity [113]. Another challenge in PET involves the inaccuracy in attenuation correction due to possible mismatch between CT en PET images [109]. This would lead to a difference in actual and apparent activity concentration in a certain source object.

2.2.2.4 Micro-PET

Since the advance in mouse genomics and the wide range of small animal models of human disease in the mid 90's, PET has extended to small animal imaging (micro-PET). Therefore, the spatial resolution must be improved considerably and the scanner must become more compact, less expensive and easy in use. Over the past years, the spatial resolution of PET has been increased by the use of smaller scintillator crystals and spatial localization has been improved due to the combination of PET with CT. Micro-PET enables to obtain a statistical significant biodistribution from a *small amount* of animals and enables to do repeated studies in a single subject. The most extensive application of micro-PET imaging to small animal models of disease is in the area of oncology (tumour detection and follow-up). Micro-PET is able to monitor genetic and cellular processes *in vivo*. Because repeated imaging of the same animals is possible, quantitative information about migration and expansion of tumours can be acquired over time.

A challenge specific for small animal imaging, is the need for animal immobilization during imaging. This can be accomplished by restraining devices, which unfortunately alter the metabolic rate of the animal and thus make the interpretation of the actual glucose utilization more difficult. The same holds for the use of anaesthetics, which show confounding effects on cardiovascular, respiratory and central nervous system.

2.2.3 Electroencephalography (EEG)

2.2.3.1 Recording an EEG

EEG measures the weak electrical fields on the scalp surface as produced by electrical brain activity. Millions of neurons have to fire together in a synchronized way to produce a voltage signal. More in specific, it are the synaptic currents of the pyramidal neurons cells inside gray matter,

oriented in parallel and perpendicular to the cortex, that are the main EEG generators (**Figure 25**). Their electrical signal can be measured by electrodes that are placed in standard positions on the scalp. This results in a time course of the potential between an amount of chosen electrode pairs, also called an electroencephalogram (**Figure 26**). An EEG can also be obtained in a more invasive way by implantation of an electrode in the skull.

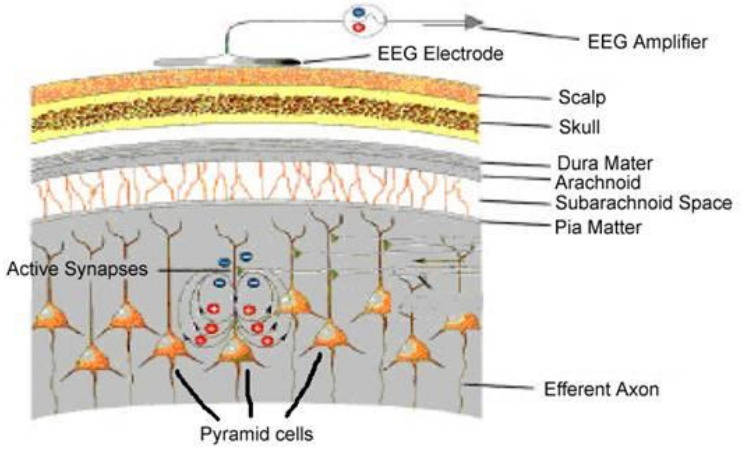

Figure 25: Pyramidal cells are the main EEG generators. They are located in the gray matter and oriented in parallel and perpendicular to the cortex.

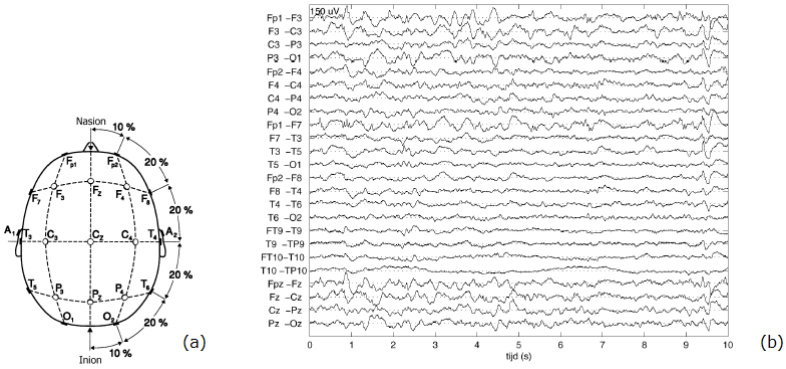

Figure 26: a) Electrodes are placed in standard positions on the scalp (10-20 system), b) Recorded EEG, which shows the time course of the potential between an amount of chosen electrode pairs.

2.2.3.2 Advantages and disadvantages of EEG

The major advantage of EEG is its high temporal resolution (millisecond-range), which is important for determining the precise moments at which electrical events take place. Because fMRI has more poor temporal resolution (seconds to minutes) but relatively high spatial resolution (micro- to millimeters) in high field small animal, this technique can be combined with EEG in order to acquire both high temporal and spatial resolution. EEG-fMRI can suffer from some artefacts, due to the interaction of the magnetic field with the currents. First, a gradient artefact can arise due to the switching magnetic field in fMRI sequences. Secondly, ballistocardiographic artefacts are possible due to small movements related to blood flow. It is important that these artefacts are detected and removed.

An important disadvantage of EEG recording is the poor spatial resolution (centimeter-range), which is especially problematic in small animal studies. EEG is even more difficult to record on small animals because their heads are too tiny for a traditional EEG cap of 27 up to 256 channels. An

adequate number of electrodes is however essential to record very localized activity as well as to analyze accurately the distribution of more diffuse activity and large-scale changes in neuronal activity [114,115]. Finally, EEG has a limited ability to detect epileptic activity from deep brain structures (e.g. hippocampus, basal ganglia). The latter can be compensated in an EEG-fMRI study because fMRI is equally sensitive to both superficial and deeper structures. In small animals, simultaneous EEG-fMRI is however limited to only a few electrodes because of the small available scalp area, but also because the electrodes are very near the brain tissue. When a large amount of electrodes are placed within a few centimeters, high magnetic field disturbances would be produced that can affect MRI signaling [115].

2.3 Deep Brain Stimulation (DBS)

Deep brain stimulation (DBS) is a neuromodulation technique whereby low-voltage electrical pulses are delivered to deep structures of the brain to treat certain disorders such as movement disorders (e.g. Parkinson's Disease [116-118], dystonia [119,120]) or pain syndromes [121,122]. The idea of neuromodulation is to "modulate" certain brain targets in order to correct for abnormal brain activity. Today, there is a lot of ongoing research on the role of DBS in psychiatric disorders (e.g. depression [123,124], obsessive-compulsive disorders [125,126]) and refractory epilepsy [127,128]. Other neuromodulation techniques besides DBS include Cortical Electrical Stimulation (CES), Transcranial Magnetic Stimulation (TMS [129]) and Vagus Nerve Stimulation (VNS).

2.3.1 Implantation and hardware

In DBS, electrodes are implanted in the deep nuclei of the brain, such as the hippocampus or the anterior and centromedian nucleus of the thalamus for patients with refractory temporal lobe epilepsy. A stereotactic implantation of the electrodes is necessary in order to create a reference coordinate system. First, a stereotactic frame is fixed to the skull with bolds. Then, an MRI scan is taken in order to determine the path for implantation with the lowest risk. The frame possesses markers that are visible under MRI. This allows optimal knowledge about the position of the frame. Next, one can calculate where to arrive with the electrodes relative to the frame. Once the coordinates are determined, the surgery can be executed. After implantation of the electrodes, the pulse generator ("stimulator") is implanted under the clavicle and connected to the electrodes by an insulated wire (**Figure 27**). The pulse generator encompasses a battery that delivers power to the electrodes. This makes it possible for each electrode to convey electrical pulses into the brain.

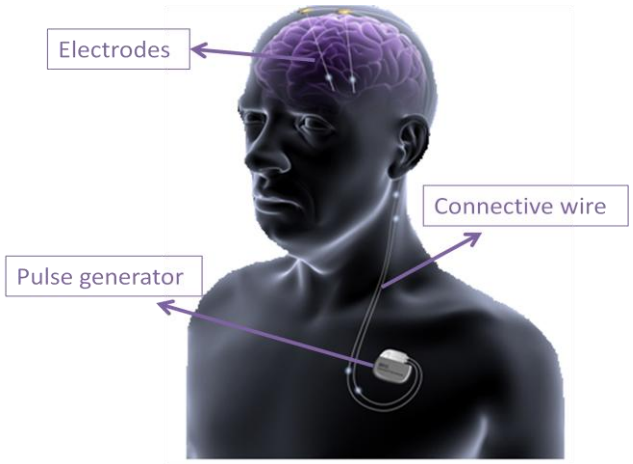

Figure 27: DBS hardware consists of the electrodes, a pulse generator and a connective wire between both.

The electrode material chosen in this study is Platinum Iridium (PtIr). The electrode is MR-compatible, which means that it is MR safe (no additional risk to the patient) and alters the quality of the diagnostic information as well as the operation of the electrode itself in the least possible way [183]. The MR environment in this case can be anywhere inside the 5-Gauss line of the 7 Tesla static magnetic field. Jupp et al.[184] described the development and testing of different MR-compatible electrodes (carbon, gold and platinum iridium) for induction of amygdala kindling in the rat. It was seen that gold and carbon fiber electrodes did not induce any artefacts in T2-weighted images, while the PtIr-electrode induced a larger apparent electrode size (a diameter of 0.5mm became 2.2mm on the MR-images) and signal increase. This disruption of the B_0-homogeneity is due to PtIr being a paramagnetic material. Such materials create artefacts by inducing a magnetic field in the direction of the externally applied magnetic field, and thereby altering the precession frequency of protons. The advantage of PtIr, however, is its good workability. Because a quadri-polar electrode requires twisting of four wires, the material has to be both strong and flexible. Therefore, quadri-polar electrodes out of carbon cannot be made. Also gold is a relative fragile material. Chao et al.[90] have used tungsten electrodes during a DBS-fMRI experiment in the VP thalamus. They concluded that using a thinner tungsten electrode (for example 114µm instead of 250µm) can ensure that there is no image distortion. With regard to biocompatibility, both PtIr and tungsten perform relatively well. They also have good conductivity and both materials are able to visualize BOLD responses in remote brain structures that are functionally connected to the stimulated structure [185]. But the disadvantage of tungsten is that it is a relative rigid material, which makes twisting of the wires to form a quadri-polar DBS-electrode more difficult. Therefore, platinum iridium turns out to be the preferable material in the current study.

2.3.2 DBS and epilepsy

Up to 33% of the patients suffer from "refractory epilepsy", which means that those patients cannot be controlled with Anti Epileptic Drugs (AED's). More in specific, they have tried at least two AED's without any marked improvement. Thirty to 40 percent of the patients with refractory epilepsy are candidates for a resective surgery, the other 60 to 70 percent may benefit from VNS. Only one percent is treated with DBS today [130]. The most common DBS stimulating targets in epilepsy include the anterior and centromedian nucleus of the thalamus, as well as the hippocampus.

2.3.2.1 Targeting the hippocampus

The hippocampus is a key component in the network abnormality of temporal lobe epilepsy (TLE), the most common form of refractory epilepsy [131]. The hippocampal formation is part of the Circuit of Papez. The circuit originates from the hippocampus and subiculum, projects via the fornix to the mammillary body, then via the ascending mammilothalamic tract to the anterior nucleus of the thalamus (ANT) (**Figure 28**). The ANT projects to the cingulate gyrus, then to the parahippocampal gyrus, followed by the entorhinal cortex, which finally projects via the perforant pathway back to the hippocampus [132,192]. Also the septal nuclei (not shown here) have extensive reciprocal connections with the HC (via the fornix), (hypo)thalamus, amygdala and cingulate cortex. Several locations along the Papez pathway have demonstrated effective modulation of seizure propagation by HFS. Canals et al.[134] stimulated the dentale gyrus (DG) and the hippocampus proper orthodromically by positioning an electrode in the medial perforant path[4]. They concluded that a certain level of activity (and hence, a detectable BOLD signal) can be reached by applying trains of relative low frequency pulses (up to 20 Hz). Once the threshold is passed, there is a linear relation

4 Perforant path: provides a connectional route from the entorhinal cortex to all fields of the hippocampal formation, including the dentate gyrus, all CA fields (CA1-CA3), and the subiculum.

between the BOLD signal and the stimulating current. The authors also established that at current intensities evoking a half-maximum population spike, the activity spreads through the DG, to the hippocampus proper, Sub and EC, first ipsilaterally and then contralaterally. At higher frequencies (50 Hz), subthreshold current intensities spread the activity through the hippocampal formation, restricted to the ipsilateral hemisphere.

An open pilot study with ten patients was performed by Boon et al.[127] about the influence of unilateral DBS on patients with refractory TLE. Half of them experienced a seizure reduction of more than 50% and one patient became completely seizure-free (>1year). Vonck et al.[211] conducted a long-term follow-up (8.5 years) of patients with refractory MTL epilepsy treated with hDBS. They proposed biltateral MTL DBS for patients with a unilateral focus and in whom unilateral DBS failed to decrease seizures by ≥90% after a 2.5-3 year follow-up. Also Cukiert et al.[128] has recently proposed hippocampal DBS as safe and effective in patients with refractory epilepsy. Seven of the nine patients were considered responders. Earlier studies had already shown that DBS in TLE has positive effects on interictal epileptiform discharges and seizures [212-214].

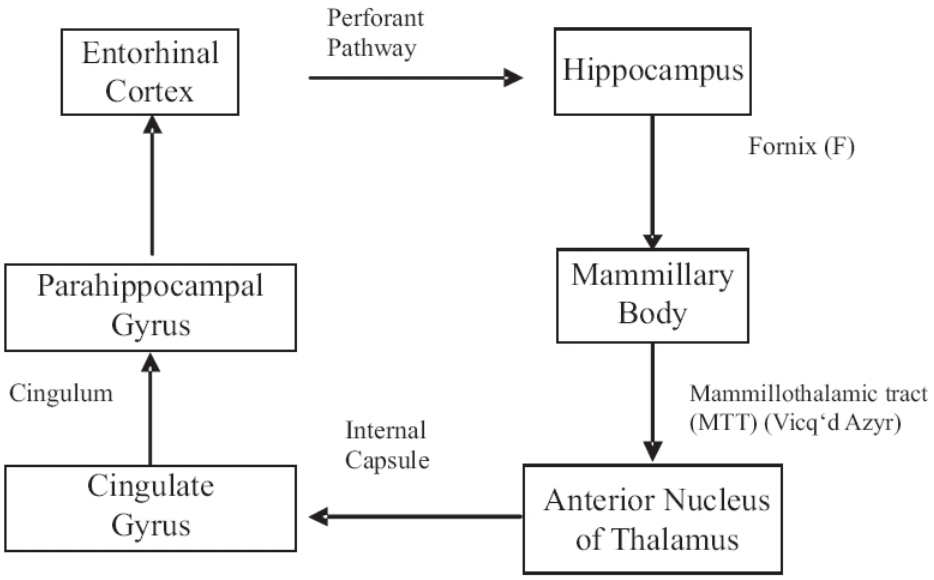

Figure 28: The hippocampal formation is a part of the Circuit of Papez. The circuit originates from the hippocampus and subiculum, projects via the fornix to the mammillary body, then via the mammilothalamic tract to the anterior nucleus of the thalamus (ANT). The ANT projects to the cingulate gyrus, then to the parahippocampal gyrus, followed by the entorhinal cortex, which finally projects via the perforant pathway back to the hippocampus [192].

2.3.2.2 Targeting the thalamus

The anterior nucleus of the thalamus (ANT), another possible target in refractory epilepsy treatment, was stimulated in a double-blind, randomized clinical trial with 110 patients, namely the (bilateral) Stimulation of the Anterior Nucleus of the Thalamus for Epilepsy (SANTE) trial [139]. By 2 years, there was a mean reduction of 56% in seizure frequency; 14 patients were seizure-free for at least six months. Some reports in literature support the "lesioning hypothesis" when the electrodes were placed in the anterior nucleus of the thalamus [140,141]. It is hypothesized by the authors that efficacy of DBS is based on the lesion provoked by insertion of the electrode, also called the "postsurgical microthalamotomy effect". The hypothesis may be true for some targets, but can be inapplicable for others [127]. Targeting the centromedian nucleus (CMN) of the thalamus was performed by Valentin et al [142]. They concluded that CMN stimulation is a safe and efficacious

treatment, particularly in patients with refractory generalized epilepsy. Other possible stimulation targets in refractory epilepsy are the subthalamic nucleus [143], cerebellum [144] and caudate nucleus [145].

2.3.2.3 General conclusions

Some general things may be concluded from previous studies with regard to DBS in epilepsy. First, it is seen that the benefits of DBS increase over time; the maximum effect is seen 1-2 years after implantation. Secondly, seizure frequency reduction is approximately 40 % during the first months and 50-69% after several years. Also the seizure intensity might be reduced [146]. Bradley et al.[142] as well as Laxpati et al.[132] have summarized different studies that were conducted in the past with their specific stimulation sites, seizure types and results. Knowledge gained from animal models in the past was reviewed by Wyckhuys et al [133]. It was concluded that optimal DBS parameters strongly depend on the chosen target. Up to day, the best choice for brain target as well as the most effective combination of stimulation variables (Section 2.3.3) for uncontrolled epilepsy remains unknown. Generally spoken, the electrode can be placed in three kind of structures in refractory epilepsy: a structure involved in (a) seizure onset, (b) seizure generalization and/or propagation and (c) seizure modulation [133]. In TLE, the hippocampal formation is a typical area of seizure onset and hence, stimulating this area can prevent seizure occurrence [210]. Stimulation in the thalamus, for example, interrupts ongoing seizures and stimulation of the STN is promising in suppressing seizure generalization.

2.3.3 Stimulation paradigm

Different stimulation variables have a profound impact on the effects of DBS: amplitude, pulse width and frequency of the stimulation, voltage- or current driven stimulation, mono- or multipolar stimulation modes, automatically delivered stimulation or in response to a detected event. The most effective combination of parameters is often determined by trial-and-error. One set of parameters might be optimal at one site, whereas another combination of parameters is more optimal at another site. For example, stimulation of the ANT is more successful with higher frequencies, while the effects of DBS in the cerebellum are greater with low frequencies [133]. Amplitudes should be kept below the threshold for induction of seizures. In hippocampal DBS, stimulation frequency is approximately 130 Hz with a stimulation amplitude of approximately 200 μA. The stimulation protocol is called High Frequency Stimulation (HFS) [135]. A new stimulation protocol was recently introduced by Wyckhuys et al.[136] with lower stimulus amplitude (156 μA). The protocol is called “Poisson Distributed Stimulation” (PDS). Instead of using a single stimulation frequency as in HFS, a Poisson distribution of stimulus intervals was applied with also a mean frequency of 130 Hz. In this way, the same amount of pulses were delivered in both protocols. The authors concluded that asynchronous PDS shows an effective seizure-suppressive effect and that a lower stimulation intensity (amplitude) can be used, resulting in an extended battery-life.

In general, the stimulation will be mostly bilateral, using two single-channel neurostimulators. Van Nieuwenhuyse et al.[137] proposed bilateral DBS for patients with their both hippocampi as seizure onset zones in TLE. Such patients are not suitable for resective surgery. The authors conducted a comparison study between uni- and bilateral hDBS in a rat model. Bilateral stimulation resulted in an increased seizure reduction, an increased responder rate and better seizure control. They emphasized that the translation from rat to human might not be straight-forward, since there are strong connections between both hippocampi of the rat, which are vestigial in humans. Along these connections, seizure activity can easily spread to the contralateral site, which is not necessarily

the case for the therapeutic effect of unilateral hDBS. Therefore multisite stimulation with different frequencies was proposed to disrupt seizure activity most efficiently in strongly interconnected epileptic networks.

One can also distinguish between mono- and bipolar stimulation. Monopolar is characterized by a radial current propagation around the electrode ending, which is also more widespread. Specific targeting of a certain area can be realized by bipolar stimulation. Monopolar stimulation is most clinically used because it requires lower stimulation intensity for the same clinical output as bipolar stimulation [138].

Next to uni- or bilaterally stimulation, and uni- or bipolar stimulation modes, one can also distinguish between mono- or biphasic pulses. Harnack et al.[215] claimed that during monophasic stimulation, the build-up of charges can lead to tissue damage. Piallat et al.[216] proved that HFS using monophasic pulses was only safe during short stimulation and at low intensities. For pulses as high as 2 mA and durations up to 120 minutes, biphasic pulses are suggested during HFS. The parameters of DBS for control of tremor and Parkinsonian motor symptoms have been assessed in the past mainly by trial-and-error (monopolar cathodic; 1 to 5 V stimulus amplitude; 60 to 200 μseconds stimulus pulse duration; 120 to 180 Hz stimulus frequency) [217]. The parameters for new therapeutic disorders, however, are less easy to predict and knowledge about the therapeutic mechanism(s) of actions of DBS turns out to be of great importance (see next section).

2.3.4 Mechanism(s) of action

DBS turns out to be effective in epilepsy, despite the fact that the working mechanism is largely unknown. The first nagging question is whether the electrical stimulation is excitatory or inhibitory. Secondly, it is questioned which "electroresponsive" structures are affected in the stimulated medium (neuronal cell bodies, dendrites, axons, astrocytes?) (**Figure 29**). In the next paragraphs, some answers are proposed. Presently, four general hypotheses exist to explain the therapeutic mechanism(s) of DBS: (a) depolarization blockade [205], (b) synaptic inhibition [206], (c) homeostatic downscaling of intrinsic excitability [207] and (d) glial-neuronal interactions leading to a wide range of activation and inhibition effects in the whole brain network [208]. They are shortly reviewed below.

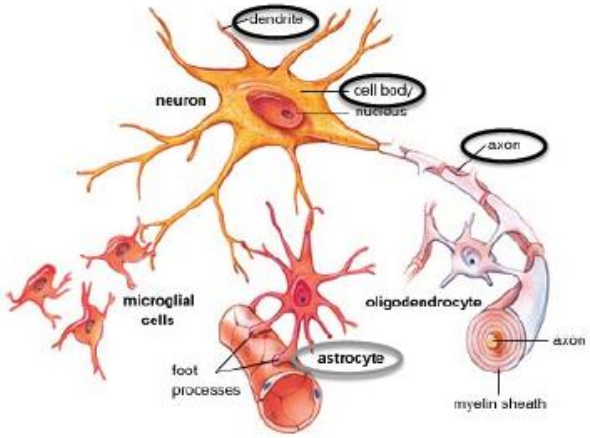

Figure 29: "Electroresponsive" structures that might be affected during DBS: dendrites, cell bodies, axons and astrocytes.

(a) High frequency stimulation results in a strong depression of voltage-gated currents, thereby blocking the neural output near the electrode. In this way, the somatic activity is suppressed.

However, a high-frequency output during DBS of projection neurons is seen and hence, the independent activation of the efferent axon of the projection neurons is not taken into account by this hypothesis [217].

(b) The afferent axons have the lowest threshold for activation. Exciting these axon terminals (afferent inputs) that make a synaptic connection with neurons near the electrode, results in an indirect inhibition of neuronal output by inhibitory interneurons that reduce the bursting activity of the cell. This hypothesis also does not take into account the activation of the efferent axon of the projection neurons [217].

(c) In response to the level of synaptic input activity, neurons adjust the magnitudes of their functional intrinsic currents and/or modulate their synaptic strength. During HFS and PDS, there is a high input activity, resulting in a "scaling down" of synaptic strength. This process of synaptic plasticity is accomplished by neurons triggering a signaling pathway that will restore the homeostatic equilibrium [218]. The hippocampus is a highly plastic brain structure.

(d) DBS can both inhibit neurons and activate axons, generating a wide range of effects. This implies that the mechanisms that underlie DBS work not only locally but also at the network level [36]. Astrocytes will play a major role in this hypothesis (see below).

Several neuromodeling experiments were reviewed by McIntyre et al [147]. The experiments predicted in the first place that the activity recorded in the cell body is not necessarily representative of the spiking output generated in the axon. Secondly, the efferent (axonal) output of local cells to DBS is dependent on the positioning and orientation of the neuron with respect to the electrode. The local cells within ~2 mm of the electrode will mainly contribute to the efferent (axonal) output. Next to location and orientation of the affected structures relative to the electrode, also the voltage response to current injection determines whether the threshold voltage for generation of an action potential is reached [148]. Dependent on the combination of pulse duration and current amplitude, certain peripheral nerves will be activated while others won't (**Figure 30**). High speed nerves (higher axon thickness or less myelinated) need only a short pulse with a low amplitude, compared to low speed nerves. Cells stimulated at subthreshold levels will be suppressed [147]. Local afferents and fibers of passage can also be activated orthodromically or antidromically. Laxpati et al.[132] speaks about an "entrainment" of downstream neuronal firing by DBS, depending on the connections with the downstream circuits.

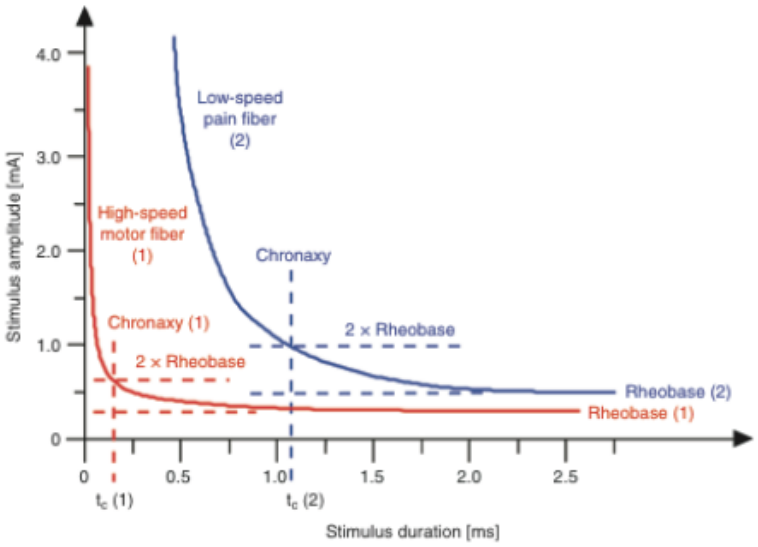

Figure 30: Relationship between current and pulse duration that initiates an action potential in peripheral nerves.

Because the afferent axon has the lowest threshold for generation of an action potential, this is probably the first segment that is activated. The activation threshold increases in myelinated axons, dendrytes and cell bodies, respectively [149]. Recently, also the role of astrocytes -a major type of glia- in DBS efficacy has been investigated [150]. Astrocytes play an important role in synaptic transmission, whereby a single astrocyte can support and modulate about 100.000 synapses in rodents. Because modulation of axonal flow (and hence, synaptic transmission) is of great importance in the working mechanism of DBS, it is quite likely that both neurons and astrocytes contribute to the therapeutic effect of DBS. Large pools of glutamate are stored in astrocytes. These excitatory neurotransmitters can be extracellular released by HFS through a Ca^{2+}-dependant mechanism. They will play a role in the modulation of neuronal responses important to the cessation of abnormal oscillatory activity as seen in seizures [151]. Hence, the effect of DBS seems to be excitatory in nature, rather than a local inhibition at the site of stimulation. Activated astrocytes can signal further astrocytes through long-distance Ca^{2+}-waves across large networks, contributing to the observed network effects induced by DBS. In this way, astrocytes may contribute to the distal (ipsilaterally) effects of inhibition (of excitatory cells) induced by DBS [152].

2.4 DBS and functional imaging

2.4.1 DBS-fMRI

Previous studies [134, 153-155] have investigated BOLD responses during direct stimulation of the perforant pathway of the rat hippocampus. A bilateral BOLD response was detected in hippocampal, thalamic and cortical structures, depending on the stimulation intensity. It was also seen that the DBS-induced bilateral connectivity increased with increasing stimulation intensity. The difference with the current study is that previous researchers have used acute stimulation, compared to a chronically implanted DBS-electrode in this study, meaning that their experimental protocol cannot be used for longitudinal studies. The authors dedicated the increased interhemispheric communication and recruitment of hippocampal and thalamic structures with increasing stimulation intensity to “long-term potentiation”. This means that neuronal strength within the hippocampus can increase due to repeated high-frequency stimulation at that site.

Other studies have also used a chronically implanted DBS-electrode, but did not stimulate the hippocampus. Shih et al.[156] demonstrated thalamacortical connectivity by stimulation of the ventral posteromedial (VPM) thalamus in rats. The fMRI-reponse was highly frequency-dependent. Shyu et al.[157] have shown that fMRI is feasible in investigations of the functional thalamocortical activation during direct stimulation of the rat medial thalamus (MT). They used a chronically implanted glass-coated carbon fiber electrode and a stimulus frequency of 10 Hz. Another study [158] compared direct stimulation of the VP of the lateral thalamic pathway and the MT of the medial thalamic pathway. The former activated the S1, while the latter activated the Cingulate Cortex (which was also found in the study of Shyu et al.). Moreover, they observed that the BOLD response gradually increased with increasing stimulation frequency (up to 12 Hz) and intensity. Finally, Dunn et al.[159] have used carbon fiber-based electrodes that are biocompatible and chronically implanted for studying functional activation at stronger magnetic fields (9.4T).

2.4.2 DBS-PET

Recently, PET has gained ground in the domain of deep brain stimulation (DBS), whereby DBS-induced changes in glucose metabolism can be investigated nearby the electrode as well as in more distant brain regions [160]. The past twenty years, there have been several DBS related PET studies conducted in PD patients [161-166]. However, the outcomes have not always been identical, probably due to methodological differences. Borghammer et al.[167] demonstrated that artefactual CBF-augmentations as seen in several studies most likely arise from normalization to a biased global mean. It was concluded that global mean normalization should not be used as the *default* normalisation reference region in group comparison studies, unless the stability of the global mean could be carefully validated. Comparing different studies in the investigation of the effect of DBS-induced neural changes in the cerebral glucose metabolism, is even more challenging because of the diverse experimental set-ups that have been used: awake or anesthetised rat, stimulation parameters, targeted area, diseased brain, electrode material,...

Van Den Berge et al.[160] investigated the influence of hippocampal DBS on the glucose utilization in a healthy rat brain by micro-PET. They found significant decreases in the glucose metabolism in the bilateral hippocampus and other mesial and cortical limbic structures up- and downstream. Hence, it is shown that DBS affects specific circuits, rather than only locally around the electrode tip. Another [^{18}F]FDG-PET study was conducted by Klein et al.[168], whereby the subthalamic nucleus of a healthy rat brain was stimulated by DBS. They also concluded that unilateral DBS stimulation affects entire bilateral functional networks rather than isolated regions.

2.4.3 DBS-SPECT

Single Photon Emission Computed Tomography (SPECT) is a non-invasive imaging technique to for evaluation of regional cerebral blood flow (rCBF) changes, reflecting changes in neuronal activity. Wyckhuys et al.[169] have used micro-SPECT (with injection tracer HMPAO-Tc99(m)) to evaluate rCBF changes by hippocampal DBS in a healthy rat brain. Substraction analysis of stimulation on/off revealed that hDBS caused a significant decrease both in the ipsilateral and contralateral hippocampus. Moreover, significant hypoperfusion ipsi- and contralaterally was seen by a bipolar PDS stimulation paradigm ($p<0.01$) and the contralateral spread increased with increasing stimulation amplitude. However, the intensity of the hypoperfused regions remained unaltered for the different stimulation amplitudes. These results coincide with the DBS-PET study of Van Den Berge et al., because those authors also did not find any correlation between the intensity of the hypometabolic region and the stimulus intensity. However, the ipsi- and contralateral widespread was also observed with increasing stimulus intensity. Other studies can confirm this relationship between stimulus intensity and spatial extent of the DBS-induced changes [134,147].

2.4.4 DBS-EEG

DBS can possibly stimulate above the seizure threshold of the animal. This means that the animal can suffer from an epileptic seizure, which has to be avoided. During simultaneous DBS-fMRI or DBS-PET experiments, it is necessary to control for DBS-induced seizure activity. This can be accomplished by using an EEG that acts in this regard as some kind of supportive technique, evaluating abnormalities during DBS. EEG characterizes ictal discharges by spiking activity with high amplitude and frequency.

2.4.5 Complications/side-effects

Boon et al.[127] stimulated the perforant pathway (medial temporal lobe region) using relatively low output currents with high frequency (130–200 Hz) and medium pulse widths of 0.45 ms. There was no increase in seizure frequency nor were there any afterdischarges encountered. Even no behavioural responses were noticed. However, there was one occurrence of intracranial bleeding in the area around the depth electrode. In the SANTE trial, adverse effects involved stimulation-related paraesthesias and bleeding around the electrode. Eight patients reported symptoms associated with depression. Another consistent adverse effect of electrode implantation can be tissue inflammation. However, this can be minimized by the use of chronically implanted electrodes, as stated by Van Den Berge et al. [160]. DBS in epileptic patients could also provoke acute symptomatic seizures. Finally, it is also important to remark that the battery of the pulse generator has a limited life-span (5-10 years) and symptoms may return when batteries are not replaced.

A difficulty in DBS neuroimaging could be the magnetic susceptibility artefact as produced by the implanted electrode. Functional response detection might be obstructed in tissue areas near the electrode. Especially in small animals, such artefacts have to be excluded. The right choice of electrode material will play a major role [152]. Another obstacle in functional imaging involves the determination of the influence of DBS in anesthetized rodents. Anesthetization is important to suppress movement during scanning. However, depending on the choice of anesthetic, the BOLD signal can be altered to a greater or lesser extent. Lai et al.[170] implanted a tungsten microwire electrode in the ventral posteromedial (VPM) thalamus for DBS-fMRI scanning procedures in the rat. They compared the influence of alpha-chloralose and isoflurane on the BOLD response. The percent BOLD response as a function of frequency showed a similar profile under both anesthetics, however the peak percent BOLD response was significantly enhanced under alpha-chloralose. The authors concluded in this study that both anesthetics are suitable for VPM-DBS. Alpha-chloralose is preferable in acute studies requiring high signal detectability. Other studies have also successfully used isoflurane as anesthetic in DBS-fMRI studies [123,125]. Chao et al.[90] chronically implanted an MR-compatible electrode in the ventroposterior (VP) thalamus of the rat. They looked to the forebrain BOLD responses over one week under isoflurane and dexmedetomidine. Frequency- and amplitude-dependant BOLD responses were seen in the ipsilateral somatosensory cortex (S1). In this study, a frequency of 12 Hz (or a stimulation current of 300 μA) enhances the response, but only during the first stimulation epoch. The fact that this was not the case in further epochs was explained by the “adaptation effect” [124,132]. Under isoflurane, on the other hand, the BOLD response pattern was extremely unstable between experimental sessions. This could be explained by the fact that a free breathing state instead of mechanical ventilation was applied to control the physiological condition of the animal during stimulation. It is well known that neurovascular coupling is highly sensitive to isoflurane. Also other studies have chosen medetomidine as the preferable anesthetic in DBS-fMRI studies [126, 137].

2.5 Data-analysis

2.5.1 Pre-processing

Prior to statistical analysis, the raw functional data are pre-processed in order to correct for subject movement and to improve the signal-to-noise ratio (SNR). The most essential steps of pre-processing are described below.

2.5.1.1 Temporal filtering

Voxel time courses often show low-frequency drifts due to physiological and scanner-related noise. These drifts reduce the power of the statistical data analysis and can be removed by using a high-pass filter during the pre-processing. In practice, the high-pass filter is multiplied with the Fourier transformed time course of each pixel. The high frequencies (containing stimulus-related activity) are passed, while the low frequencies (drifts) are removed. Next, they are inversely Fourier transformed back to the time domain. This process will increase the overall SNR. The effect of high-pass temporal filtering is shown in **Figure 31**. Low-pass filtering can also be applied to remove high frequency noise. However, this is only useful when the predicted model does not contain high frequencies [171]. This study will use a band-pass filter, cutting off low- and high-frequencies outside a certain frequency-range.

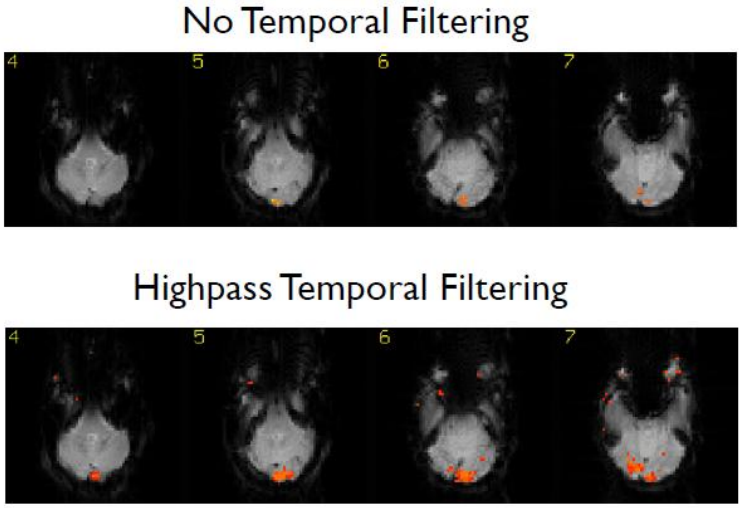

Figure 31: No temporal filtering (above) and high-pass temporal filtering (below) [171].

2.5.1.2 Realigning

Functional images have to be aligned so that the positioning of the brain in each image is the same. The alignment is typically to the first functional image and all subsequent scans are realigned to this one. However, the reference scan can also be the middle or the last scan, as well as the mean of several images. The goal is primarily to remove motion artefacts (such as breathing) in fMRI. Realignment is carried out in three steps. First, six parameters are determined which describe the movement of the head over time. They consist of three rotations (pitch (about x-axis), roll (about y-axis), yaw (about z-axis)) and three translations (x, y, z). This is also called a "rigid-body transformation" of the images (**Figure 32**), because the size of the brain is kept constant [172]. Secondly, the realignment parameters are applied to the functional images. Next, the sum of squared differences (SSD) in intensity between pixels in the image and the reference are calculated and the parameters are adapted until the SSD is minimal.

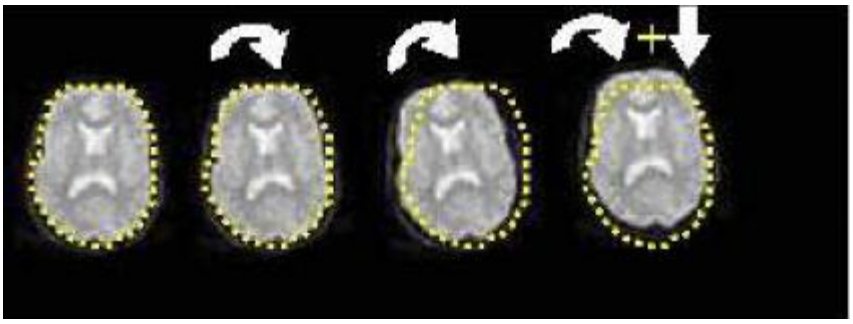

Figure 32: The first image is used as a reference. The rigid-body parameters that are needed for realignment, are calculated for the subsequent images. The second and third image have to be rotated (white, curved arrow), while the fourth image has to be rotated as well as translated (straight, white arrow) [172].

2.5.1.3 Coregistration

Coregistration is used to align the functional and anatomical image. In this way, the activation pattern is superimposed onto the correct anatomical location. There are two methods for coregistration [172]; the first one is "segmentation". The images are segmented into different tissue types (such as CSF, gray matter, white matter) and every voxel is classified by a certain tissue type. A least square method is used to check whether separate segments are a good match. The second method for coregistration is based on "mutual information". This method is used when the anatomical and functional image have a different modality, for example the anatomical scans might be T2-weighted, while the functionals are T1-weighted. In this case, trying to minimize intensity differences between both images, as is done in realignment, would give bad results. This method measures the mutual information (MI) between the intensity of the functional image and the intensity of the anatomical one. For example, when a bright voxel of one image corresponds to a dark voxel in the other image, both images have high MI (**Figure 33**). In this study, coregistration between an anatomical scan (T2) and functional EPI-scan (T2*) is applied based on mutual information.

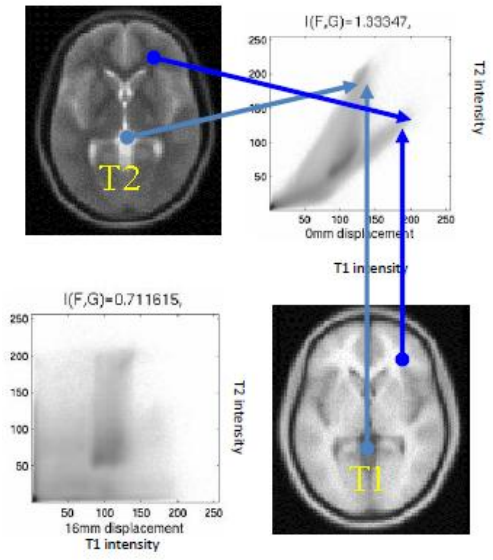

Figure 33: Coregsitration using the mutual information (MI) method. MI is high when a bright voxel in the T2 image corresponds to a dark voxel in the T1 image.

2.5.1.4 In plane smoothing

In plane smoothing is performed to increase the SNR and is realized by the convolution of the image with a Gaussian kernel of a specific size. This size is determined by the full width at half maximum (FWHM), which will be equal to 1 mm in this thesis. This means that the smoothing Gaussian kernel is 1 mm wide at 50 percent of its peak value. The value of 1 mm was chosen because it matches the size of the expected activation area (1 mm^2) in small animals such as rats. During the smoothing-process (also called "spatial filtering"), each voxel intensity is replaced by a weighted average of its neighbouring intensities (**Figure 34**). The voxels that lie within the FWHM-range receive higher weights than those that fall out of it. When the FWHM would be chosen higher than the activation area, then the overall activation would be reduced. Typically, a FWHM of two/three times the voxel size is chosen [172].

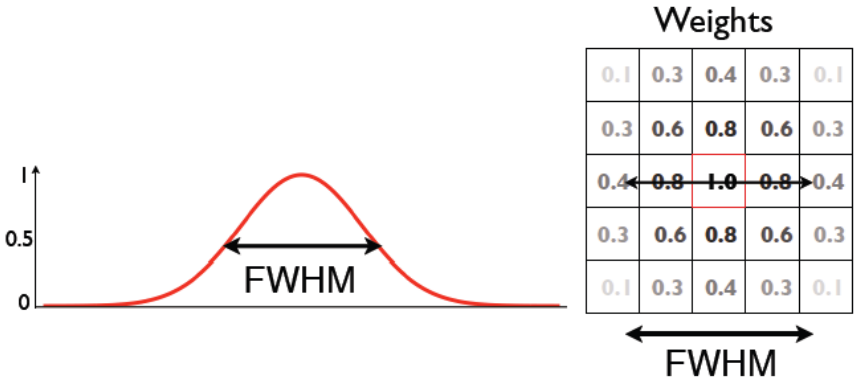

Figure 34: Spatial filtering (smoothing): each voxel intensity is replaced by a weighted average of its neighbouring intensities [171].

An important advantage of smoothing, besides the increase of SNR, is that any reduction in random noise is beneficial for the statistical analysis during which true activations will be detected (see next section). The effect of different smoothing kernels on the amount of significant activations is depicted in **Figure 35**. A disadvantage of smoothing, however, is that the spatial resolution is reduced. The resolution is determined by the number of voxels that fall within the FWHM. Moreover, the convolution of the functional data with a Gaussian kernel poses a problem on the edges of the image, because brain voxels are there smoothened with non-brain voxels.

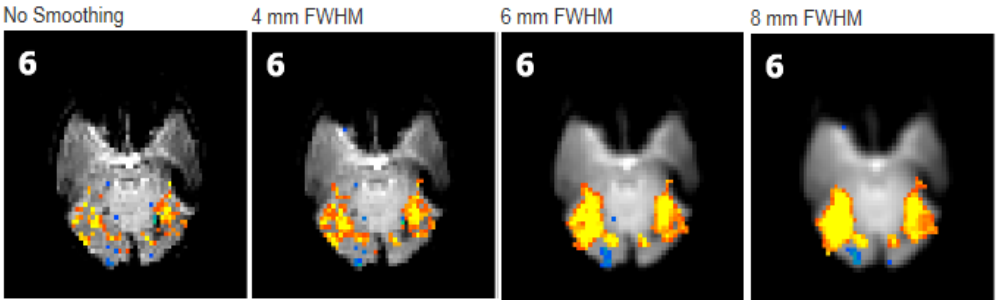

Figure 35: The effect of no smoothing and different smoothing kernels (with FWHM equal to 4, 6 and 8 mm respectively) on the amount of significant activations. Increasing the FWHM shows an increased blurring and activation area [173].

2.5.2 Statistical analysis

The goal of performing an fMRI experiment is to localize the activated brain regions that correspond to a certain motor, sensory or cognitive process. Statistical analysis of the fMRI data will then determine which activation is significant. It will assign weights and an evaluation of statistical

significance (p-value) to the different factors (or effects) that are responsible for the signal fluctuations in time. The latter is also called signal variance. One can distinguish the effects of interest (stimulation) and the effects of no interest (low frequency, high frequency and movement related noise). Due to the presence of noise fluctuations, observed differences between experimental conditions might occur simply by chance [174]. The null-hypothesis states that "an observed effect is solely the result of noise fluctuations". During fMRI analysis, it is determined for the time series of each voxel what the likelihood is that the null hypothesis is true. When $p < 0.05$ (i.e. 5%), then the null hypothesis is rejected, meaning that it is unlikely that the effects have occurred only due to noise fluctuations. Different methods can determine what the p-value is.

2.5.2.1 Mean comparison method: t-Test

A t-Test is performed in every voxel and assesses how much signal variance is explained by a certain effect, relative to the amount of unexplained noise left by the total model [172]. The formula of the t-value is given by:

$$T = \frac{\overline{X_2} - \overline{X_1}}{\hat{\sigma}_{\overline{X_2} - \overline{X_1}}} \tag{5}$$

The numerator contains the calculated mean difference between rest condition and stimulated condition, while the denominator contains the estimate of the expected variability (i.e. standard error of the mean difference) [175]. The higher the t-value, the smaller the variability between the two conditions and the less likely it is that the mean difference between two conditions is solely the result of noise fluctuations. The p-value can now be calculated from using the incomplete beta-function, the number of measured data points N and the obtained t-value:

$$p = I_{\frac{N-2}{N-2+t^2}}\left(\frac{N-2}{2}, \frac{1}{2}\right) \tag{6}$$

If $p < 0.05$, the null hypothesis is rejected and the alternative hypothesis is accepted. One can say that in this case the stimulated condition differs significantly from the rest condition.

2.5.2.2 Correlation analysis

When the repetition time is high (e.g. 2 seconds), the BOLD responses change gradually from one condition to the next. In this case, it can be difficult to calculate the mean of different conditions (as is done in a t-Test), because different time points cannot be assigned easily to different conditions [175]. Correlation analysis has the possibility to capture the gradual increase and decrease of the BOLD signal. The time course of a certain reference function (X_t) will be compared with the time course of the measured data (Y_t) at each voxel. This comparison is realized by calculation of a correlation coefficient r:

$$r = \frac{\sum_{t=1}^{N}(X_t - \bar{X})(Y_t - \bar{Y})}{\sqrt{\sum_{t=1}^{N}(X_t - \bar{X})^2 \sum_{t=1}^{N}(Y_t - \bar{Y})^2}} \tag{7}$$

r indicates the strength of covariation and has a value between -1 and +1. A value of +1 indicates a perfect correlation, meaning that the reference and the data time course go up and down in the exactly same way. A value of -1 indicates perfect anti-correlation and a value close zero means no correlation. In this case, the null hypothesis corresponds to r=0, meaning that a value in one time course cannot be used to predict the corresponding value in the other time course and hence, the occurred effects are only due to noise fluctuations. Whether the null hypothesis is rejected or accepted, is again determined by the p-value. This value is calculated by formula (6), whereby t is in this case:

$$t = \frac{r\sqrt{N-2}}{\sqrt{1-r^2}} \quad (8)$$

Seed-based correlation analysis is one of the most common ways to investigate functional connectivity within the brain. The seed can be an individual voxel or a certain region of interest (ROI). When the time series of the seed is highly correlated with the time series of other voxels or regions in the brain, they are said to be functionally connected. This can be understood by the fact that brain areas with similar activation patterns are most likely to be communicating and forming a network.

2.5.2.3 General Linear Model (GLM)

The GLM models the observed data (dependant variable) as a linear combination of predictor/regressor variables (independent variables). The dependent variable corresponds to the observed fMRI time course of a voxel, while the independent variables correspond to several reference functions, i.e. the time courses of *expected* fMRI responses for different conditions. Such a predictor time course is obtained by convolution of a "boxcar" stimulus function with the HRF (**Figure 36**). Each predictor time course is then weighted by a coefficient ß, which quantifies the contribution of the predictor time course to the observed time course. A large positive (or negative) ß weight corresponds to a strong activation (or deactivation) in the voxel during the modelled experimental condition relative to the baseline [175].

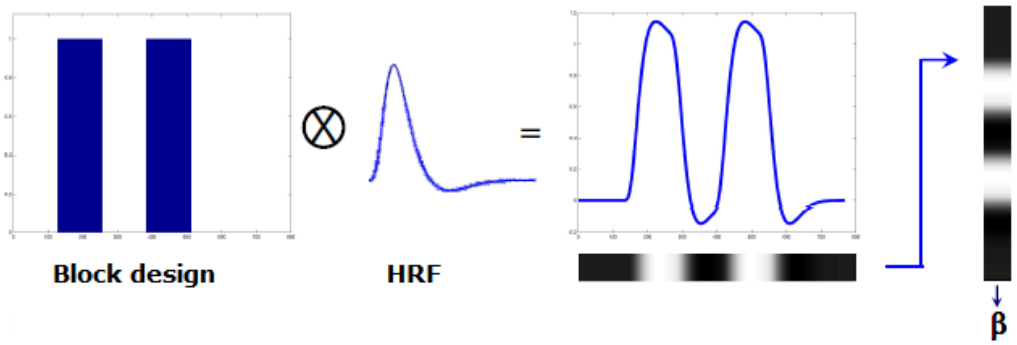

Figure 36: A predictor time course is obtained by convolution of a "boxcar" stimulus function with the HRF. Each predictor time course is then weighted by a coefficient ß, which quantifies the contribution of the predictor time course to the observed time course.

The GLM system is represented in **Figure 37**. An error ε is added to the system of equations to describe the remaining unexplained observed data due to noise fluctuations. The formula for i observations modelled using j predictor variables is given by (Figure 37):

$$y_i = ß_0 + ß_1 x_{i1} + ß_2 x_{i2} + ß_3 x_{i3} + \ldots + ß_j x_{ij} + \varepsilon_i \quad (9)$$

$$\Updownarrow$$

$$Y = ßX + E \quad (10)$$

whereby X represents the matrix of predictor variables (also called the design matrix or the model), Y represents the vector of the observed data, ß represents the vector of weighting factors and E represents the vector of error values. $ß_0$ represents the signal level of the baseline condition. The design matrix X (**Figure 38**) consists of eight columns which equal the amount of regressors. The first regressor depicts a block-design with rest periods in between. The six regressors next to it are the realignment parameters of the subject (3 position- and 3 rotationparameters with respect to the first scan entered). The last column consists of the constants (baseline). Because the convolved regressor (i.e. the first regressor) will not always be a good fit to the actual course of the BOLD signal, temporal derivatives (subtle time-shift of the signal) or dispersion derivatives (change width of the

HRF response) can be added as regressors in the design matrix X. They are inserted as the second and third regressor in X.

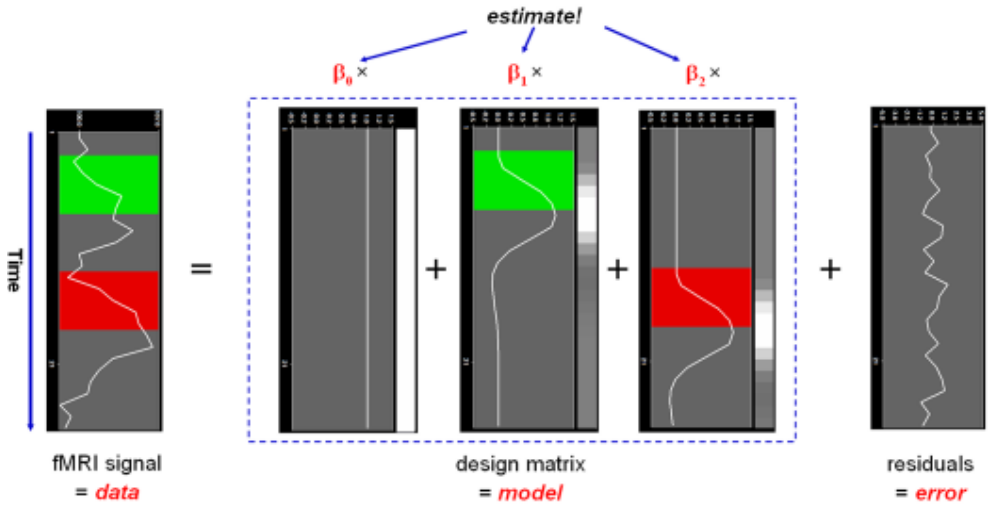

Figure 37: Representation of the GLM system.

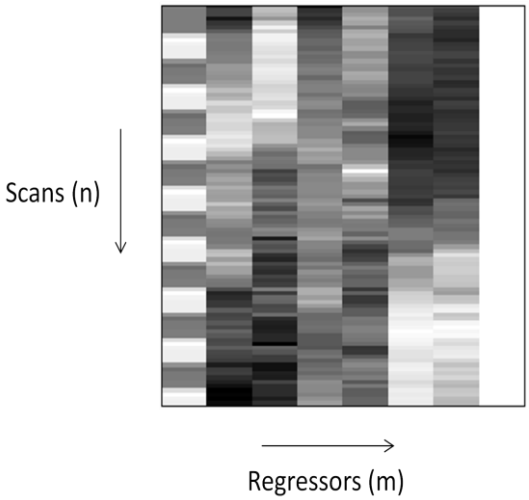

Figure 38: Design matrix X, with n Scan rows and m Regressor columns. Black corresponds to the regressor at its smallest value, white corresponds to the regressor at its largest value and grey represents intermediate values [176].

It is the aim to solve for the unknowns $ß_{0..j}$. This will be realized by estimating the ß-values and solving the equations for $y_{1..i}$ in order to acquire y-values that are as close as possible to the observed values. Therefore, one has to determine the ß-values such that the error values are minimal. GLM finds such ß-values by minimizing the sum of squared error values:

$$e'e = (Y - Xß)'(Y - Xß) \rightarrow \min \quad (11)$$

whereby e'e is the vector notation for the sum of squared error values, and ' denotes transposition of a vector or matrix. The optimal ß weights are now obtained by:

$$ß = (X'X)^{-1}X'Y \quad (12)$$

After the parameters are estimated, one can test several null hypotheses using t or F statistics. To assess which individual conditions differ significantly from each other (with regard to activation), contrasts are used. A contrast is a linear combination of ß values that correspond to a certain null hypothesis, which can be described by:

$$\text{contrast} = c'ß \quad (13)$$

In the case of "T-contrasts", c is a vector. The contrast vector c defines how to weight each column of the design matrix. For example, when you want to test whether activation in condition 1 is significantly different from activation in condition 2, the null hypothesis would state that the ß values of both conditions would not differ, i.e. $ß_1 = ß_2$ or $(+1)ß_1+(-1)\ ß_2=0$. The contrast vector is in this case [+1 -1]. Conditions can also be compared to a baseline, hence when you want to find areas that are active during condition 1, but not during the other condition, you use the contrast vector [1 0]. When c is a matrix, "F-contrast" is defined, meaning that *any* difference (positive or negative) between conditions can be detected. The F-test evaluates whether any (combination of) contrast(s) explains a significant amount of variability in the measured data [176]. For example, when c is [1 0 0 0; 0 1 0 0], it is tested whether including conditions 1 and 2 together explains significant variance in the data [177].

A typical fMRI data set of a rat brain contains approximately 30.000 voxels. The same design matrix X and contrast vector c will be used for each voxel, but each voxel will have its "own" vector of ß values. Statistical test-results for each voxel are accumulated in a 3D data set, called a statistical parametrical map [175]. Only those voxels with e.g. a t-value that exceed a specified threshold are colour-visualized. However, specification of a threshold for each voxel creates a "multiple comparisons problem" (MCP), meaning that there would be a lot of false positives when the experiment is repeated several times for a single voxel. Therefore, the Bonferroni correction method can be applied, which involves that the single-voxel threshold is adjusted to retain an error probability of 0.05 *at the global level*. The single-voxel threshold then equals the family-wise error probability (p=0.05) divided by the number of independent tests that have to be performed. The latter equals the number of voxels in the rat brain (approximately 30.000). Because this method controls for false positives across *all* voxels, it is called a "family-wise error correction method". However, the Bonferroni correction method corrects more strictly than is actually necessary, because it assumes that the data at neighbouring voxels are completely independent from each other. In reality, neighbouring voxels show similar activation patterns within functionally defined brain regions [175]. Hence, they are more likely to activate in clusters. A solution for that in SPM is the family-wise error correction method that is based on the so-called "random field theory" (RFT). It estimates the true number of independent tests and corrects the threshold accordingly. A disadvantage of this correction method could be that it requires spatial smoothing, lowering the spatial resolution. A last option to solve for multiple comparisons and to decrease to risk for false positives, is to restrict the number of voxels you want to look at. This can be done by choosing a lower uncorrected p-value (e.g. $p < 0.001$) and grouping the voxels in a cluster with a certain clustersize k. Here a voxel is only deemed truly active when it belongs to a cluster of k contiguous active voxels. Because clusters are more unlikely to occur only by chance (i.e. noise has less of a tendency to form clusters of activated voxels), the solution is thus to threshold clusters, not voxels. This method is called "cluster based thresholding" and is chosen when one is interested in specific areas of the brain. It can be applied in combination with RFT whereby the desired threshold (e.g. p=0.05) is divided by the number of resels (resolution elements) (or independent tests). A resel is a bunch of voxels equal to the same size as the FWHM of the smoothness of the image [178].

2.5.2.4 Independent Component Analysis (ICA)

ICA is a viable alternative for GLM in fMRI statistical data-analysis [179,180]. It is a purely data-driven method (rather than hypothesis-driven) that attempts to find common features within the data. There is no prior knowledge about the HRF required. This can be an advantage in an analysis were multiple subjects have to be compared, as HRF will differ amongst them. Information about the

exact onset and duration of stimulation (as was needed in the design matrix of GLM), is also not required in ICA.

ICA tries to recover the underlying (independent) signals from linear mixtures of those signals. ICA assumes that the source signals are mutually and statistically independent in space (sICA) or time (tICA). sICA is the preferred technique in fMRI data analysis because there are more spatial points (i.e. voxels) than temporal points (i.e. image acquisitions) [181]. The mixed signals can be represented in a data matrix X. This matrix consists of different columns that represent the time course of a single voxel. Each row of the matrix is a spatial image at a certain time point. The aim of ICA is now to factor the data matrix into a product of a set of time courses and a set of spatial patterns (**Figure 39**) [182]. After pre-processing, the ICA decomposition can then be written as X=AS, whereby X represents the data matrix, S represents the source matrix (containing the independent signals) and A represents the mixing matrix (containing the mixing weights).

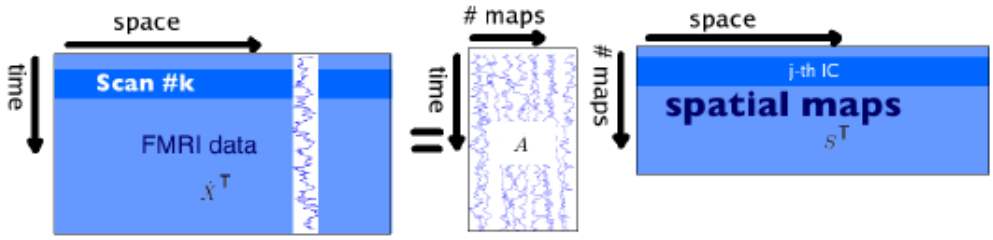

Figure 39: Illustration of the ICA decomposition after pre-processing. The aim of ICA is to factor the data matrix X into a product of a set of time courses A and a set of spatial patterns S [181].

Chapter 3

Materials and methods

3.1 Electrode

Quadri-polar DBS-electrodes were used, which are custom-made by twisting together four PFA-coated Platinum Iridium wires (A-M Systems, WA, U.S.A.), with 140µm diameter (**Figure 40**). The two outer channels are used for stimulation purposes and the distance between their tips is 3mm. The inner wires are used for EEG recording and the distance between their tips is 0.5mm. Each wire has a connector pin for contact with the stimulation unit. Also a ground electrode was made, with a diameter of 125µm, which consists of a polyimide coated stainless steel wire (Bilaney, Germany) and also a connector pin. The ground electrode was implanted subcutaneously in the neck.

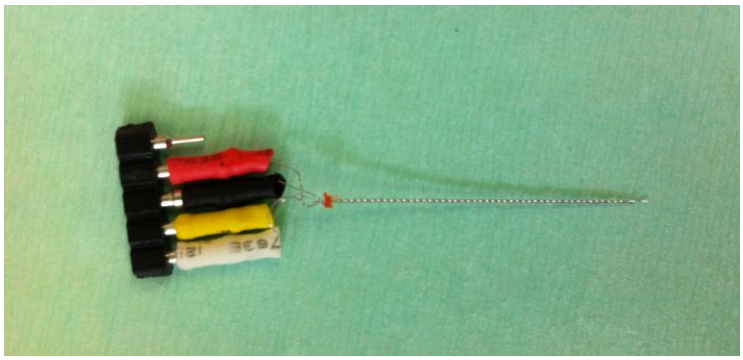

Figure 40: Quadri-polar DBS electrode. The red and white channels are for stimulation purposes, while the black and yellow channels are for EEG recording. The uppermost connector pin is for contact with the ground electrode.

3.1.1 Impedance measurement

Before the electrodes were implanted, their impedance was measured using an impedance meter. Impedance – being the resistance to current flow in an alternating current circuit – opposes electrical current delivery to the tissue. Therefore, it is important to verify when impedance is too high due to for example electrode contact loss. First, all electrodes were electrolytic cleaned for impedance optimization. Since the DS4 stimulator can generate up to 48V, the impedance cannot be over approximately 74 kΩ for a current intensity of 650 µA (i.e. the maximal administered intensity during threshold determination). The impedance did not exceed 70 kΩ.

3.2 Subjects

In this study three adult male Sprague-Dawley rats (Janvier Laboratories, Saint Berthevin, France) were used with a body weight between 200g and 250g. It was planned that all rats underwent three hDBS-fMRI experiments under medetomidine and two under isoflurane. However, two rats died within the first twenty minutes that they were tested with isoflurane. Only one rat was able to sustain the isoflurane protocol – a protocol that was successfully conducted in previous studies [90]. However, that rat was excluded from this study due to bad headcap placement causing distortion in

the fMRI acquisitions. The headcap consists of the connector piece with stainless steel pins and dental cement. During the fabrication of the headcap it is highly important that the connector pins are positioned as far posterior as possible, to avoid metal artefact in the FOV of the EPI acquisitions. **Figure 41a/b** shows localiser scans (tripilots) that were taken for appropriate positioning of the subject in the scanner. The scans show the central axial and sagittal brain slice, whereby the right figure represents one of our rats with a rightly implanted headcap and the left one represents a rat with a one that was implanted too low. One of their EPI scans (**Figure 41c/d)** confirms indeed incorrect implantation of the headcap, causing a lot of distortion in dorsal coronal slices. Therefore, the third rat had to be excluded from the analysis. All rats were treated according to guidelines approved by the European Ethics Committee (European Directive 2010/63/EU). The experimental procedures were approved by the Animal Experimental Ethical Committee of Ghent University Hospital (ECD 14/15). The rats were kept in a temperature-controlled room (20-23°C), using a 12h light/dark cycle. The relative humidity was approximately 50%. Food and water were available *ad libitum*.

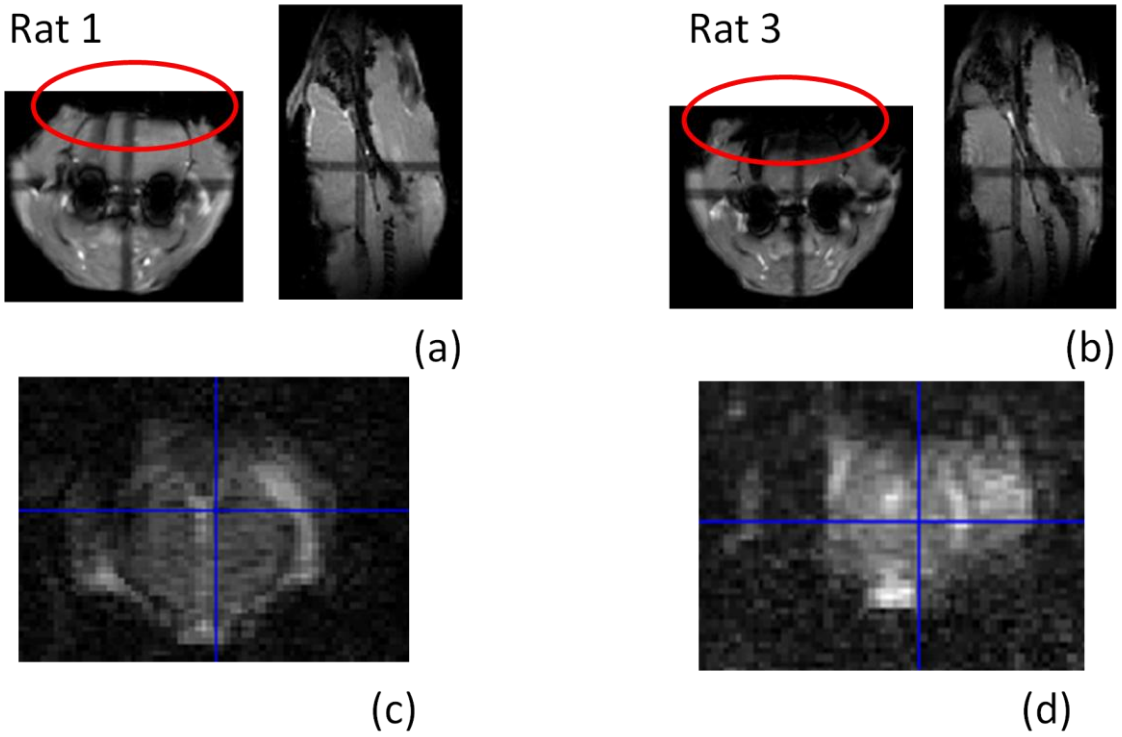

Figure 41: Comparison of one of our rats (figure a and c) with a rightly implanted headcap and one rat (figure b and d) with a headcap that was implanted too low in the head, causing distortion (see red circles) in dorsal brain structures. a/b: localiser scans, c/d: EPI's.

3.3 Surgery

First, the rat is anesthetised by a mixture of medical 0_2 and isoflurane (5% for induction, 2% for maintenance). Next, the rat is fixed in a stereotactic surgical frame by means of two ear bars and one tooth bar (**Figure 42**).

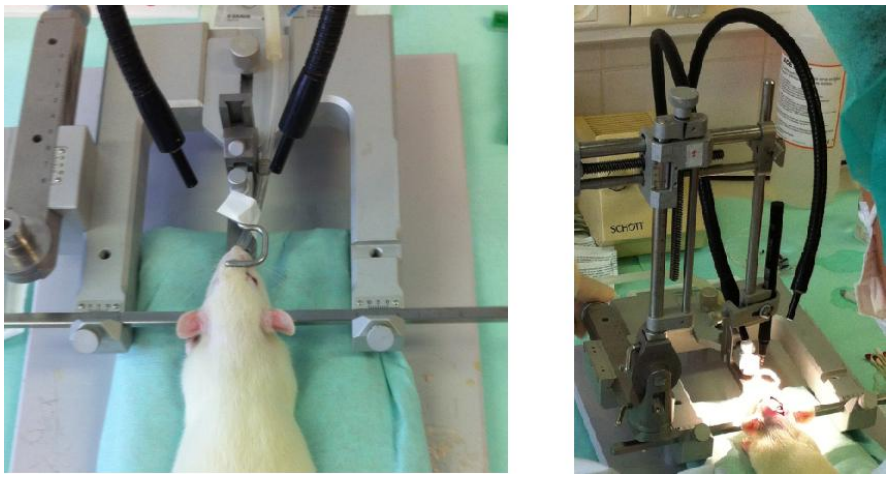

Figure 42: The rat is fixed to a stereotactic surgical frame. The teeth are placed over a tooth bar.

After disinfecting the surgical area, an incision is made with a scalpel and the meninges are pushed aside in order to reveal the bare skull. The intersection of two cranial sutures on the skull is called "bregma" (**Figure 43a**), and is used as the reference for electrode implantation. The anterior-posterior (AP) and medio-lateral (ML) coordinates relative to bregma can be read from the stereotactic frame and the exact position of the ventral right hippocampus can be determined from the neuroanatomical atlas (AP: bregma-0.56 cm, ML: bregma-0.52 cm, DV: bregma-0.74cm) [191]. Next, five holes are drilled into the skull, whereby one is for placing the electrode and the others for placement of four MRI-compatible nylon anchor screws (**Figure 43**).

Figure 43: a) The intersection of two sutures is called "bregma". Five holes are drilled, whereby one hole is for the electrode and the other four holes are for anchor screws. b) The screws are placed in the skull on the positions of the crossmarks of figure a.

The electrode is now placed on the stereotactic arm. It is important to adjust the electrode positioning within the holder to ensure straight and vertical implantation (**Figure 44a**). Immediately after the actual implantation of the electrode into the hippocampus, the electrode is fixed to the nearest screws by using UV cement for thirty seconds (quick dry). Acrylic dental cement is applied to the skull surface in between the screws to better fix the headcap for durability (**Figure 44b**). The ground electrode is inserted subcutaneously along the neck of the rat. It is important that the headcap is placed as posterior as possible, because it contains MR-incompatible parts made from SS that can create MR-artefacts in the brain images. After the electrode placement, the animal is put under IR-light to ensure proper body temperature at the start of recovery. The animals were allowed one week recovering period before conducting the actual DBS-fMRI experiments.

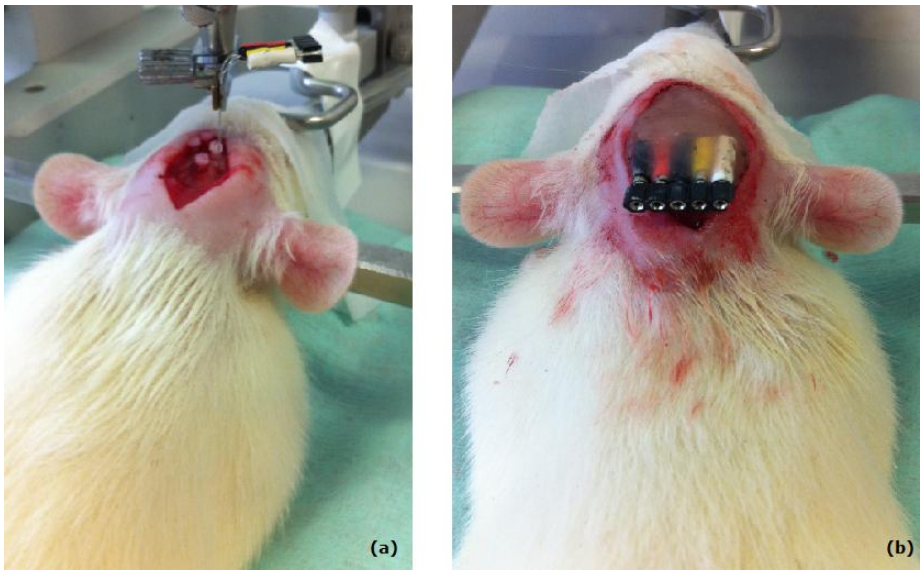

Figure 44: a) The coordinates for placement of the electrode are controlled by the stereotactic frame. b) Acrylic dental cement is applied to the skull surface in between the screws to better fix the headcap.

One day after the post-surgical recovery period (=one week), thresholding was performed in each individual rat to determine the stimulation intensity giving rise to an epileptic seizure. During the actual DBS-fMRI experiments, DBS was performed at different lower percentages of this seizure threshold. The thresholding started after at least one hour of continuous medetomidine infusion. Medetomidine was continued during the experiment itself. The threshold was determined by successive stimulation episodes of 15seconds, alternated by rest episodes of 60seconds. For each successive stimulation episode, the intensity was augmented by 25µA until an ictal discharge was observed on the EEG. Ictal discharges are characterized on the EEG by spiking activity （**Figure 45b**）. EEG recording was possible using the inner wires of the quadri-polar DBS electrode.

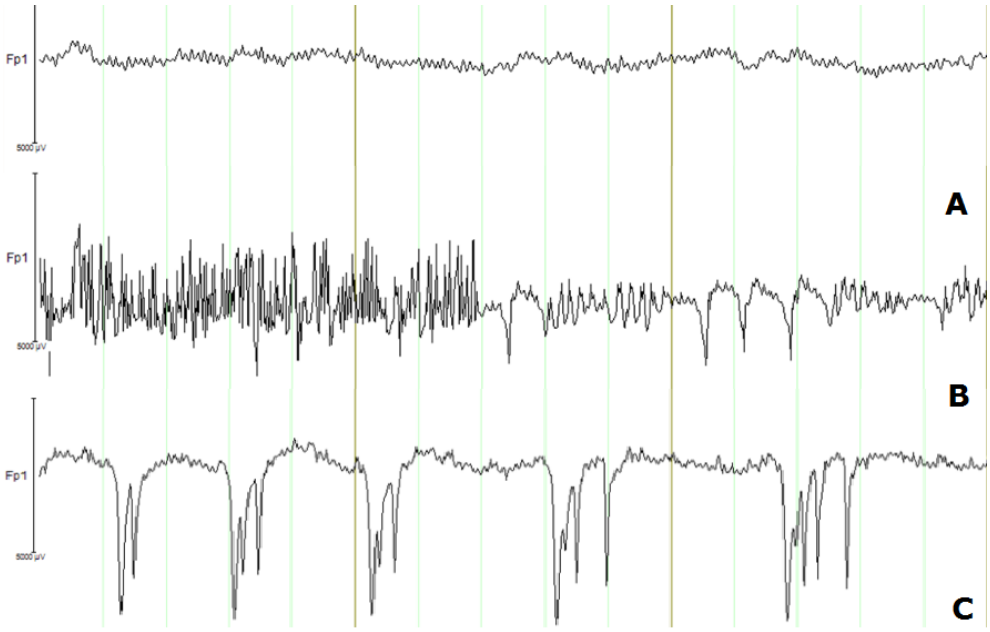

Figure 45: A) Normal EEG, B) ictal EEG during stimulation (first half of the EEG), C) post-ictal EEG.

3.4 Deep Brain Stimulation

All rats were stimulated unilaterally in the right hippocampus with a Poisson distributed stimulation (PDS) paradigm. The paradigm consisted of a series of bipolar, biphasic, charge-balanced square-wave pulses with a pulse duration of 100 μs and an interstimulus duration that varied according to a Poisson distribution with mean and variance 1/130 seconds. An isolated stimulator (DS4 Bi-phasic Stimulus Isolator, Digitimeter Ltd, Hertfordshire, England) delivered constant pulses to the hippocampus through the outer channels of the implanted quadri-polar electrode. The stimulator is triggered by a data-acquisition card (NI-DAQ USB-6343, National Instruments, Austin, TX, U.S.A.), which is on its turn connected to a standard PC. The stimulation consists of 5 blocks of 60 seconds, of which 40 seconds rest and 20 seconds stimulation. This resulted in a total experimental time of 5 minutes. The stimulation protocol for one DBS-fMRI session is schematically presented in **Figure 46**. In total, 10 DBS-fMRI sessions are performed, with 2 sessions per stimulation intensity. The intensities were set at 10%, 30%, 50%, 70% and 90% of the seizure threshold as was determined for each individual rat.

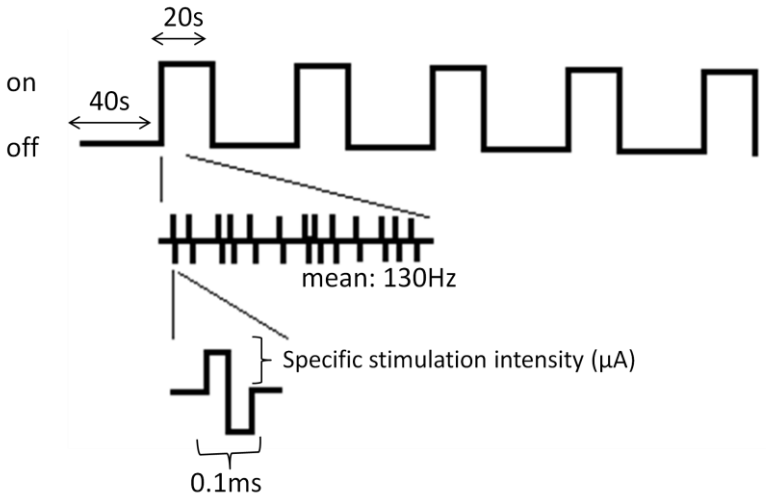

Figure 46: Stimulation protocol for one DBS-fMRI session. Biphasic constant electrical current pulses are used, with a width of 0.1 ms, mean frequency of 130 Hz and intensities set at 10%, 30%, 50%, 70% and 90% of the seizure threshold. This threshold was determined for each individual rat. The stimulation consists of 5 blocks of 60 seconds, of which 40 seconds rest and 20 seconds stimulation.

3.5 BOLD-fMRI acquisition

Animals were anesthetized initially using a mixture of medical 0_2 and isoflurane (5% for induction, 2% for maintenance), delivered through a nosecone for spontaneous breathing.

In the medetomidine experiment, a bolus of medetomidine (± 0.05 mg/kg) was injected subcutaneously. Isoflurane was discontinued 10 minutes after administration of the bolus. A continuous subcutaneous infusion of medetomidine (rate: 0.1 mg/kg/h) was started 15 minutes after the bolus injection [15,16]. Approximately 90 minutes after the start of the continuous infusion, the rate is augmented to 0.3 mg/kg/h, according to the study of Pawela et al [100]. According to the authors, a constant infusion of medetomidine at 0.1 mg/kg/h is not sufficient to maintain sedation beyond 3 hours and stepping the infusion dosage from 0.1 to 0.3 mg/kg/h makes experiments as long as 6 hours possible. At the end of the DBS-fMRI experiment, medetomidine was antagonized by an intraperitoneal injection of atipamezole (0.1 mg/kg).

In the isoflurane experiment, the isoflurane is lowered to 2 % after maximum 10 minutes and continued for the rest of the experiment. Both experimental protocols for scanning are depicted in **Figure 47**.

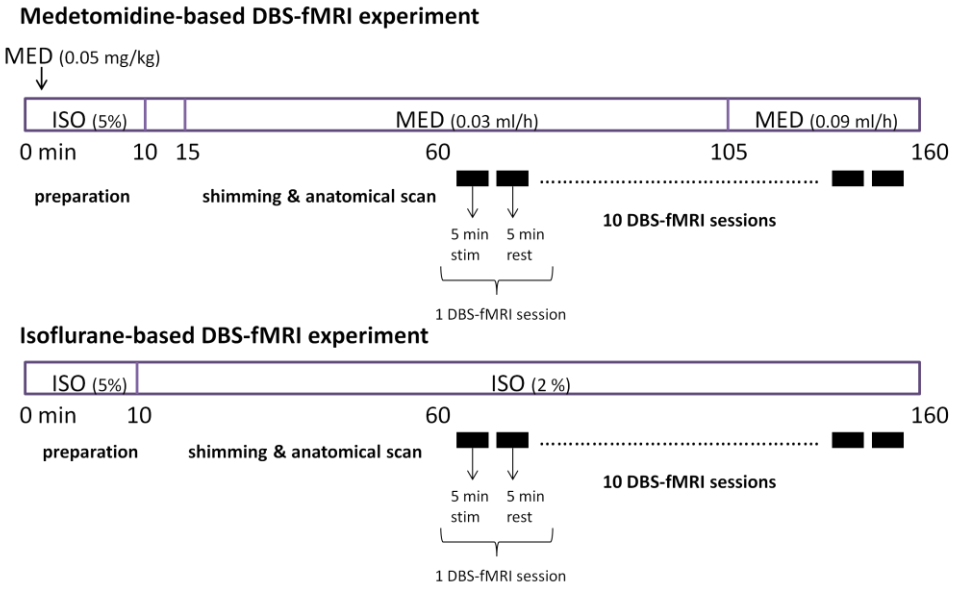

Figure 47: Experimental protocol of a medetomidine-based DBS-fMRI experiment (above) and an isoflurane-based DBS-fMRI experiment (below).

All MR images were acquired on a Pharmascan 7T (Bruker BioSpin, Ettlingen, Germany) with a bore diameter of 160mm. The system is equipped with a BGA-9S gradient coil with an outer diameter of 150mm and an inner diameter of 90mm. The BGA-9S HP gradient coil has a gradient strength of 370 mT/m and a maximum linear slew rate of 3300 T/m/s. A Rat Head/Mouse Body volume coil with an inner diameter of 40mm and an outer diameter of 75mm was used to transmit and receive the RF signals. The length of the coil is 100mm. The rat brain volume coil was used in order to obtain BOLD responses from subcortical brain structures, such as the hippocampus. The rat is restrained in the scanner using a tooth bar, adhesive tape and two flexible cushions on the two sides of the head. Decent rat positioning is crucial to maximize EPI quality and to minimize coregistration errors. The temperature is held constant by using a water-circulated heating pad at ± 37°C.

Before starting the BOLD-fMRI data acquisition, the magnetic field homogeneity of the acquisition site is improved by shimming. Global first- and second order shims were applied on the *global* volume. This is followed by second order *local* shimming on an isotropic voxel of 4x12x6 mm^3. The latter is done using MAPSHIM macro, which performs the shimming protocol based on a field mapping procedure over the volume of interest. More in specific, a field map is acquired and a correction based on the result is computed. Next, the quality of the shim can be determined by measuring the FWHM of a water FID signal, using the Press_waterline sequence. The line width at 50% of the signal-height has to be below 20 Hz for a good shim in a normal rat brain [186]. Because of the electrode artefact and the size of the local shim area in our study, the line width will be higher (up to 70 Hz is still acceptable).

The BOLD-fMRI data acquisition is performed using multi-slice single shot gradient-echo echo planar imaging (GE-EPI). The geometry is adjusted to cover the fourteen coronal slices of interest, with TE=20ms, slice thickness=1.2mm, matrix size=80x80, pixelsize=0.313x0.312mm^2, FOV= 2.5x2.5cm^2. During 5 minutes, 150 EPI's are recorded with a TR of 2 seconds. This GE-EPI run is repeated ten times (two times for each intensity; 5 intensities in total) in randomized order. There is a 5 minute rest-period between each run to allow neurovascular recovery and to minimize

contribution of heating and tissue damage as can be introduced by DBS [15,16]. Anatomical images are acquired using a Turbo RARE sequence with slice thickness=0.6mm, matrix size=276x320, pixelsize=0.109x0.109mm^2, FOV=3x3.5cm^2. These T2-weighted images provide information about anatomical reference and electrode position verification.

3.6 Data-analysis

The statistical analysis of the acquired functional images is done in Matlab (The Mathworks, Inc., version 7.12.0 (R2011b)), using also its statistical parametric mapping package (SPM8). Each rat underwent three DBS-fMRI experiments under medetomidine. One fMRI experiment consisted of 10 fMRI acquisitions (2 sessions per stimulation intensity; 5 intensities in total).

3.6.1 Pre-processing

First, pre-processing is done to match all scans of an individual subject under one of the anesthetics. The pre-processing steps of one DBS-fMRI experiment include: (1) Realigning and reslicing of all EPI scans of a certain session to the mean of that session (and also aligning the mean of each session to the mean of the first session), (2) Coregistration of all images to the anatomical image, and (3) Smoothing of all images. Realignment is done to remove movement artefacts and the default values of SPM were used, except for 'separation' and 'smoothing' because those settings applied to human subjects. 'Separation' involves the choice of the distance between the points sampled in the reference image; it is set to 0.4 mm, which is ten times lower than for a human subject. 'Smoothing' involves the choice of the FWHM of the Gaussian smoothing kernel which is applied to the images before the realignment parameters are estimated. The FWHM is set to 0.5 mm, which is also ten times lower than for a human subject. After realignment, an "rp….txt"-file is created for each session and contains 6 columns (3 position- and 3 rotationparameters in X, Y, Z for each scan with respect to the first scan of the session entered). The second pre-processing step involves coregistration to the reference (i.e. anatomical) image (**Figure 48**), based on normalized mutual information. The mean image is chosen as the source image and is jiggled around to best match the reference image. The other images need to remain in alignment with the source image. Again, the 'separation' values were divided by ten, resulting in [0.4 mm, 0.2 mm]. The third and last pre-processing step involves in plane smoothing of the realigned and coregistered images with a Gaussian kernel of specific width. This is done to suppress noise effects. The FWHM of the Gaussian kernel is chosen to be [1mm, 1mm, 1mm], which is eight times lower than the default values (**Figure 49**).

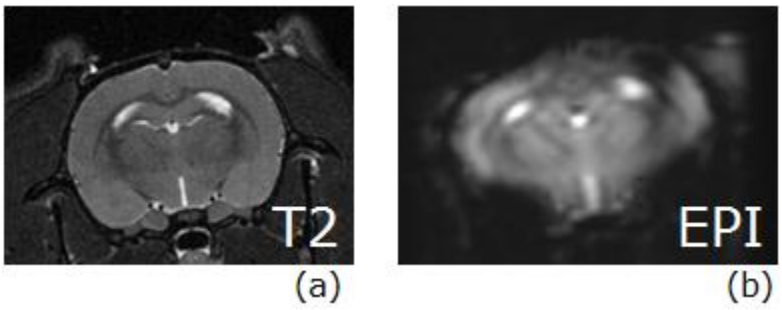

Figure 48: The second pre-processing step involves coregistration of the EPI (b) to the anatomical (T2) reference image (a).

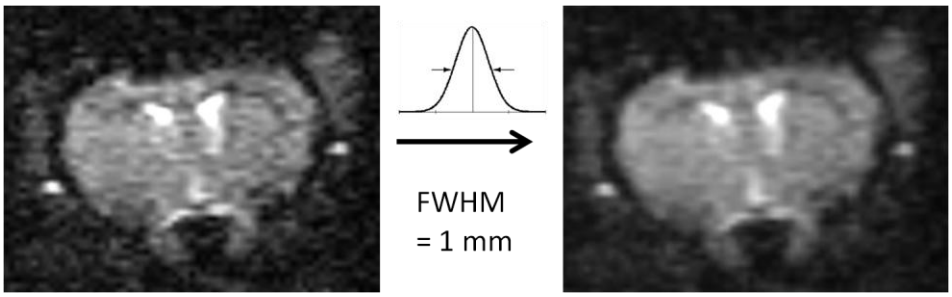

Figure 49: The third pre-processing step involves in plane smoothing of the realigned and coregistred images with a Gaussion kernel with a FWHM of 1 mm.

Eventually, two more options were considered in order to prepare the pre-processed data for statistical analysis. These include: (1) Band-pass filtering and (2) Detrending. Band-pass filtering was performed with the Resting-state fMRI data analysis toolbox (REST), and a bandpassfilter of (0.01 Hz-0.08 Hz) was used to reduce low frequency noise (scanner drifts, slow vascular/metabolic oscillations,...) and physiological noise (cardiac pulsation and respiratory movement). Detrending, on the other hand, was performed by the Linear Model of Global Signal toolbox (LMGS) and removes all effects that are correlated with the global signal (i.e. the time course of the average intensity over all voxels in the brain) [187]. In other words, BOLD fluctuations that are unrelated to neuronally-induced BOLD changes (i.e. both low- and high-frequency components as well as both large- and small-amplitude effects) are removed. The LMGS method achieves this by modelling the time course of each voxel to the global signal and when it correlates with the global signal, the global component is removed from the time course of that voxel. LMGS was chosen over other techniques, because of three reasons. First, it does not assume that global components are of low frequency, in contrast to the method of 'spline detrending'. Secondly, it is not based on any particular experimental design. And thirdly, it allows for regional variation in global effects - which is important in ROI-analysis -, in contrast to the method of 'intensity normalization'. Macey et al.[187] have compared LMGS with spline detrending and intensity normalization. They concluded that LMGS best preserves the magnitude of the signal increase (as opposed to spline detrending) and eliminates subsequent drift likely related to global effects (as opposed to intensity normalization) in fMRI time series.

In total, six methods can be considered of which we have to choose the optimal one. These include: (1) Only pre-processing, (2) Detrending + pre-processing, (3) Filtering + pre-processing, (4) Detrending + filtering + pre-processing, (5) Pre-processing + filtering and (6) Detrending + pre-processing + filtering. Detrending - if applied - was always chosen to be the first step, because a global effect in the fMRI time series is unlikely to be introduced after filtering or pre-processing. Whenever a global effect is present, it will be the biggest in the raw data. Choosing the optimal method comes down to the determination of the "goodness of the fit" of the mean epoched BOLD-signal time series over all the voxels to the block paradigm as was implemented in our model. Other factors that play a role in the determination of the optimal pre-processing method, are the significance of the results (p-value) and the amount of residual noise after cluster thresholding. We conclude that the optimal pre-processing method for our study was pre-processing + filtering, more information can be found in section 4.2 of Chapter Results.

3.6.2 Statistical analysis

To explore DBS-induced network modulation, data were analyzed by means of two techniques: voxel-wise analysis using the General Linear Model (GLM) and seed-ROI based Correlation Analysis (CA). The GLM relies on a known form of the HRF to estimate activation patterns. However, the shape of this response function varies substantially across brain regions and subjects. Therefore,

correlation analysis was introduced as an alternative analysis strategy. The implementation of both methods is described below.

3.6.2.1 General Linear Model

GLM requires information about the exact onset and duration of the stimulation in order to produce Statistical Parametric Maps (SPMs). This information is added in the step 'specify 1st level' (or fMRI model specification), which is used to implement a within-subject analysis. This step is conducted per DBS-fMRI experiment and per threshold. It creates the design matrix in an "SPM.mat"-file. The following parameters have to be added in the fMRI model specification. First, the interscan interval, referring to the period between the start of two subsequent scans, equals 2 seconds. In 'Data & Design', the pre-processed data are added for the two sessions of one specific threshold. For each session, only one condition is specified because of the on-off stimulation paradigm. The reason behind this is that in fact only one regressor is needed to model the difference between the on- and off-condition [188]. The onset times and duration of each stimulation block is the same for the three sessions and is respectively [42, 102, 162, 222, 282] seconds and 20 seconds. The onset of the first block is chosen to be 42 seconds, instead of just 40 seconds, due to the temporal resolution of the experimental set-up. However, adding two extra seconds will not completely eliminate fluctuations due to asynchrony to the stimulation output, which is a confounder of the GLM analysis method. Other times of onset were tested as well, namely 41, 43 and 45 seconds. Next, the 'multiple regressors' option is used to add the parameters of realignment (i.e. the parameters of movement of the subject in the scanner) to the design. This was saved as an "rp….txt"-file for each data set after realignment. The default canonical HRF was selected as basic function, because it was shown in previous studies that the HRF of the rat is similar to the one of humans (with a response delay of approximately 2 seconds and a peak flow at approximately 5 seconds from stimulus onset) [189]. However, the shape and time-to-peak of the response function may vary substantially across brain regions and between different subjects. Therefore, a priori inserting of the stimulation paradigm in the model is another confounder of the GLM analysis method. Eventually, temporal and displacement derivatives are added as two additional regressors in order to introduce more freedom in the shape of the responses that one can model [188].

Once the model is specified, it can be fitted onto the actual data. This step is called 'estimation'. The classical algorithm for estimation is chosen, namely the Restricted Maximum Likelihood (REML). The difference between this method and the Maximum Likelihood is that: (1) REML maximizes the likelihood of the residuals (e= Y-ßX) instead of maximizing the likelihood of the data Y, (2) REML is used to estimate variance parameters instead of "mean" parameters ß, and (3) REML provides unbiased estimates instead of biased estimates of variance [190].

After estimation, the results can be reviewed per threshold (and per DBS-fMRI experiment). Therefore, the "SPM.mat"-file has to be loaded, which brings you in the contrast manager. Here, one has to specify different F-contrasts. Previously, when the model was fitted onto the data, each regressor (in each voxel of the brain) was assigned a certain ß-value. This value determined the amount of variance explained by that regressor [188]. Different ß's can now be combined to define a contrast of interest. An F-contrast was chosen because we want to assess whether any of the ß's, regardless of directions, explains a significant amount of the variance [188]. After defining the contrasts, SPM performs F-tests and calculates the F-maps. There is no masking with other contrasts applied. It is now asked to choose a p-value. With regard to the multiple comparisons problem, it can be a possibility to choose a Bonferroni-corrected p threshold. However, this correction method assumes the voxels to be independent from each other, which is not the case since the data are

actually spatially smoothened. Therefore, a multiple comparisons correction method based on Random Field Theory and cluster-based thresholding is used. A more liberal uncorrected p-value (e.g. p<0.001) and a clustersize k are chosen for each stimulation intensity as the extent threshold for display. The uncorrected p-value is divided by the amount of independent tests and compared to the most significant uncorrected p-value of all clusters that still activate. When this value exceeds p=0.001, this means that there are still too many false positives and k must increase. In this way, an appropriate clustersize k can be chosen. The amount of resels (or independent tests) are estimated to be 3000 to 5000, since the rat brain consists approximately of 30.000 voxels with dimensions of 0.312x0.312 mm^2 and only 14 slices were recorded.

3.6.2.2 Correlation analysis

In this study, functional connectivity is measured as the temporal correlation of neuronal activity between an *a-priori* selected region-of-interest (ROI) and all the other brain voxels. Using this method for assessing functional connectivity, it is of critical importance to choose an appropriate seed region with a valuable size and shape. ROIs were determined based on functional activations from our initial GLM analysis. A box with dimensions 1.5x1.5x1.5mm was drawn around the most activating voxels and their mean time series were determined by calculating the first eigenvariate in SPM8. Next, this mean time series of the ROI was correlated with the time series of each other voxel in the brain by means of a script, written in MATLAB 2011b. The output of the script resulted in a matrix of correlation coefficients, whereby a high correlation coefficient indicates that the voxel is highly correlated with the seed region. In this way, it is possible to define the regions that are most functionally connected with the seed region and thus reveal communication pathways of one region with another. In order to incorporate only brain slices of interest for correlation analysis, a mask consisting of zeros and ones was drawn in AMIRA 5.2.0. This means that axial slices from the most anterior and posterior side of the brain were not included in the mask, because no activation is expected in the olfactory organ and cerebellum, respectively. The mask was overlaid on the pre-processed EPIs by a simple multiplication of matrices in Matlab.

The complete Matlab script for masking and correlation analysis is added in Appendix A. It consists of four important steps. First, there is the masking of pre-processed EPIs (NIFTI format). Secondly, pre-processed time series are read from the NIFTI files. Thirdly, correlations are calculated and eventually, correlation matrices are drawn and written to NIFTI format for visualization in Amira. The most important parts of the script are explained below.

```
%(..)
scans=150;
for i=1:scans
    header=spm_vol(strcat(fn,fmri_files(i,1).name));
    [fMRI_data(:,:,:,i),XYZ]=spm_read_vols(header);
end
%(..)
[labels,XYZ2]=spm_read_vols(maskfile);
%(..)
for i=1:scans
    RR=fMRI_data(:,:,:,i).*labels;
    %(..)
end
```

Since each fMRI run consists of 150 repetitions (i.e. timepoints), the first loop of the script above stores data from the EPIs files in a 4D matrix ("fMRI_data") with dimensions 276x320x49x150. Next, a matrix "labels" is constructed consisting of zeros and ones, which represents the mask.

Multiplication of both matrices sets the intensity of all voxels outside the mask to zero and those inside the mask preserve their intensity value.

```
%(..)
for j=1:scans
    time_series(:,j)=reshape(fMRI_data(:,:,:,j),num_voxels,1);
end
sum_time=sum(abs(time_series),2);
time_series2=time_series(sum_time>0,:);
```

The loop of the script above reshapes the 4D matrix "fMRI_data" to a 2D matrix called "time_series". Its amount of rows corresponds to the amount of voxels and its columns to the 150 repetitions. "time_series2" incorporates only those voxels whose total time series are different from zero and thus fall within the mask.
In order to calculate the averaged BOLD responses of different sessions (recorded on different days) in one rat, intensity normalization has to be performed. Therefore, the following formula was applied in Matlab to bring each session to a common baseline:

$$\mathrm{Y(x,y,z,t)_{new}} = \frac{\mathrm{Y(x,y,z,t)} - \mu_{\mathrm{mean}}}{\sigma_{\mathrm{mean}}} \tag{14}$$

whereby Y(x, y, z, t) represents the intensity value as was recorded by the MRI scanner at a certain voxel position (x,y,z) and at a certain timepoint t in the 4D matrix, μ_{mean} represents the mean intensity value over all voxels and all timepoints, and eventually σ_{mean}represents the mean standard deviation over all voxels and all timepoints. When normalization is accomplished for all sessions, the next step is to take the average from those $Y(x,y,z,t)_{new}$ values in corresponding voxels and timepoints of all sessions. This then becomes the new matrix "time_series2".

```
activevoxels=length(time_series2);
K= zeros(activevoxels+1,scans);
K(1,:)=Yseed(1:scans,1)';
K(2:activevoxels+1,:)=time_series2;

firstrow=zeros(1,activevoxels);
for i=2:activevoxels+1
    R2= corrcoef(K(1,:)',K(i,:)');
    firstrow(1,i-1)=R2(1,2);
end
threshold=0;
places=find(abs(firstrow)>threshold);
%(..)
```

The script above calculates correlation matrices. A matrix "K" is constructed, whereby its first row corresponds to the time series of the seed region and the other rows correspond to the time series of all other brain voxels of interest. The loop will then correlate the first transposed row (i.e. the time series of the seed region) with all the other transposed rows (i.e. the time series of each brain voxel), using the built-in Matlab function *corrcoef.* The corresponding Pearson's correlation coefficients (CC) are calculated and stored in "firstrow". A threshold for the CC can be chosen, meaning that only those voxels with a correlation coefficient above the threshold are assumed to be correlated with the seed. The indices of all voxels with a CC above the threshold are stored in "places". Eventually (see Appendix A), these indices will be converted to the equivalent row and column subscripts from the "fMRI_data" matrix such that each CC can be found on the position of its corresponding voxel. These correlation maps are then overlaid on the structural MR in Amira for visualization.

It was chosen to apply exactly the same ROIs onto averaged results of all rats (within-subject analysis). Therefore, it was needed to draw ROIs as a matrix of zeros and ones (NIFTI-format) for the first rat, using MARSBAR and SPM8. They were drawn around the most significant activating voxels detected by GLM, as described above. In order to draw ROIs at exact the same location in the other rats, coregistration was applied in SPM8 of the structural MR of rat 1 (defined as 'source image') on the structural MR of rat 2 (defined as 'reference image') and also passing this transformation onto the seeds (defined as 'other images'). Mean time series of these ROIs could be extracted by the Matlab script below.

```
brainmask = 'G:\Data\PtIr14\ROI1.nii';
maskfile = spm_vol(brainmask);
[labels,XYZ]=spm_read_vols(maskfile);
eln=find(labels==1);
timeseries_ROI_mean=zeros(num_voxels,150);
k=1;
for i=1:num_voxels
    if som_time(i,1)>0
       timeseries_ROI_mean(i,:)=time_series2(k,:);
       k=k+1;
    else timeseries_ROI_mean(i,:)=0;
    end
end
Yseed=mean(timeseries_ROI_mean(eln,:),1)';
```

The script above reads in the brainmask and makes a matrix of zeros and ones from it ("labels"). The column "eln" consists of the locations of the ones in the 4D matrix "fMRI_data". The loop then extracts the corresponding time series from the matrix "time_series2" (which was described earlier) and calculates the mean time series from it, defined as "Yseed".

Chapter 4

Results

4.1 Data acquisition

4.1.1 Shimming

Before the BOLD-fMRI data acquisition was started, shimming is performed to improve magnetic field homogeneity. As stated before (Section 3.5), the shimming protocol was based on a fieldmap procedure over the volume of interest. A fieldmap such as in **Figure 50a** was acquired and a correction to compensate for magnetic field inhomogeneities was calculated. **Figure 50b** shows an example of a bad shim. The variance in colors points out that the field is not homogenous at all. Three methods can be applied in order to improve shimming results. First, the animal can be repositioned and a new fieldmap is acquired to check for possible improvements in homogeneity. Secondly, the amount of anesthesia can be increased to decrease movements. And a last option is to decrease the signal-to-noise ratio of the fieldmap.

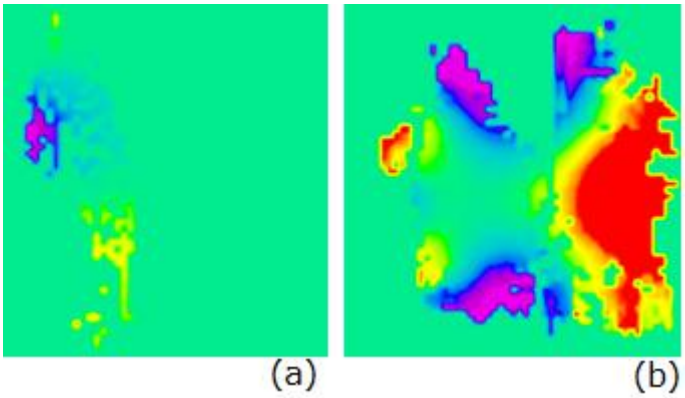

Figure 50: a) Good shim, b) Bad shim.

4.2 Pre-processing

Six methods were considered to find the best combination of pre-processing steps: (1) Only pre-processing, (2) Detrending + pre-processing, (3) Filtering + pre-processing, (4) Detrending + filtering + pre-processing, (5) Pre-processing + filtering and (6) Detrending + pre-processing + filtering. The different methods were tested on one dataset of one rat, for the 90% threshold. **Figure 51** depicts the results of all methods. The left figures show the plots of the BOLD response vs. time series (eigenvariate plots) for the whole brain. The right figures show the activation maps as were generated by GLM in SPM. Cluster-based thresholding in combination with RFT is chosen to correct the p-value as threshold for display.

Figure 51 method 1 shows the result after conducting the three 'pre-processing' steps (realignment, coregistration, smoothing). When choosing a high cluster threshold (i.e. k=22300), there is a lot of activity seen at the periphery of the brain (see white arrow). The p-value was chosen

to be 0.05. When lowering to p=0.001, almost no activity is remarked (except for some activity in hippocampal substructures ipsilaterally from the DBS electrode). When adding detrending before pre-processing (**Figure 51 method 2**), the results show that detrending has almost no influence on the BOLD response vs. time series of all voxels. Also the activation maps remain similar as without detrending. When using filtering before pre-processing (**Figure 51 method 3**), the results become more significant (p-value can be lowered) but the time series cannot be easily correlated to the block paradigm (see black arrow). This is not solved by adding detrending as well (**Figure 51 method 4**). Moreover, despite the fact that a small cluster threshold was chosen (k=4100), contralateral activity seems to disappear (see white arrow). The optimal results are seen when filtering was performed after pre-processing (**Figure 51 method 5**). Adding detrending in this case (**Figure 51 method 6**) does not involve any added value, because activation maps show also major activation in the periphery of the brain (i.e. in regions where no activation was expected) when choosing a high cluster threshold (k=22800). Moreover, contralateral activation seems to be gone.

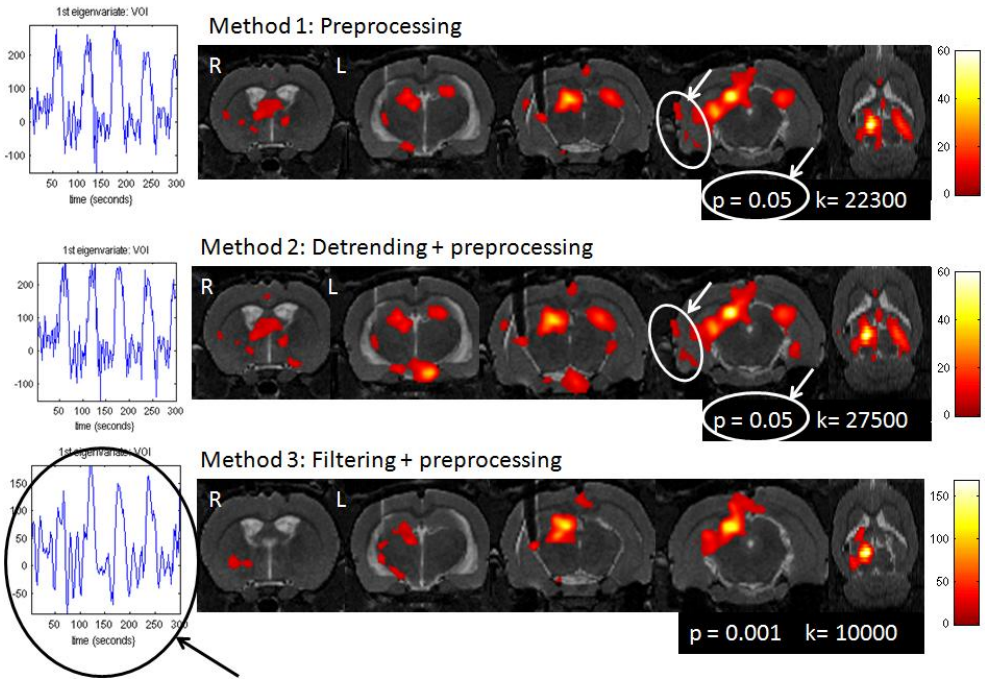

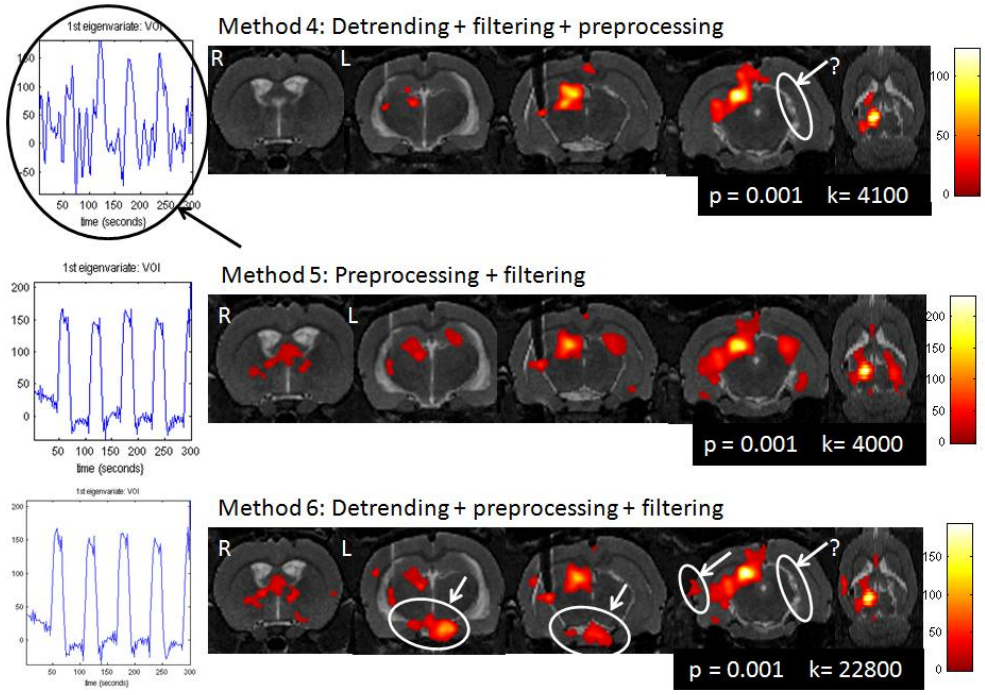

Figure 51: Six methods were compared in order to find the optimal combination of pre-processing steps. Left figures depict the BOLD response vs. time series for the whole brain. Right figures depict activation maps, whereby an appropriate p-value and cluster threshold k was chosen. Four axial slices and one coronal slice are shown. White arrows refer to activation in unexpected regions; white arrows in combination with '?' refer to regions were activation is expected but not seen. Black arrows refer to badly correlated time series.

4.3 Statistical analysis

Statistical analysis was performed by means of two techniques: voxel-wise analysis using the General Linear Model (GLM) and seed-ROI based Correlation Analysis (CA). Since the electrode is implanted in the right hippocampus, it is expected that different areas of the hippocampal formation will be uni- or bilaterally activated, depending on the stimulation intensity. The hippocampal formation consists of the subiculum (corresponding to hippocampal output), the hippocampus itself (CA1, CA2, CA3), the dentate gyrus (corresponding to hippocampal input) and eventually the entorhinal, ectorhinal and perirhinal cortex (corresponding to the cortical input). All regions are known to be tightly connected to each other, not only ipsilateral (side of implanted electrode) but also contralateral via hippocampal commissural fibers that connect the hippocampi of both hemispheres. It is demonstrated in this study that unilateral DBS causes a significant increase in BOLD response, both in ipsilateral and contralateral hippocampal and thalamic substructures depending on the stimulation intensity. Depending on the analysis technique, additional structures that could be modulated by DBS include hypothalamic mammillary bodies, septal nuclei, parahippocampal and cingulate cortex. More detailed results from our two analysis techniques are described below.

4.3.1 General Linear Model

4.3.1.1 Analysis of one session

Activation maps are shown in **Figure 52** for one session in one rat (rat 1). This particular session and rat was chosen because of highly significant results for the stimulation intensity of 90% of the threshold. More in specific, even when the strongest FWE correction for multiple comparisons at the voxel level was applied in SPM, highly significant BOLD responses are still detectable in the expected regions. This is not the case for any other session of the other rat. The most probable explanation for this is that first of all GLM requires an a priori insertion of the hemodynamic response function, which is likely to differ between- and within-subjects and brain regions.

Our results show that for low current intensity, different regions such as hippocampal structures and piriform cortex are activating. With increasing stimulation intensity, additional activating structures include several cortical limbic structures (such as the entorhinal, ectorhinal and perirhinal cortex), thalamic structures, septal nuclei and mammillary bodies (part of hypothalamus). At 90% of the threshold, a bilateral BOLD response in hippocampal, thalamic and cortical limbic structures is detected. Hence, increasing the stimulation intensity goes together with more contralateral hippocampal tissue activation. **Figure 53** gives more clarity about the different substructures of the hippocampal formation (dentate gyrus, subiculum, hippocampus proper, entorhinal cortex, ectorhinal cortex and perirhinal cortex) that are activating at 90% of the seizure threshold.

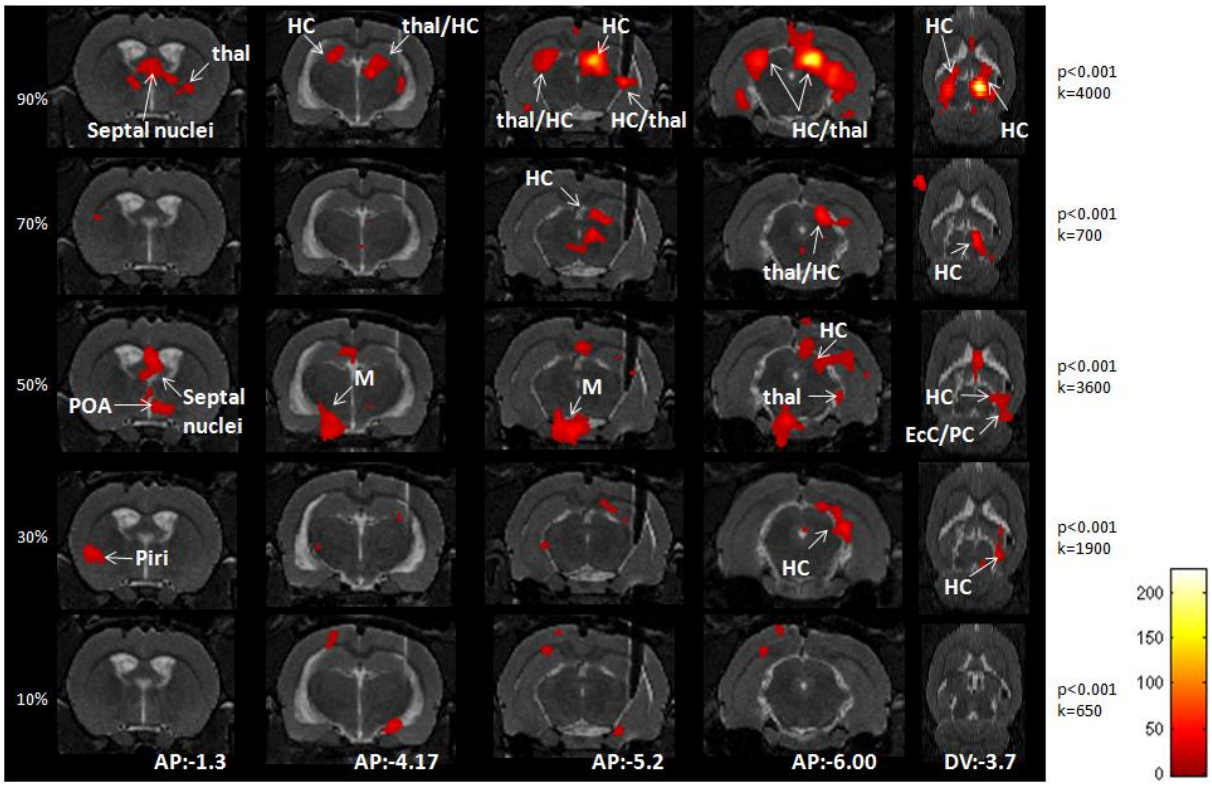

Figure 52: BOLD fMRI activation plots for session 1 of rat 1 during bipolar Poisson distributed DBS of the right hippocampus. The hippocampal structures (HC), thalamic structures (thal), ectorhinal cortex (EcC), perirhinal cortex (PC), mammillary bodies (M), septal nuclei, piriform cortex (piri) and preoptic area (POA) as part of the hypothalamus are labelled with white arrows. A multiple comparisons correction method based on Random Field Theory and cluster-based thresholding is applied. Voxels with p<0.0001 were considered as active and k represents the chosen cluster threshold per stimulation intensity. The colorbar represents percent signal change with respect to a whole-brain mean signal intensity scaled to 100, as is automatically done in SPM.

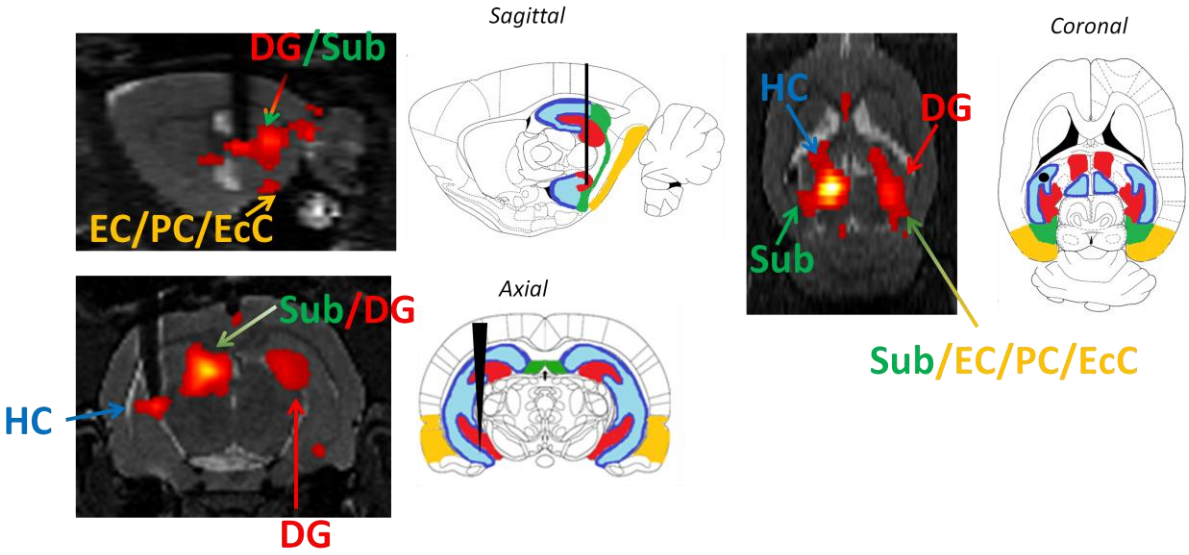

Figure 53: Different substructures of the hippocampal formation are activating at 90% of the seizure threshold. These structures include subiculum (SUB; green), dentate gyrus (DG; red), hippocampus proper (HC; blue) and entorhinal, perirhinal and ectorhinal cortex (EC/PC/EcC; yellow).

Our findings indicate that the amount of active voxels in the brain (p_{corr}<0.001) increases in an approximately linear way (R^2=0.9378) with increasing stimulation intensity (**Figure 54**). Whether this goes together with an increase in spatial extent of the hDBS-induced BOLD responses at the ipsi- and contralateral hippocampal formation is also investigated. The spatial extent is characterized by the ratio of the amount of significant (p_{corr}<0.001) activating voxels in the ipsi- and contralateral hippocampus to the total ipsi- and contralateral hippocampal volumes, respectively. **Figure 55** shows that higher stimulation intensity leads to more activating hippocampal volume at the ipsi- and contralateral side, whereby the amount of activating voxels at the ipsilateral HC stays higher. It can be concluded that the activated tissue shifts more and more to the contralateral side with increasing current intensity and that the BOLD response becomes more widespread. These results only indicate a trend and further investigation is necessary in order to investigate the true relationship between current intensity and the level of BOLD response changes.

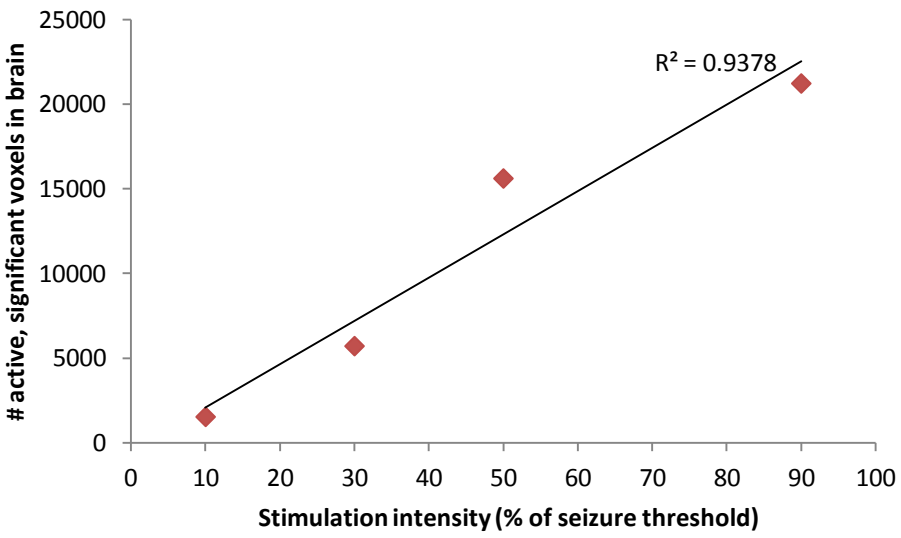

Figure 54: A linear relationship is observed between the amount of activating voxels in the brain (p_{corr}<0.001) and the stimulation amplitude. The latter is determined as the percentage of the seizure threshold of the individual rat (550µA in this rat). The stimulation amplitude that corresponds to 70% of the seizure threshold was not included due to very small brain activity during stimulation.

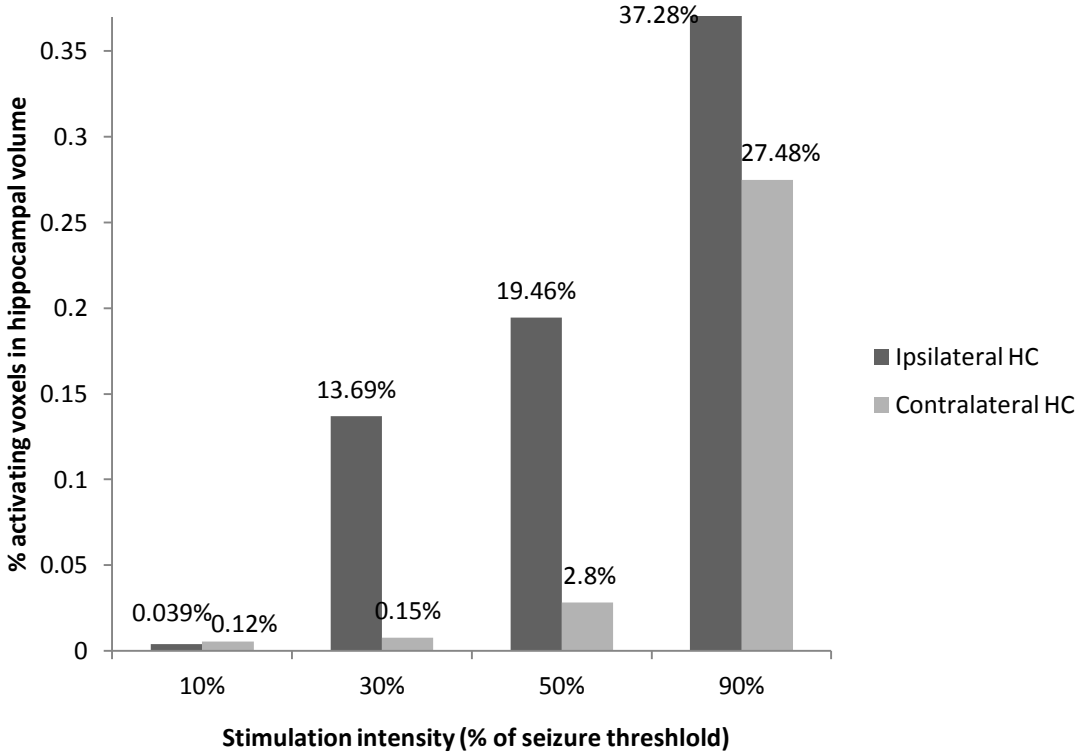

Figure 55: Graph illustrating the relation between the stimulation intensity during hDBS and the spatial extent of the hDBS-induced BOLD responses in the ipsi- and contralateral hippocampal formation (HC). The stimulation intensities were determined as the percentage of the seizure threshold of the individual rat (550 µA in this rat). The spatial extent is characterized by the ratio of significant (p_{corr}<0.001) activating voxels in the ipsi- and contralateral hippocampal formation to the total ipsi- and contralateral hippocampal volume, respectively.

4.3.1.2 Analysis of averaged sessions

BOLD responses to DBS were also investigated for the other sessions in rat 1 in order to search for longitudinal stability of the activating regions. Also the other rat was analyzed using the general linear model (GLM) in SPM. Averaged results for rat 1 and 2 were rather inconsistent and no trends as seen in session 1 of rat 1 could be derived by GLM. This is probably due to constraints that are imposed by GLM, as explained before. **Figure 56** shows the averaged BOLD responses in rat 1 for two sessions (each session consisting of two repeated recordings). The third session had to be excluded from the study because of motion artefacts.

Activation in hippocampal, thalamic and cortical limbic structures are consistently detectable in the averaged results over several sessions, pointing out that these regions show a stable BOLD response to hDBS. It needs to be remarked that the scale of the colorbar is different from Figure 52. Other regions (such as substantia nigria (SNR), superior colliculus (Coll), hypothalamic mammillary bodies (M) or pons) show occasionally activity, but their presence and how they change with stimulation intensity is never consistent. Also the trend towards increased bilateral activity with increasing stimulation intensity is less clear from these results. Therefore, it was chosen to focus on correlation analysis for further investigation of network-induced activation by DBS (see next Section).

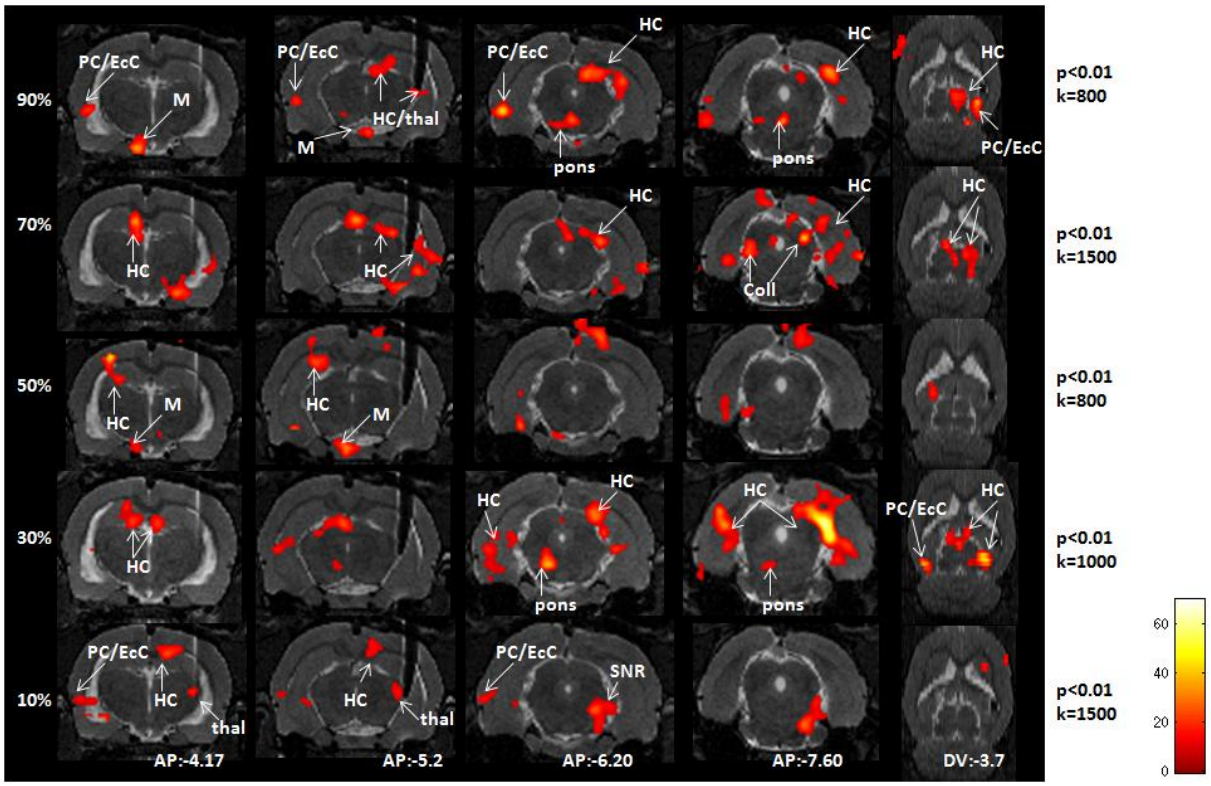

Figure 56: BOLD fMRI activation plots during bipolar Poisson distributed DBS of the right hippocampus of one rat. The hippocampal structures (HC), thalamic structures (thal), ectorhinal cortex (EcC), perirhinal cortex (PC), mammillary bodies (M), pons, substantia nigria (SNR) and colliculus (Coll) are labelled with white arrows. A multiple comparisons correction method based on Random Field Theory and cluster-based thresholding is used. Voxels with p<0.01 were considered as active and k represents the chosen cluster threshold per stimulation intensity. The colorbar represents percent signal change with respect to a whole-brain mean signal intensity scaled to 100, as is automatically done in SPM.

Eventually, it was also investigated whether the intensity (i.e. amplitude) of the BOLD response also increases with increasing stimulation intensity. Therefore, the whole-brain maximal and mean BOLD intensities were extracted from the averaged time series of all sessions within one rat for each stimulus intensity, using Matlab. The maximal BOLD intensity was calculated by applying formula 14 (Section 3.7.2) directly on the averaged time series of all sessions. The mean BOLD intensity was directly extracted from the time series in Matlab (arbitrary units as recorded by the fMRI scanner). Results are summarised in **Table 1**. The results show that both maximal and mean BOLD intensities are largely independent from stimulation intensity. As an illustration, **Figure 57** depicts the BOLD response vs. time series for each of the five stimulation intensities in one session of rat 1. Other sessions show similar results. It is confirmed by these graphs that the *amplitude* of the BOLD response remains approximately unaltered for all the different stimulation intensities.

Table 1: Whole-brain maximal and mean BOLD intensities for different stimulation intensities in both rats. The maximal intensity is calculated using formula 14 (section 3.6.2) on the averaged time series of all sessions. The mean intensity [arbitrary units] is directly extracted from the time series in Matlab. It is established that there is no dependence on stimulation intensity.

	RAT 1		RAT 2	
	Max. BOLD int.	**Mean [a.u.]**	**Max. BOLD int.**	**Mean [a.u.]**
90%	4.4832	7040.5	2.1944	10854
70%	4.7353	6808.8	2.2211	10817
50%	4.7451	6740.7	2.3033	10715
30%	4.5938	6820.7	2.2611	10438
10%	4.6562	6609.7	2.3846	10458

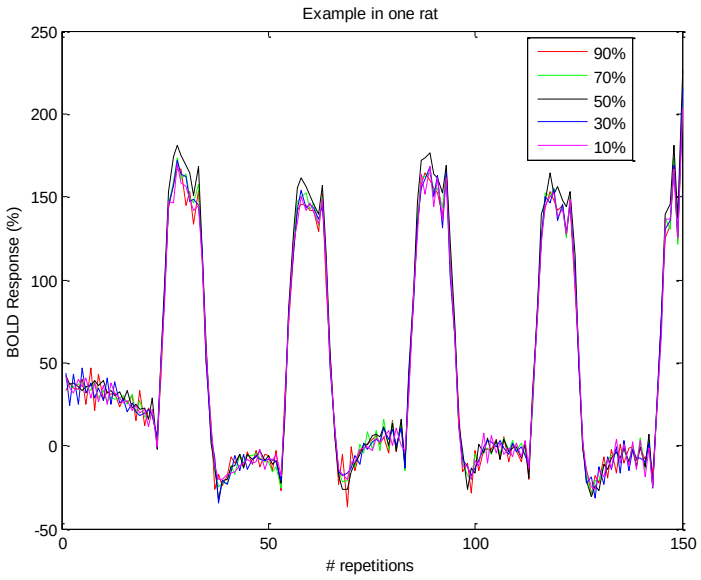

Figure 57: BOLD response (%) as a function of 'time' (i.e. 150 scans were taken with a TR=2s) for five different stimulation intensities. The stimulation intensities were determined as the percentage of the seizure threshold of the individual rat (550 μA in this rat). It is concluded that the amplitude of the BOLD response is independent from stimulation intensity. The vertical axis represents percent signal change with respect to a whole-brain mean signal intensity scaled to 100, as is automatically done in SPM.

4.3.2 Correlation Analysis

4.3.2.1 Analysis of one session

Seed-based correlation analysis was first conducted for the first session of rat 1, since this session showed significant activation results in expected brain areas, as was explained in the previous section. Seeds were chosen based on the most significant activating areas from our initial GLM analysis. For 90% of the seizure threshold, these regions include the medial/lateral ventral part of the septal nuclei (AP: Bregma+0.72mm), hypothalamic medial/lateral mammillary bodies (AP: Bregma-4.7mm), hippocampus right (side of electrode implantation) and hippocampus left (AP: Bregma-5.76mm and Bregma-6.24mm, respectively). It is known that the septal nuclei receive reciprocal connections from the hippocampus via the fornix. The mammillary bodies, which are considered as a part of the medial zone of the hypothalamus, act as a relay for impulses coming from hippocampus, going via the mammillo-thalamic tract to the thalamus [192]. The mean time series (BOLD response vs. amount of recorded scans) of all seeds were extracted by means of SPM8 and are depicted in **Figure 58**. The results show that the onset of stimulation differs between different seeds and that their onsets also lag the onset of the stimulation paradigm. Indeed, it is known that some regions might show later or earlier BOLD response than the canonical HRF due to local differences in vasculature or in strength of connections with the stimulation site. The stimulation block paradigm is assumed to start at 40 seconds (i.e. scan 20). It is seen from the graph that mammillary bodies and septal nuclei began to activate at approximately 46 seconds (i.e. scan 23) in this particular session for stimulation at 90% of the seizure threshold, while the left and right hippocampus activate at approximately 42 seconds (i.e. scan 21).

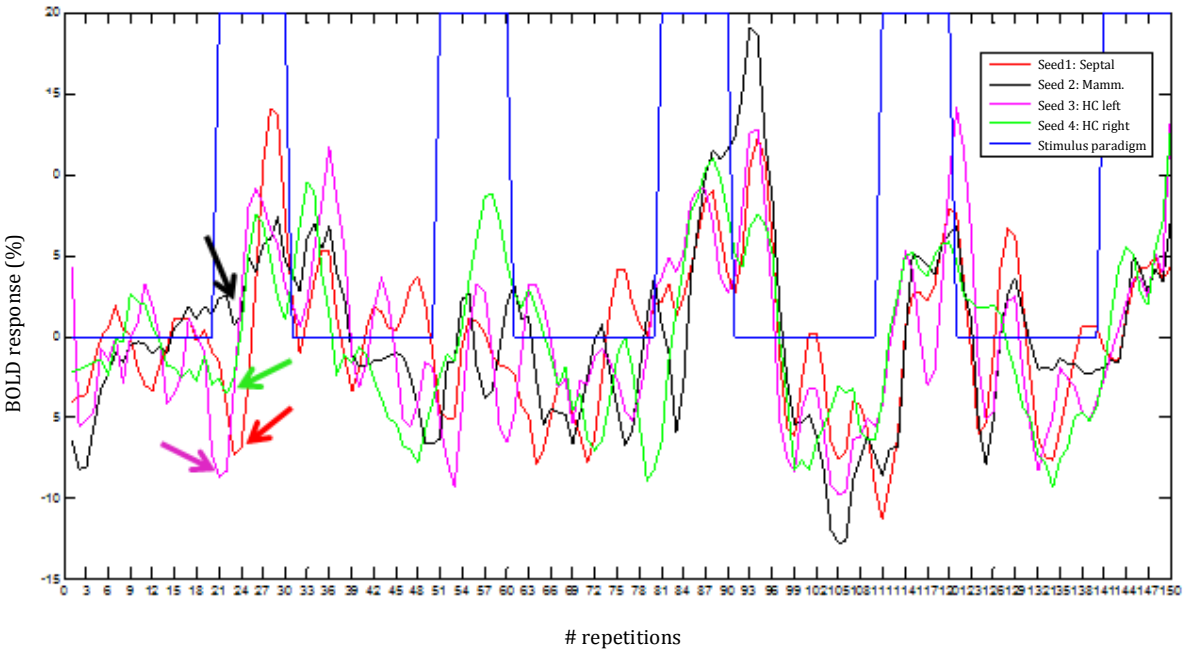

Figure 58: Mean time series of 4 seeds at 90% of the seizure threshold (550µA in this rat) for session 1 of rat 1. Seed 1 consists of the lateral/medial septal nuclei (red), seed 2 consists of the mammillary bodies (black), seed 3 consists of left hippocampal structures (pink) and seed 4 of right hippocampal structures (green). The stimulus paradigm (blue) encloses 5 stimulation epochs of 10 scans (i.e. 20 seconds) and 5 rest periods of 20 scans (i.e. 40 seconds). The time series of all seeds largely follow the stimulation paradigm. However, their onsets lag the onset of the stimulation paradigm (see arrows).

These four seeds were then correlated with all other voxels in the brain using a correlation coefficient threshold of 0.4. Negative correlation coefficients (i.e. anti-correlation) were very low and thus not considered as significant. **Figure 59** depicts the correlation maps for three of the four seeds at 90% of the seizure threshold. The fourth seed (i.e. right hippocampal structures) shows a rather weak correlation map, probably because this seed was rather located in areas of the superior colliculus than in the hippocampal area itself. It is seen that both mammillary bodies and the septal nuclei have relatively strong connections with each other, as well as with left and right hippocampal structures, anterior thalamic structures (to a rather limited extent), cingulate cortex and entorhinal and perirhinal cortex. All those areas belong to the Papez circuit [192]. The entorhinal cortex is the most important region of what is called the "parahippocampal cortex" (other regions include the perirhinal cortex, pre- and parasubiculum [193]), forming together with the cingulate cortex the "limbic cortex". The mammillary bodies, as a part of the medial zone of the hypothalamus, form also connections with other areas of the hypothalamus such as the preoptic and tuberal zone.

Taking the left HC as a seed, connectivity is shown with hypothalamic mammillary bodies, septal nuclei, right HC and the parahippocampal cortex. However, connectivity with cortical structures as well as with thalamic structures is less clear. Connectivity maps were also drawn for stimulation at 50% and 30% of the seizure threshold. All their seeds were chosen based on highest significant activating areas as were detected by general linear modelling (Figure 52). For 50%, those areas include posterior hippocampus right (AP: Bregma-8.04mm), mammillary bodies (AP: Bregma-5.2mm) and septal nuclei (AP: Bregma-0.36mm). For 30%, those areas include posterior hippocampus right (AP: Bregma-8.04mm) and piriform cortex (AP: Bregma+0.36mm). Similar connections are seen at lower stimulation intensities, but connectivity with limbic cortical structures and contralateral hippocampal structures seems to decrease. Also the extent of correlated hippocampal structures seems to decrease with decreasing stimulation intensities for this session. The contralateral piriform cortex at 30% shows only weak connections with the dorsal hippocampus and mammillary bodies.

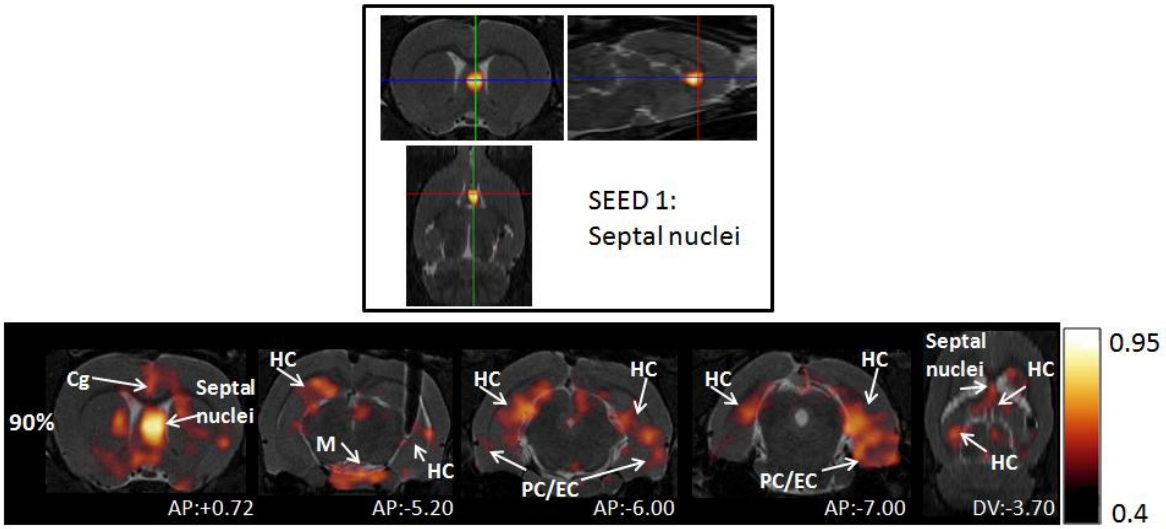

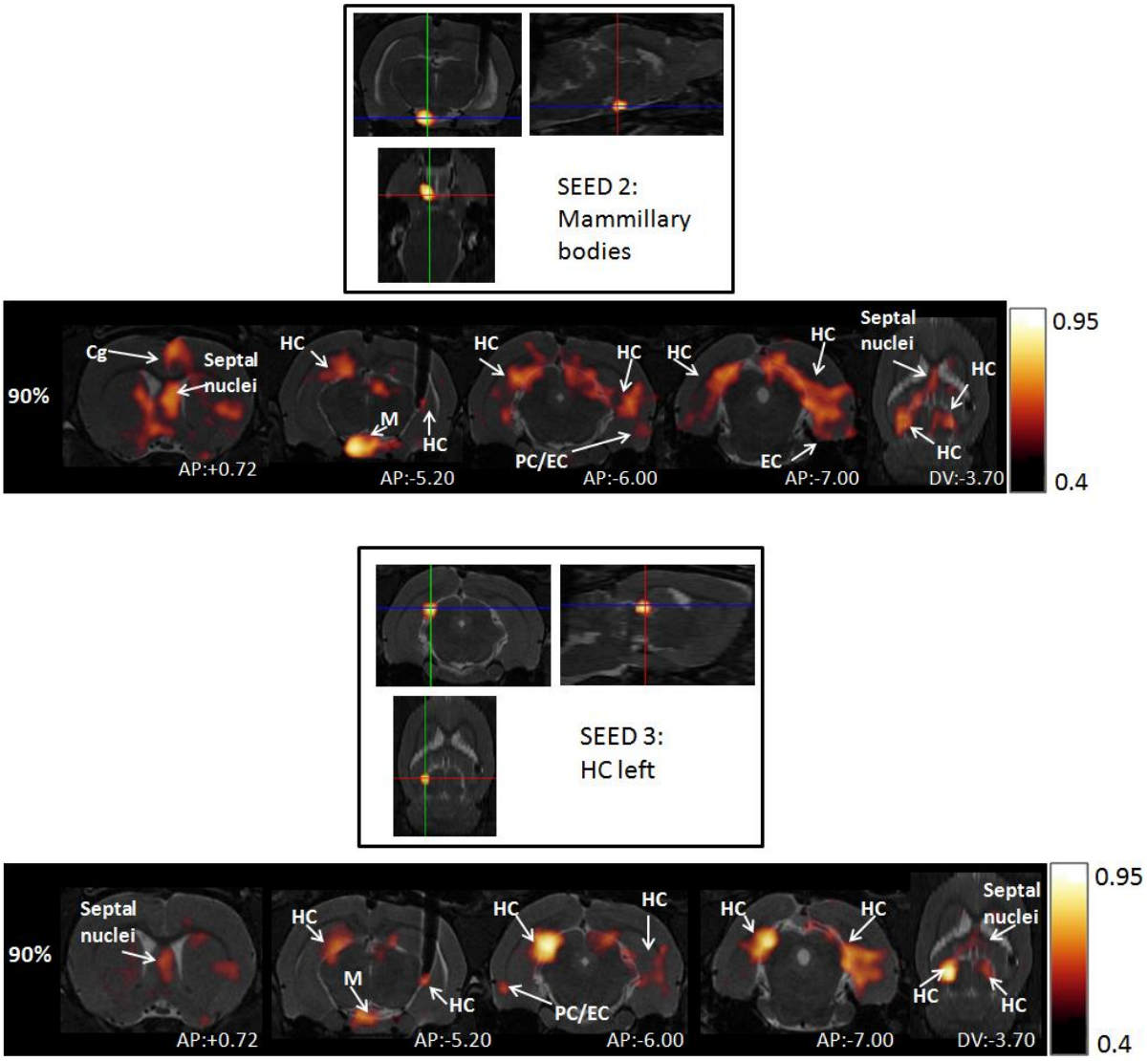

Figure 59: BOLD fMRI correlation maps for session 1 of rat 1 during bipolar Poisson distributed DBS of the right hippocampus. There was stimulated at a current intensity of 90% of the seizure threshold (550µA in this rat). The three seed regions are from top to bottom: the septal nuclei (AP: Bregma+0.72mm), mammillary bodies (AP: Bregma-4.7mm) and left hippocampus (Bregma-6.24mm). The hippocampal structures (HC), entorhinal cortex (EC), perirhinal cortex (PC), mammillary bodies (M), septal nuclei and Cg (cingulate cortex) are labelled with white arrows. The correlation coefficients range from 0.40 to 0.95.

Since the activation plots for 10% of the seizure threshold using GLM show no significant activation in expected regions, two fixed regions of interest are compared between 90% and 10% of the seizure threshold, namely HC left and HC right. Both mean team series of each ROI are depicted in **Figure 60**. The graphs show that the time series at 90% are more closely related to the stimulation paradigm than those at 10%. Their corresponding correlation maps are depicted in **Figure 61**. Our results indicate that network activity is more widespread for stimulation at 90% of the threshold compared to 10% of the threshold, for a fixed seed.

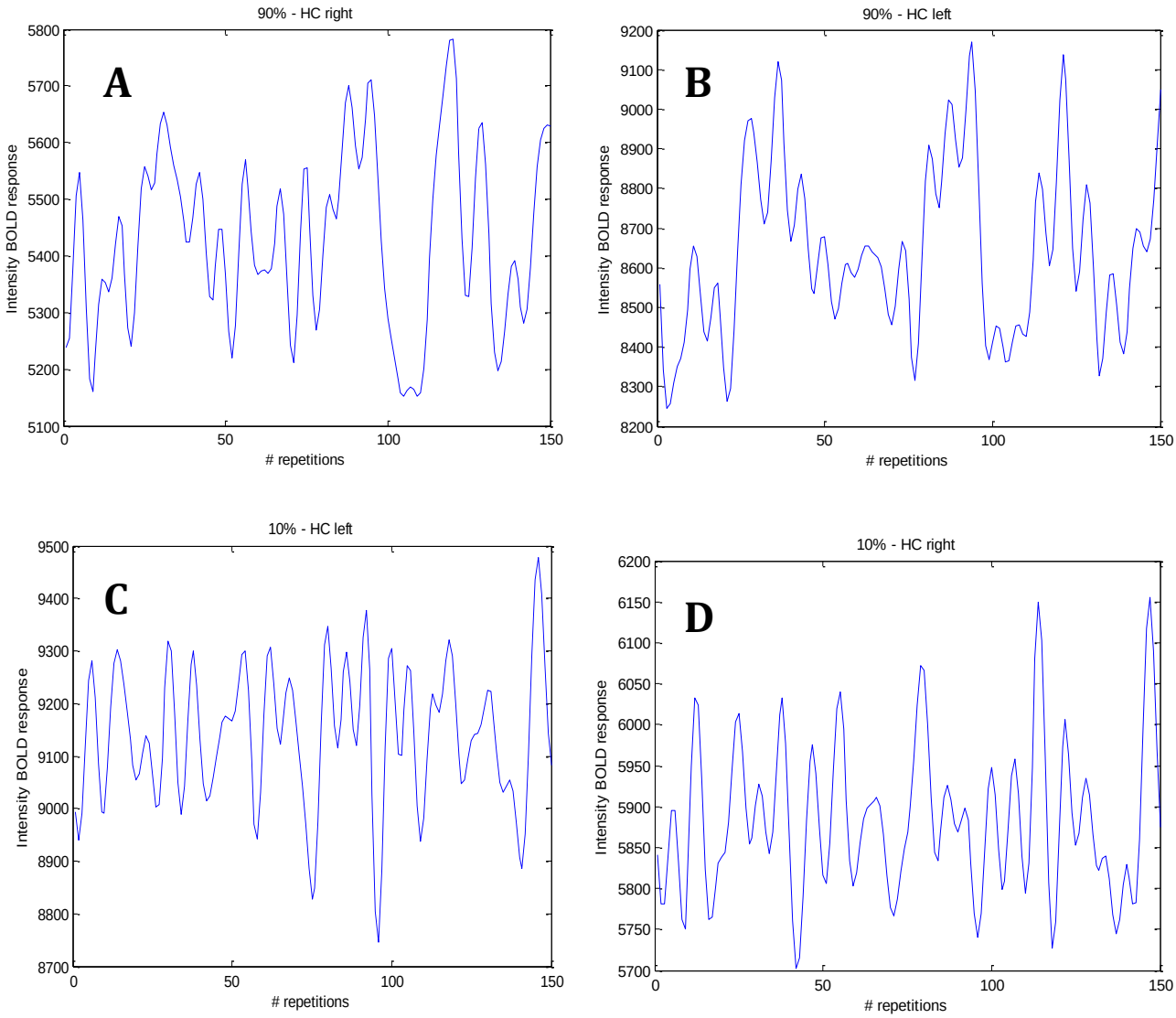

Figure 60: Mean intensity [a.u.] vs. time series of two fixed ROIs (left and right HC) for a stimulation at 90% of the seizure threshold (Figure A and B) and 10% of the seizure threshold (Figure C and D). Time series at 90% of the seizure threshold show a better correlation with the stimulation block paradigm.

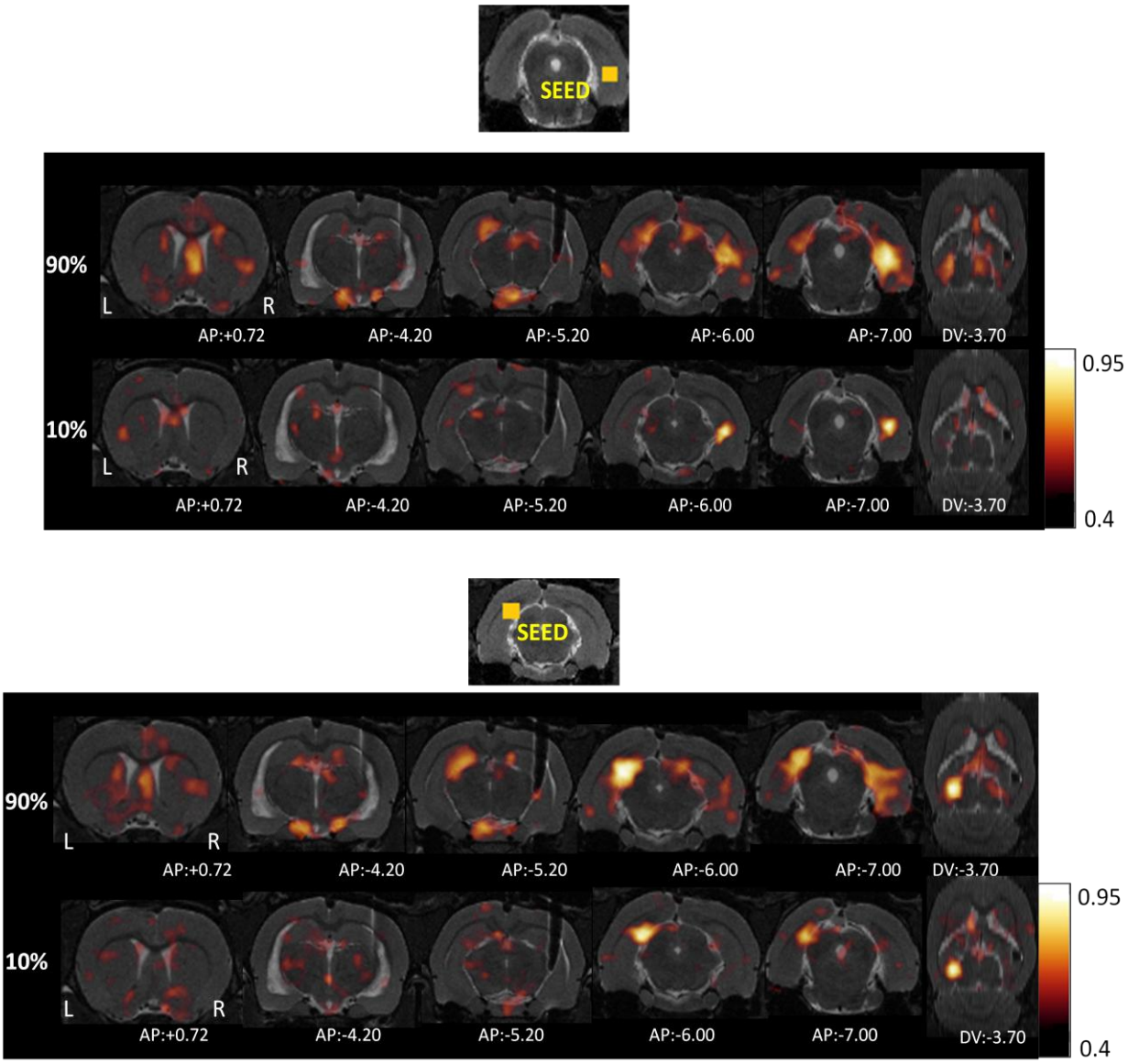

Figure 61: Comparison of two fixed seeds between stimulation at 90% and 10% of the seizure threshold (550µA in this rat). Above: right hippocampus (AP: Bregma-7mm), below: left hippocampus (AP: Bregma-6.00mm). Network activity is more extended for stimulation at 90% of the threshold compared to 10% of the threshold, for a fixed seed.

4.3.2.2 Analysis of averaged sessions

Two sessions of rat 1 and three sessions of rat 2, each consisting of two repeated DBS-fMRI recordings on their turn, were within-subject averaged using intensity normalization (formula 14 of section 3.6.2). Seeds of the first rat were determined based on significant activating regions as detected by GLM (Figure 56). The same seeds at exactly the same locations were used in de second rat. How they were determined was described in Section 3.7.2. For stimulation at 90% of the seizure threshold, the first seed corresponds to the contralateral lateral-medial zone of the hypothalamus (i.e. tuberomammillary nuclei and medial/lateral mammillary bodies) (AP: Bregma-4.20mm), the second seed corresponds to ectorhinal/perirhinal cortex (EcC/PC) (AP: Bregma-6.36mm) and the third seed to HC right posterior (AP: Bregma-7.56mm). Correlation maps for the first two seeds, using a CC threshold of 0.3, are depicted in **Figure 62** for rat 1 and **Figure 63** for rat 2. In the first rat,

mammillary bodies show strong correlation with septal nuclei, ipsi- and contralateral hippocampal structures and limbic cortical structures such as ectorhinal, perirhinal, entorhinal, (amygdalo)piriform and cingulate cortex. There is also connectivity with other regions of the hypothalamus such as the preoptic area. In the second rat, mammillary bodies show far more correlation with thalamic structures, but also connections with dorsal hippocampal structures (both left and right) and nuclei of the pons are seen. The second seed (contralateral EcC/PC) in the first rat shows relatively strong connections with limbic cortical structures (ipsilateral entorhinal, ectorhinal and perirhinal cortex, amygdalohippocampal area and (amygdalo)piriform cortex), ipsi- and contralateral hippocampal structures, as well as with cortical/medial amygdaloid nuclei, hypothalamic nuclei (preoptic area) and septal nuclei. Again, thalamic connections are more clear in the second rat, and hippocampal connections are rather absent.

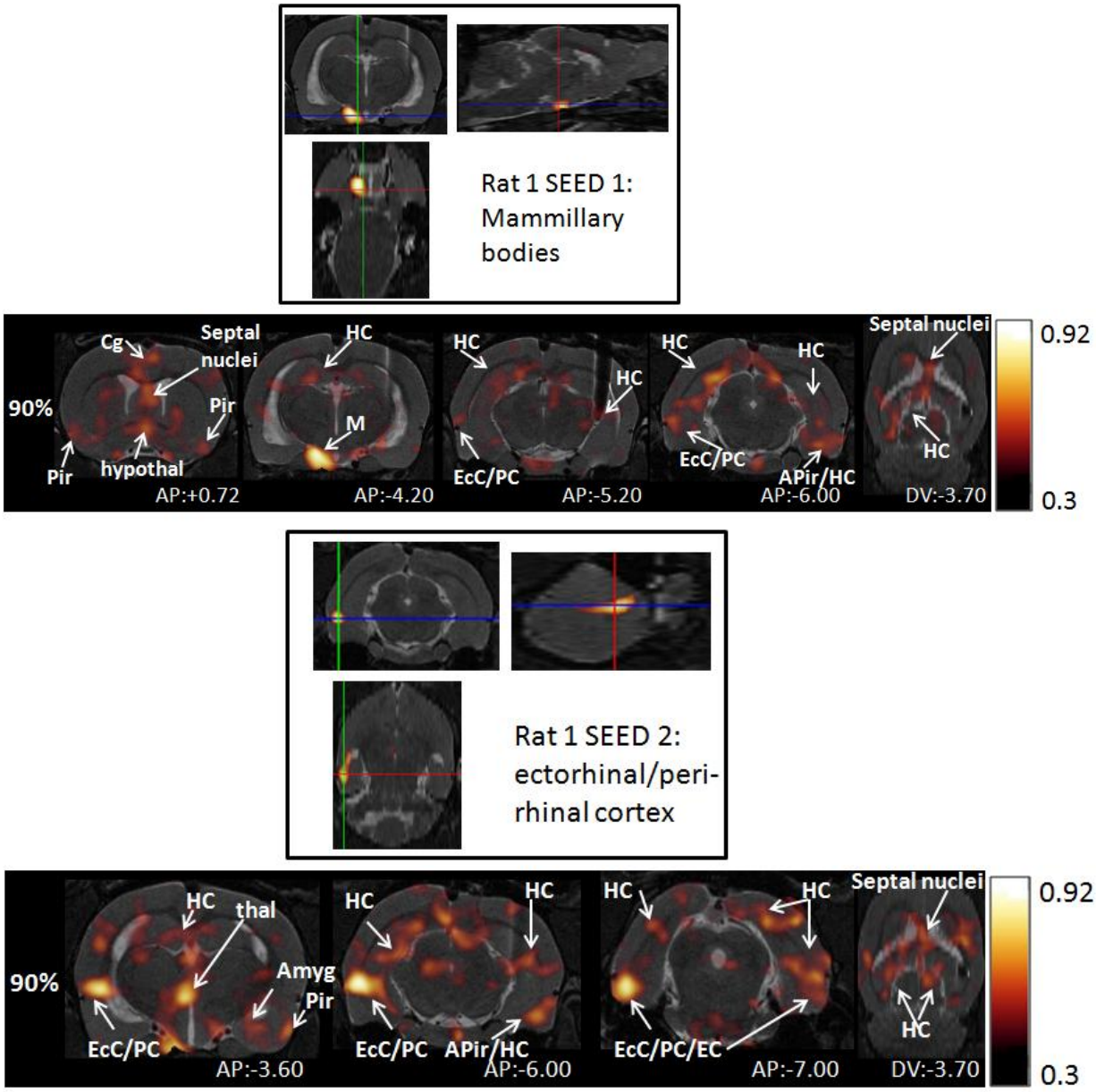

Figure 62: BOLD fMRI correlation maps for rat 1 during bipolar Poisson distributed DBS of the right hippocampus. There was stimulated at a current intensity of 90% of the seizure threshold (550µA in this rat). The two seed regions are from top to bottom: mammillary bodies (AP: Bregma-3.84mm) and ectorhinal/perirhinal cortex (AP: Bregma:-6.36mm).The hippocampal structures (HC), entorhinal cortex (EC), ectorhinal cortex (EcC), perirhinal cortex (PC), mammillary bodies (M), septal nuclei, amygdaloid nuclei

(Amyg), piriform cortex (Pir), amygdolapiriform cortex (APir), cingulate cortex (Cg) and thalamic structures (thal) are labelled with white arrows. The correlation coefficients range from 0.30 to 0.92.

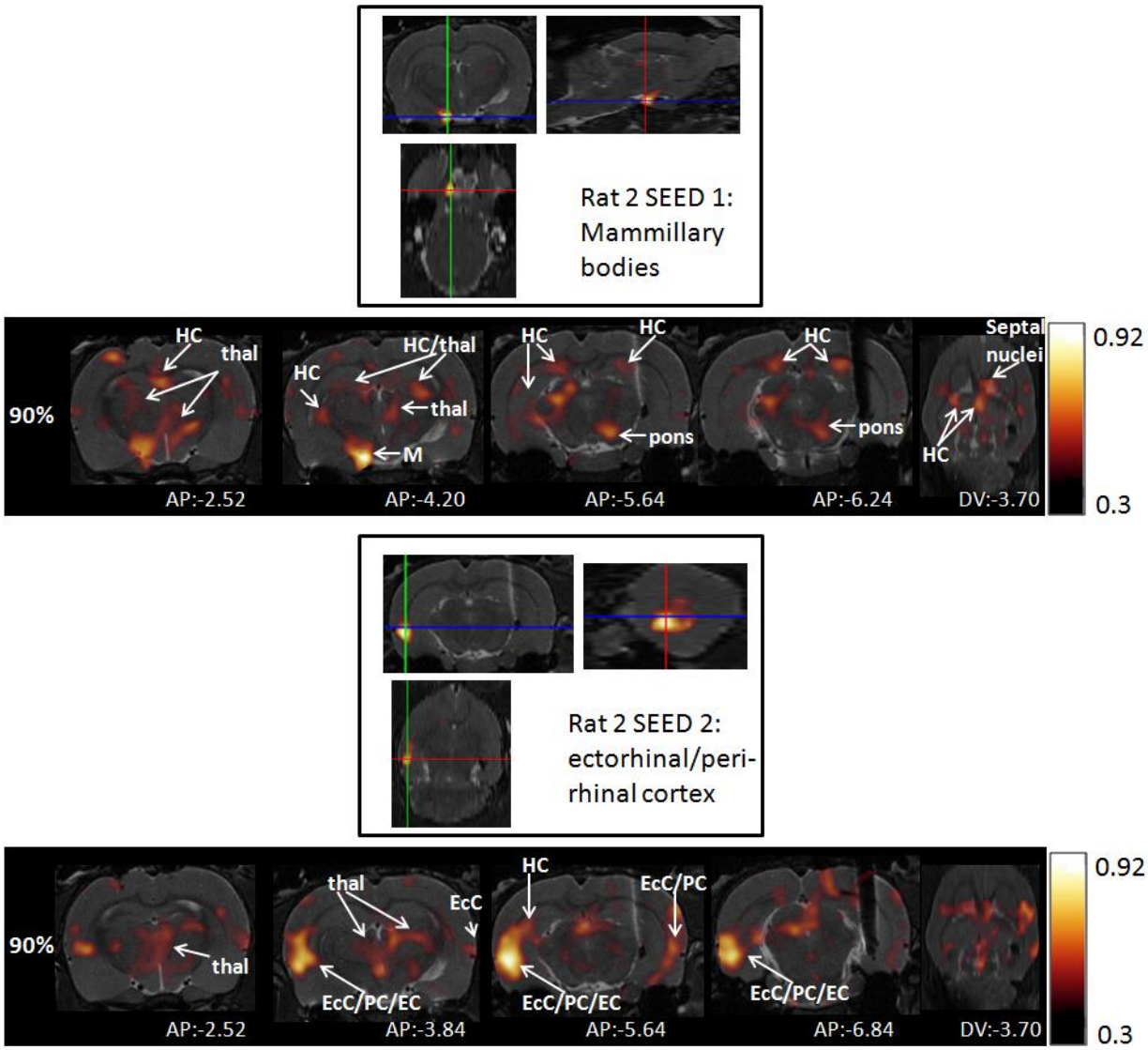

Figure 63: BOLD fMRI correlation maps for rat 2 during bipolar Poisson distributed DBS of the right hippocampus. There was stimulated at a current intensity of 90% of the seizure threshold (600µA in this rat). The two seed regions are from top to bottom: mammillary bodies (AP: Bregma-3.84mm) and ectorhinal/perirhinal cortex (AP: Bregma:-6.36mm).The hippocampal structures (HC), entorhinal cortex (EC), ectorhinal cortex (EcC), perirhinal cortex (PC), mammillary bodies (M), septal nuclei, thalamic structures (thal) and pons are labelled with white arrows. The correlation coefficients range from 0.30 to 0.92.

Correlation maps were also generated for all other stimulation intensities. At 70% of the seizure threshold, ipsilateral laterodorsal (AP: Bregma-2.76mm) and ventral (AP: Bregma-4.44mm) thalamic nuclei, as well as dorsomedial hypothalamic (AP: Bregma-2.76mm) seeds were chosen. Connections with contralateral thalamic structures are very strong as expected. Both hypothalamic and thalamic nuclei also connect reciprocally and relatively strong with each other. Connectivity with ipsi- and contralateral hippocampal structures is clearly seen in rat 1 and to a lesser extent in rat 2. Connectivity with mammillary bodies, cortical limbic structures and septal nuclei is present but not so strong. Also at 50% and 30% of the seizure threshold, several seeds were correlated with the brain. Largely spoken, there is the trend of seeds being less connected with hippocampal, (hypo)thalamic and limbic cortical structures at these lower stimulation intensities. At 10% of the

seizure threshold, only medial mammillary bodies (AP: Bregma-4.8mm) are found as a possible region of interest. For a correlation coefficient threshold of 0.3, connectivity is seen especially with hippocampal structures in the first rat and with thalamic structures in the second rat.

In order to draw conclusions about the relation between the extent (i.e. volume) of correlated regions on the one hand, and stimulation intensities on the other hand, two fixed seeds (left and right HC) were taken for all stimulation intensities. **Figure 64** shows the correlation of both seeds with all other brain voxels in rat 1, using a correlation coefficient threshold of 0.4. At 10% of the seizure threshold, there is almost no correlation of brain regions with either the left or right HC. At 30%, 50% and 70% of the seizure threshold, there is not much difference between the amount and extent of correlated regions, but there is certainly more correlation than at 10%. At 90% of the seizure threshold, there is a strong increase in the amount and extent of correlated regions compared to lower stimulation intensities. There is also a clear bilateral response detected. The correlation maps of rat 2 for the same fixed seeds and stimulation intensities show a similar trend. At 90% of the seizure threshold, regions that are most strongly correlated with the left HC include right HC, thalamic structures, mammillary bodies, septal nuclei and cortical limbic structures. Regions that are most strongly correlated with the right HC (side of the electrode) include left HC, mammillary bodies, medial septal nuclei and thalamic structures.

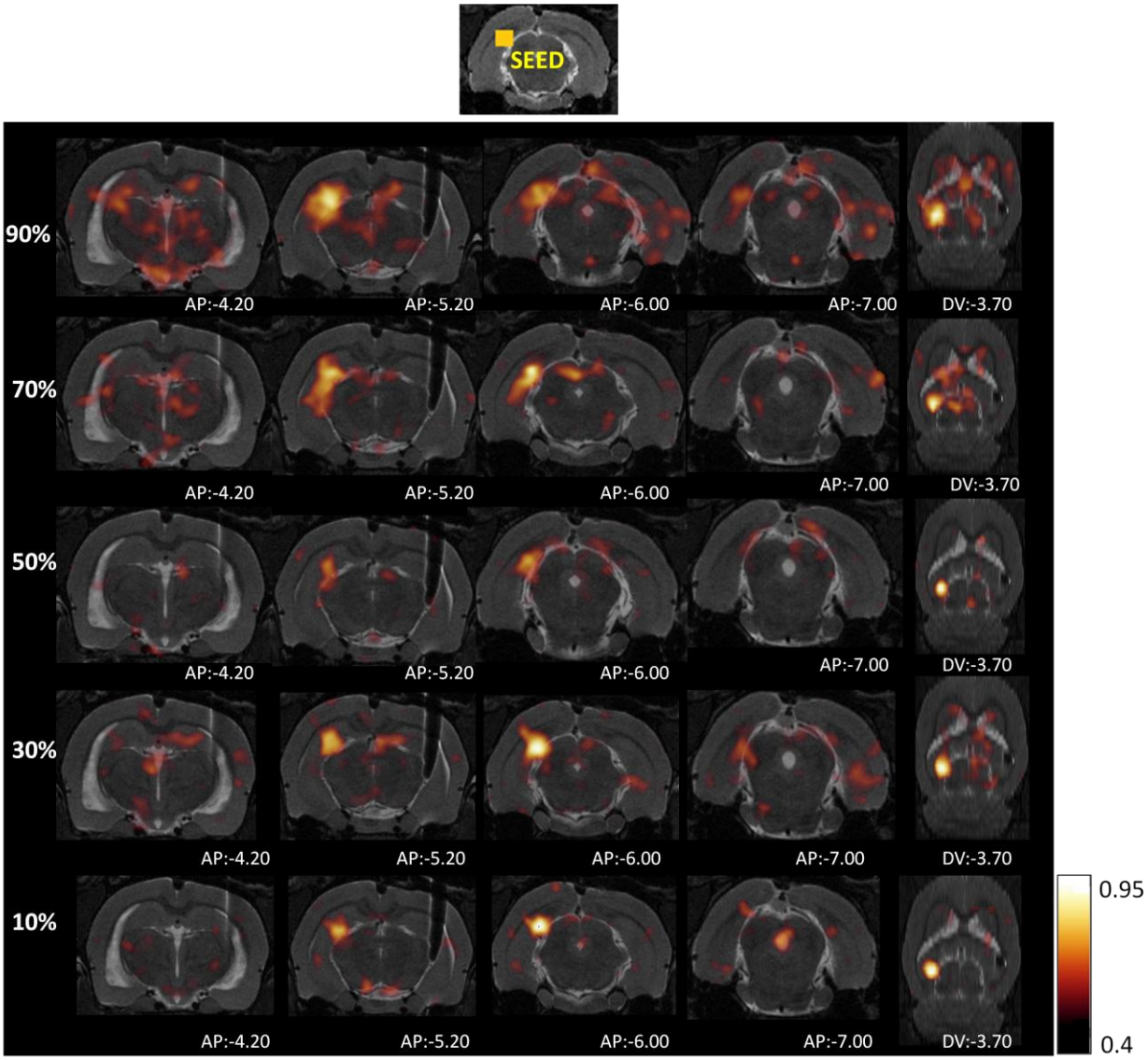

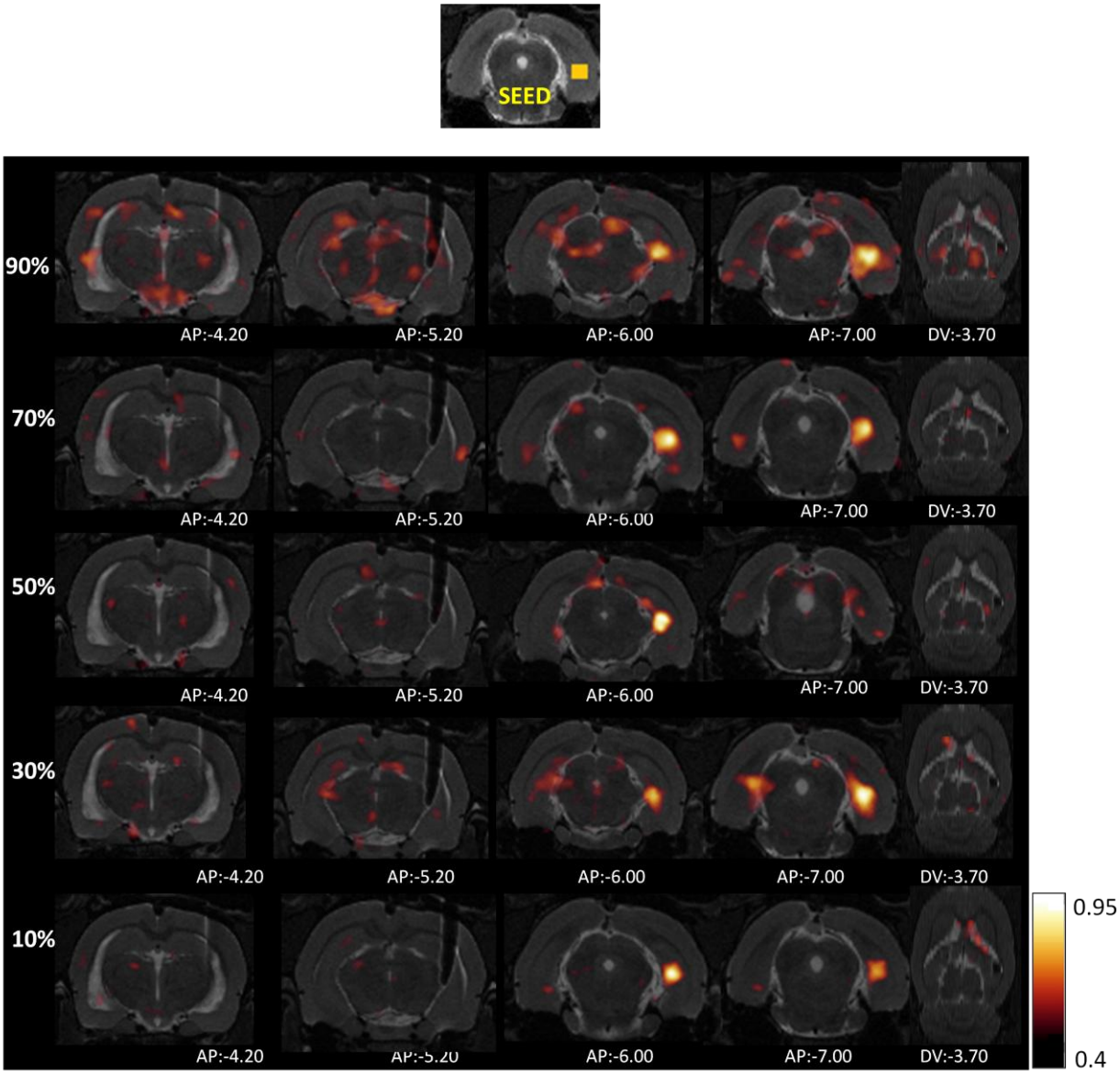

Figure 64: Comparison of two fixed seeds between stimulation at 90%, 70%, 50%, 30% and 10% of the seizure threshold (550µA in this rat). Above: left hippocampus (AP: Bregma-6.00mm), below: right hippocampus (AP: Bregma-7mm). At 90% of the seizure threshold, there is a strong increase in the amount and extent of correlated regions compared to lower stimulation intensities.

4.4 Post-mortem MRI

At the end of the experiment, each rat is euthanized by injecting an overdose Nembutal intravenously. Next, the electrode is removed from the brain and a structural MRI scan is taken. In this way, the extent of the lesion as caused by the electrode can be investigated (**Figure 65**) and the tip of the electrode can be exactly located. Furthermore, one can establish whether DBS has caused any structural brain damage by searching for areas that are brighter in one of the two hemispheres. It was concluded that no signs of local tissue damage could be observed on the structural MR images after the last fMRI scan was taken. Moreover, it could be confirmed that all the electrode tips were located in the hippocampus.

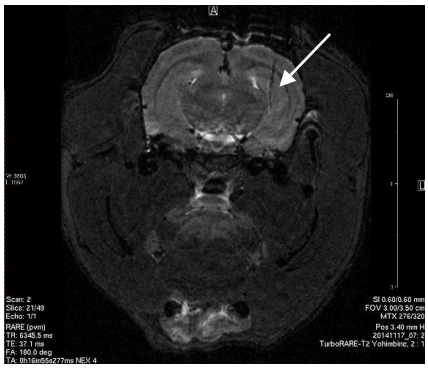

Figure 65: Post-mortem MRI scans: the original electrode tract (white arrow) is preserved.

Chapter 5

Discussion

Statistical analysis of fMRI data reveals that unilateral Poisson distributed hDBS influences the oxidative metabolism in different structures of the limbic system, including the hippocampal formation, (hypo)thalamic nuclei, amygdala, septal areas and the limbic cortex. With this study, our aim was to investigate whole-brain BOLD responses to hDBS in healthy rats anesthetised with medetomidine and to characterize the responses of different stimulation intensities. Using healthy rats eliminates brain pathology as a possible confounder. Furthermore, using medetomidine as the anesthetic minimizes the suppressive effect on neuronal activity and hemodynamic BOLD responses.

Whole-brain BOLD response of DBS

The current study reveals whole-brain effects in the hippocampal formation and other limbic structures that are anatomically connected with the hippocampus. This points out that hDBS not only causes local interaction at the site of stimulation but also in remote limbic pathways. Our findings are in line with the anatomical connections described by Rajmohan et al [133]. According to these authors, brain regions that constitute the limbic system are the limbic cortex (cingulate cortex, parahippocampal cortex, entorhinal cortex), the hippocampal formation (dentate gyrus, subiculum, hippocampus proper), hypothalamic mammillary bodies and the anterior nucleus of the thalamus. This anatomical model is referred to as the Papez circuit and is depicted in Figure 28. In the current study, anterior thalamic responses were especially detected in the second rat. Remarkably, its electrode was implanted more posteriorly in the brain, close to the pre-, para- and postsubicular areas (**Figure 66**). These findings correspond to those of Swanson et al [198], who declared that each component of the hippocampal formation has a distinctive pattern of efferent connections, whereby the projection to the anterior nuclear complex of the thalamus arises more posteriorly in the pre- and/or parasubiculum and the postsubicular area of the rat hippocampal formation. Taken together, it is possible that hippocampal-thalamic connections increase when the electrode is located in more posterior hippocampal structures. Additional electrode mapping experiments could be useful to investigate the true difference between a more anterior and more posterior implanted electrode.

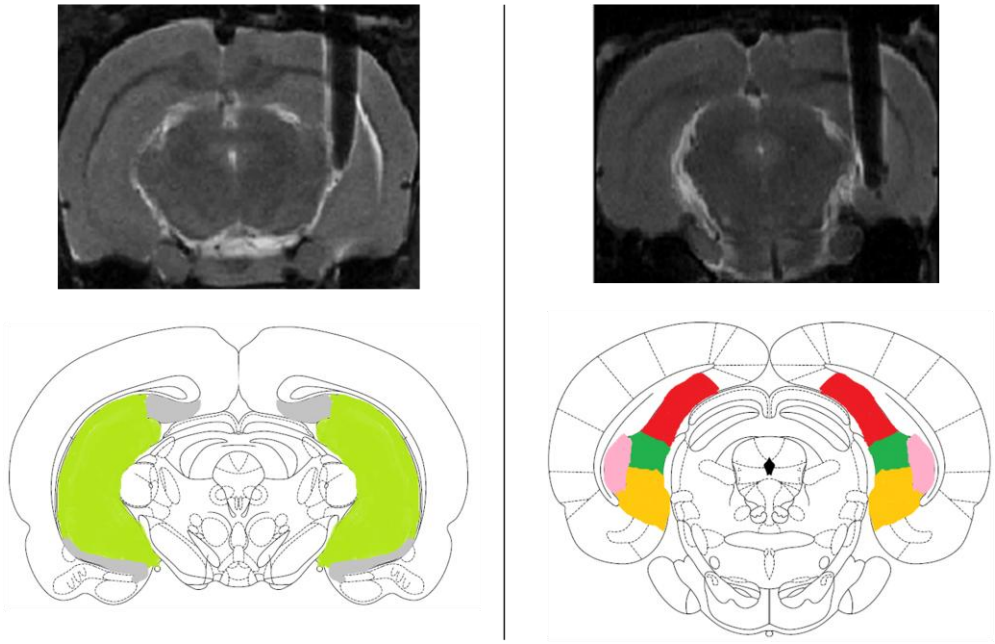

Figure 66: (left) Above: Structural MR of rat 1 (AP: -5.2 mm from Bregma); below: Axial slice from rat brain atlas [191] with light green corresponding to the hippocampal formation (CA I/II/III, DG) and grey to the ventral/dorsal subiculum. (right) Above: Structural MR of rat 2 (AP: -7mm from Bregma); below: Axial slice from rat brain atlas [191] with red corresponding to postsubiculum, green to presubiculum, yellow to parasubiculum and pink to subiculum (transition area). It is seen that in rat 2 the electrode is implanted more posteriorly in the brain, close to the pre-, para- and postsubiculum.

In addition, our results indicate not only local and distal effects induced by hDBS, but also indicate a bilateral nature of this effect, depending on the stimulation intensity. These findings are concordant with previous resting-state fMRI studies of the healthy rat brain. Those studies have shown that there is a reproducible functional connection between different limbic (cortical) structures such as hypothalamus, thalamic nuclei, cingulate cortex and hippocampus [194-196]. Moreover, these resting-state data displayed clear bilateral networks, indicating that the low-frequency fluctuations of left and right structures are similar in rats. Bilateral synchrony of fMRI signals is also detected in the current study, especially in limbic brain regions which are characterized by strong interhemispheric commissural connections such as the hippocampus [197].

Finally, our results indicate that the volume of the effect is dependent of the stimulus intensity. We were able to detect robust bilateral BOLD responses by means of Correlation Analysis (CC > 0.3-0.4) when a stimulation intensity corresponding to 90% of the seizure threshold was used. Differences in BOLD responses at lower stimulus intensities (i.e. 30%, 50% and 70% of the seizure threshold) were less clear, but compared to 90% the overall responses seemed less widespread and rather located ipsilaterally from the DBS electrode. Additional research on a larger group of animals is needed to develop a dose-response curve. Stimulation at 10% of the seizure threshold did not result in remarkable regions of increased connectivity. Taken together, our results suggest that a certain DBS intensity is required for visualisation of not only a local, but a whole-brain effect. Depending on the subject, below such a DBS intensity the BOLD response is very small or insignificant. Stimulation above this intensity results in robust bilateral and widespread responses, probably mediated by commissural fibers. The relationship between the spatial extent of the BOLD response and stimulation intensity was also established by previous rodent fMRI research whereby the perforant pathway was directly stimulated using non-chronically implanted electrodes. These studies revealed also a positive BOLD response in different areas of the hippocampal formation

[134,153-155], as well as an increase in spatial extent of the response with increasing stimulation intensity [134].

Additionally, we found some [^{18}F]FDG-PET studies in the healthy rat brain. Klein et al.[168] stimulated the subthalamic nucleus and concluded that unilateral DBS stimulation affects entire bilateral functional networks rather than isolated regions. Another study [160] investigated the effect of unilateral Poisson distributed DBS on the glucose metabolism while stimulating the hippocampus. The authors concluded that the glucose metabolism decreased in both the ipsi- and contralateral hippocampus and other limbic structures. They also saw that increased stimulation intensities lead to larger volumes being stimulated, but that the intensity of the hypoperfused region was rather independent from stimulus intensity. Those findings coincide with the current results since we find also no correlation between amplitude of the BOLD response and the stimulus intensity that was used. Furthermore, these results were also confirmed by a [^{99m}T]HMPAO-SPECT study that investigated the effect of unilateral Poisson distributed hDBS on the regional cerebral blood flow [169]. Taken together, these studies point toward a trend of hippocampal and limbic inhibition of the entire circuit of the targeted structure [160]. Initially, this seems to contradict the increased BOLD responses that were found in our present fMRI study. One possible explanation could be that fMRI is characterized by a temporal resolution in the order of seconds, whereas [^{18}F]FDG-PET is in the order of minutes.

The current study also investigates the reproducibility of whole-brain DBS-induced effects by using *chronically* implanted MR compatible electrodes. It is seen that the BOLD responses from 3 repeated DBS-fMRI experiments with the same DBS parameters remain largely consistent. Other advantages of using chronically implanted electrodes, compared to direct stimulation applied in previous simultaneous hDBS-fMRI studies, are less tissue inflammation due to a post-surgical recovery period of one week and less displacements of the electrode during image acquisition due to fixations with dental cement. Other studies used also chronically implanted electrodes, but they targeted areas different from the hippocampus, such as thalamic structures [139-142].

Seed-based Correlation Analysis vs. General Linear Modelling

Seed-based correlation analysis shows us that for hippocampal stimulation at 90% of the seizure threshold of the individual rat, there are strong and widespread connections (CC > 0.3-0.4) between septal nuclei, hypothalamic mammillary bodies, ipsi- and contralateral hippocampal structures and limbic cortical structures such as ectorhinal, perirhinal, entorhinal, (amygdalo)piriform and cingulate cortex. By means of correlation analysis, those areas show also consistent activation at lower stimulation intensities, although in this case the responses were less widespread and rather restricted to the ipsilateral side. With GLM on the other hand, those limbic regions occasionally display BOLD responses above 10% stimulation, but this was never consistent between different rats and/or different sessions. The distinct findings between these two analysis techniques are probably due to the fact that correlation analysis is a typical reflection of *functional integration* (i.e., which brain regions are connected and interact with each other), whereas statistical mapping based on GLM is rather used to describe *functional specialization* (i.e., which regions respond to a particular, a-priori inserted experimental input). The latter involves that GLM requires the insertion of our stimulation block paradigm, convolved with the basic hemodynamic response function, to determine the "goodness of fit" with the time series of each brain voxel. However, it is well-known that hemodynamic delays can be typically prolonged in regions that are more distal to the stimulated nuclei depending on the connectivity between them [199]. Also the shape of the response function may vary substantially across brain regions and between- and within-subjects, based on the regions targeted and the anesthetics used. Hence, the a-priori insertion of a HRF with a

fixed shape and time delay across subjects and brain regions is likely to underestimate BOLD responses. A solution could be to shift the time-to-peak of an empirical HRF from one region to better estimate HRF's in other brain regions. This would however require data from a large amount of subjects across many regions of interest. Another option is the inclusion of first and second derivatives in the design matrix of GLM, but this will improve magnitude estimates only across a small range of HRF variability (time-to-onset differences from -1 to 1 sec) [199]. Compared to GLM, correlation analysis can directly account for individual voxel-based hemodynamic delays to peak BOLD responses. Nevertheless, both analysis techniques can complement each other: wheareas GLM reveals regions of interest in response to the stimulation, correlation analysis can test hypotheses about the interactions between these regions and the rest of the brain.

Physiological meaning

Because the hippocampal formation is considered as the main structure involved in seizure initiation of refractory TLE, hippocampal depth stimulation has been successfully put forward as a treatment procedure of TLE [4,137,209]. Despite promising results, the pathways that are affected by hDBS as well as its exact mechanism(s) of action remain largely unknown. In epilepsy, four main hypotheses have been proposed to explain these therapeutic mechanism(s): (a) depolarization blockade [205], (b) synaptic inhibition [206], (c) homeostatic downscaling of intrinsic excitability [207] and (d) glial-neuronal interactions leading to a wide range of activation and inhibition effects in the whole brain network [208]. The latter hypothesis supports an important role for the astrocytes – a major type of glia cells – in synaptic transmission. When astrocytes are activated, they can signal further astrocytes through long-distance Ca^{2+}-waves across large networks, contributing to our observed distal (ipsilaterally) effects induced by hDBS. The observed bilateral effects, however, are more likely to be explained by the presence of strong commissural connections between both hemispheres in the rat. It remains unclear whether these bilateral effects of hDBS will be as strong in humans [68,137]. The other hypotheses are far more difficult to link with our DBS-induced activation patterns, since fMRI is rather agnostic regarding the direction of modulation (i.e., excitation or inhibition) [200,201]. Additional cellular studies, such as optogenetics combined with DBS, could provide more insight in what happens on neuronal level during stimulation.

Limitations

The study has a number of limitations. First of all, fMRI may not be able to adequately resolve temporally dynamic DBS-induced changes in cellular activity [202], due to its rather limited temporal resolution. In order to provide complimentary information about the coupling between electrical local field potentials (LFP's) and BOLD responses, electrophysiological recordings in conjunction with fMRI are suggested [203]. Other additional fMRI modalities such as cerebral blood flow (CBF), cerebral blood volume (CBV) and histological analyses, might contribute to better insights into the complex relationship between BOLD signals and the underlying neural activity elicited by a stimulus [204]. This may ultimately result in a more accurate determination of signal sources and spatial specificity.

Secondly, the determination of the stimulation intensity based on the seizure threshold of the individual rat (i.e. thresholding) may act as a confounder since it requires induction of ictal activity. Each rat underwent three DBS-fMRI experiments on different days and a seizure threshold can vary from day to day. However, repeated electric stimulation of limbic structures can result in progressive development of seizure activity in a non-epileptic brain. Therefore, thresholding was performed only once, namely before the first DBS-fMRI experiment of the individual rat. In this way, we can be

confident that the rat is free from induced kindling behaviour or possible adaptation to repeated stimulations.

Thirdly, using fMRI as the analyzing technique can result in a small underestimation of the actual effect induced by hDBS around the site of the electrode. Despite the MR-compatible nature of PtIr, there is still an MR-artefact induced by the electrode and to a lesser extent by the headcap. This results in suppressed responses at the ipsilateral and posterior side of the electrode. Moreover, axial posterior slices are located close to the cerebellum, a region that is characterized by rapid transitions between different tissue types. Hence, there is an increased influence from structural inhomogeneitic brain regions at this site.

A fourth limitation of the study is the small amount of subjects that were used. Despite the fact that our isoflurane anesthesia protocol was successfully conducted in previous studies [90], several animals died in the first twenty minutes being tested under isoflurane. Since electrodes have to be implanted via an invasive surgical procedure, the animal has to recover for at least one week. Secondly, each rat underwent three subsequent DBS-fMRI sessions, each of them taking at least 3 hours with a minimum of 2 hours of recovery between different sessions. Hence, it was not possible to use any more subjects for the study.

Eventually, it is of great importance that the electrode is positioned in the hippocampus with high accuracy. Deviations in electrode placement smaller than the spatial resolution of the MR images may produce large differences in BOLD responses. Adequate electrode positioning could be verified with the aid of (post-mortem) high-resolution anatomical MR images.

Chapter 6

Conclusion

Our results suggest that unilateral Poisson distributed hDBS modulates different brain regions of the limbic network notably the hippocampal formation, (hypo)thalamic nuclei, amygdala, septal areas and the limbic cortex. This means that hDBS exerts both local and distal effects due to neuroanatomical and interhemispheric connections between the structures. Moreover, our results suggest that a certain DBS intensity is required to visualise the effect in more brain regions of the network. Depending on the subject, below such a DBS intensity the BOLD response is very small or insignificant. Stimulation above this intensity results in robust bilateral and widespread responses, probably mediated by commissural fibers.

Further research is necessary in a rodent model of TLE to investigate the correlation between the whole-brain modulatory effects of DBS at a certain stimulus intensity and its therapeutic effects. The determination of an optimal stimulus intensity is of clinical importance since there are still DBS non-responders. Moreover, some responders might benefit from lower stimulation intensities, which is advantageous for the battery life of the pulse generator. In conclusion, our simultaneous DBS fMRI protocol may be a valuable tool to investigate the reproducibility of the DBS-induced effects and to evaluate the effect of various stimulation parameters and targeted brain regions. With regard to data analysis techniques, it is concluded that seed-based correlation analysis is a valuable alternative for GLM to visualize DBS-induced network activity, since it can account for individual voxel-based hemodynamic delays to peak BOLD responses.

References

[1] Arantes PR, Cardoso EF, Barreiros MA, Teixeira MJ, Goncalves MR, Barbosa ER, Sukwinder SS, Leite CC, Amaro E Jr. (2006) **Performing functional magnetic resonance imaging in patients with Parkinson's disease treated with deep brain stimulation.** Mov. Disord., 21, pp. 1154–1162

[2] Albaugh DL, Shih YY (2014) **Neural circuit modulation during deep brain stimulation at the subthalamic nucleus for Parkinson's disease: what have we learned from neuroimaging studies?** Brain Connect, 2014;4:1–14

[3] Ressler KJ, Mayberg HS (2007) **Targeting abnormal neural circuits inmood and anxiety disorders: From the laboratory to the clinic.** Nat Neurosci, 2007;10:1116–24

[4] Boon P, Vonck K, De Herdt V et al. (2007) **Deep brain stimulation in patients with refractory temporal lobe epilepsy.** Epilepsia 48: 1551–1560

[5] Cukiert A, Cukiert CM, Burattini JA & Lima AM (2014) **Seizure outcome after hippocampal deep brain stimulation in a prospective cohort of patients with refractory temporal lobe epilepsy.** Seizure 23, 6–9

[6] Vuilleumier P, Armony JL, Driver J & Dolan RJ (2001) **Effects of attention and emotion on face processing in the human brain: an event-related fMRI study.** Neuron, 30, pp. 829–841

[7] Palmer ED, Rosen HJ, Ojemann JG, Buckner RL, Kelley WM & Petersen SE (2001) **An event-related fMRI study of overt and covert word stem completion.** Neuroimage, 14(1), 182-193

[8] Achard S, Salvador R, Whitcher B, Suckling J, Bullmore E (2006) **A resilient, low-frequency, small-world human brain functional network with highly connected association cortical hubs.** J. Neurosci. 26 (1), 63–72

[9] Fox MD, Raichle ME (2007) **Spontaneous fluctuations in brain activity observed with functional magnetic resonance imaging.** Nat Rev Neurosci 8 (9), 700–711

[10] Williams KA, Magnuson M, Majeed W, Peltier SJ, LaConte SM, Keilholz SD, Hu X (2010) **Comparison of α-chloralose, medetomidine, and isoflurane anesthesia for functional connectivity mapping in the rat.** Magn. Reson. Imaging 28, 995–1003

[11] van den Heuvel, MP, Pol HEH (2010) **Exploring the brain network: A review on resting-state fMRI functional connectivity.** European Neuropsychopharmacology 20 (8), 519–534

[12] Bedny M, Pascual-Leone A, Dodell-Feder D, Fedorenko E, Saxe R (2011) **Language processing in the occipital cortex of congenitally blind adults.** Proc. Natl. Acad. Sci. USA, 108, pp. 4429–4434

[13] Canals S, Beyerlein M, Merkle H, Logothetis NK (2009) **Functional MRI evidence for LTP-induced neural network reorganization.** Current Biology 19:398–403

[14] Kwan P, and Brodie MJ (2000) **Early identification of refractory epilepsy.** New England Journal of Medicine 342: 314–319

[15] Weber R, Ramos-Cabrer P, Wiedermann D, van Camp N & Hoehn M (2006) **A fully noninvasive and robust experimental protocol for longitudinal fMRI studies in the rat**. Neuroimage 29, 1303–1310

[16] Zong X, Fukuda M, Vazquez A, Kim S-G (2013) **Effects of the a2-adrenergic receptor agonist dexmedetomidine on neural, vascular and BOLD fMRI responses in the somatosensory cortex.** Salt Lack City, 2013 20–26 April

[17] Handwerker DA, Ollinger JM, & D'Esposito M (2004) **Variation of BOLD hemodynamic responses across subjects and brain regions and their effects on statistical analyses.** *Neuroimage*, *21*(4), 1639-1651

[18] Hornak JP (2014) **The basics of MRI.** Retrieved October 11, 2014, from http://www.cis.rit.edu/htbooks/mri/index.html

[19] Blink EJ (2004) **MRI Physics.** Retrieved October 11, 2014, from http://mri-physics.net/bin/mri-

physics-en-rev1.3.pdf
[20] Ridgway JP (2010) **Cardiovascular magnetic resonance physics for clinicians: part I.** *Journal of Cardiovascular Magnetic Resonance* 2010, 12:71
[21] Hanson LG (2009) **Introduction to Magnetic Resonance Imaging Techniques.**
[22] Bushberg JT, Seibert JA, Leidholdt EM Jr., Boone JM (2002) **The Essential Physics of Medical Imaging.** (second edition). Philadelphia: Lippincott Williams & Wilkins
[23] **Revise MRI.** (2015) Retrieved October 12, 2014, from http://www.revisemri.com/
[24] Pirko I, Fricke ST, Johnson AJ, Rodriguez M, Macura SI. (2005) **Magnetic resonance imaging, microscopy, and spectroscopy of the central nervous system in experimental animals.** NeuroRx 2: 250–264
[25] van de Ven RC, Hogers B, van den Maagdenberg AM, de Groot HJ, Ferrari MD, Frants RR, ... & Kiihne SR (2007) **T1 relaxation in in vivo mouse brain at ultra high field.** Magnetic Resonance in Medicine, 58(2), 390-395
[26] Kuhl CK, Traber F & Schild HH (2008) **Whole-Body High-Field-Strength (3.0-T) MR Imaging in Clinical Practice Part I.** Technical Considerations and Clinical Applications 1. *Radiology*, *246*(3), 675-696.
[27] Peeters R (2002) **High Resolution Functional Magnetic ResonanceImaging (fMRI) and Image Analysis Performed on a Modelsystem in the Rat: Localisation of Tactile Input-Projections in the Cerebellum.**
[28] Vandenberghe S (2013-2014) **Biomedical imaging.**
[29] **Mayo Clinic** (2015) Retrieved October 15, 2014, from http://www.mayoclinic.org/
[30] Badea CT, Drangova M, Holdsworth DW & Johnson GA (2008) **In vivo small-animal imaging using micro-CT and digital subtraction angiography.** Physics in medicine and biology, 53(19), R319
[31] Bartling SH, Stiller W, Semmler W and Kiessling F (2007) **Small animal computed tomography imaging.** Curr. Med. Imaging Rev. 3 45–59
[32] **Infinity UGent** (2015) Retrieved October 15, 2014, from
http://www.infinityugent.be/research-development/preclinical-small-animal-imaging
[33] Gupta R, Grasruck M, Suess C, Bartling SH, Schmidt B, Stierstorfer K, Popescu S, Brady T, Flohr T **Ultra-high resolution flat-panel volume CT: fundamental principles, design architecture and system characterization.** Eur Radiol. 2006 Jun; 16(6):1191-205
[34] Du LY, Umoh J, Nikolov HN, Pollmann SI, Lee TY, Holdsworth DW (2007) **A quality assurance phantom for the performance evaluation of volumetric micro-CT systems.** Phys Med Biol. 52(23):7087-108
[35] Hyder F, Behar KL, Martin MA, Blamire AM & Shulman RG (1994) **Dynamic magnetic resonance imaging of the rat brain during forepaw stimulation.** Journal of Cerebral Blood Flow & Metabolism, 14(4), 649-655
[36] Lindauer U, Dirnagl U. Füchtemeier M, Böttiger C, Offenhauser N, Leithner C & Royl G (2010) **Pathophysiological interference with neurovascular coupling–when imaging based on hemoglobin might go blind.** Frontiers in neuroenergetics, 2
[37] Matthews, P. M., & Jezzard, P. (2004). Functional magnetic resonance imaging. *Journal of Neurology, Neurosurgery & Psychiatry*, *75*(1), 6-12
[38] Logothetis NK, Pauls J, Augath M, Trinath T & Oeltermann A (2001) **Neurophysiological investigation of the basis of the fMRI signal.** Nature, 412(6843), 150-157
[39] Lauritzen MJ (2005) **Reading vascular changes in brain imaging: is dendritic calcium the key?** Nature Reviews Neuroscience, 6(1), 77-85
[40] Mathiesen C, Caesar K, Akgören N & Lauritzen M (1998) **Modification of activity-dependent increases of cerebral blood flow by excitatory synaptic activity and spikes in rat cerebellar cortex.** J. Physiol. 512, 555–566

[41] Buxton RB, Griffeth VE, Simon AB, & Moradi F (2014) **Variability of the coupling of blood flow and oxygen metabolism responses in the brain: a problem for interpreting BOLD studies but potentially a new window on the underlying neural activity.** Frontiers in neuroscience, 8
[42] Amaro E & Barker GJ (2006) **Study design in fMRI: basic principles.** *Brain and cognition*, *60*(3), 220-232
[43] Siegel AM, Culver JP, Mandeville JB & Boas DA (2003) **Temporal comparison of functional brain imaging with diffuse optical tomography and fMRI during rat forepaw stimulation.** Physics in medicine and biology, *48*(10), 1391
[44] Martin C, Martindale J, Berwick J & Mayhew J (2006) **Investigating neural hemodynamic coupling and the hemodynamic response function in the awake rat.** Neuroimage, *32*(1), 33-48
[45] Ressler KJ, Mayberg HS (2007) **Targeting abnormal neural circuits inmood and anxiety disorders: From the laboratory to the clinic.** Nature neuroscience, 10(9), 1116-1124
[46] Ridgway JP (2010) **Cardiovascular magnetic resonance physics for clinicians: part I.** *Journal of Cardiovascular Magnetic Resonance* 2010, 12:71
[47] Reddy JJM, Prasad V (2005) **Step by Step MRI.** (First edition). New Delhi, India: Jitendar P Vij
[48] Lee SP, Silva AC, Ugurbil K & Kim SG (1999) **Diffusion-weighted spin-echo fMRI at 9.4 T: microvascular/tissue contribution to BOLD signal changes.** Magnetic Resonance in Medicine, 42(5), 919-928
[49] Olman CA & Yacoub E (2011) **Suppl 1: High-Field fMRI for Human Applications: An Overview of Spatial Resolution and Signal Specificity.** The open neuroimaging journal, 5, 74
[50] Norris DG (2012) **Spin-echo fMRI: the poor relation?** Neuroimage, 62, pp. 1109–1115
[51] Wang J, Li L, Roc AC, et al. Reduced susceptibility effects in perfusion fMRI with single-shot spin-echo EPI acquisitions at 1.5 Tesla. Magn Reson Imaging. 2004;22:1–7
[52] Simonsen CZ, Østergaard L, Smith DF, Vestergaard-Poulsen P & Gyldensted C (2000) **Comparison of gradient-and spin-echo imaging: CBF, CBV, and MTT measurements by bolus tracking.** Journal of Magnetic Resonance Imaging, 12(3), 411-416
[53] McRobbie DW, Moore EA, Graves MJ, Prince MR (2006) **MRI from Picture to Proton.** (Second edition). Cambridge: Cambridge University Press
[54] Siero JC, Ramsey NF, Hoogduin H, Klomp DW, Luijten PR & Petridou N (2013) **BOLD specificity and dynamics evaluated in humans at 7 T: comparing gradient-echo and spin-echo hemodynamic responses.** PloS one, 8(1), e54560
[55] van der Zwaag W, Francis S, Head K, Peters A, Gowland P, Morris P & Bowtell R (2009) **fMRI at 1.5, 3 and 7 T: characterising BOLD signal changes.** Neuroimage, 47(4), 1425-1434
[56] Bandettini P (2002) **fMRI: The spatial, temporal, and interpretive limits of functional MRI.** Neuropsychopharmacology: The fifth generation of progress: An official publication of the American College of Neuropsychopharmacology, 343-356
[57] Constable RT. **Challenges in fMRI and its limitations. Chapter 4.**
[58] van der Kolk AG, Hendrikse J, Zwanenburg JJ, Visser F & Luijten PR (2013) **Clinical applications of 7T MRI in the brain.** European journal of radiology, 82(5), 708-718
[59] Yacoub E, Shmuel A, Pfeuffer J, De Moortele V, Adriany G, Andersen P, ... & Hu X (2001) **Imaging brain function in humans at 7 Tesla.** Magnetic Resonance in Medicine, 45(4), 588-594
[60] Hutton C, Bork A, Josephs O, Deichmann R, Ashburner J & Turner R (2002) **Image distortion correction in fMRI: a quantitative evaluation.** Neuroimage, 16(1), 217-240
[61] Kim DH, Adalsteinsson E, Glover GH & Spielman DM (2002) **Regularized higher order in vivo shimming.** Magnetic Resonance in Medicine, 48(4), 715-722
[62] Ramsey NF, Hoogduin H & Jansma JM (2002) **Functional MRI experiments: acquisition, analysis and interpretation of data.** European Neuropsychopharmacology, 12(6), 517-526
[63] Cohen RA, Sweet LH (2011) **Brain Imaging in Behavioral Medicine and Clinical Neuroscience.** New York: Springer

[64] Achard S, Salvador R, Whitcher B, Suckling J, Bullmore E (2006) **A resilient, low-frequency, small-world human brain functional network with highly connected association cortical hubs.** J. Neurosci. 26 (1), 63–72
[65] Fox MD, Raichle ME (2007) **Spontaneous fluctuations in brain activity observed with functional magnetic resonance imaging.** Nat Rev Neurosci 8 (9), 700–711
[66] van den Heuvel MP, Pol HEH (2010) **Exploring the brain network: A review on resting-state fMRI functional connectivity.** European Neuropsychopharmacology 20 (8), 519–534
[67] Kwan P, Brodie MJ (2000) **Early identification of refractory epilepsy.** New England Journal of Medicine 342: 314–319
[68] Supekar K, Musen M, Menon V (2009) **Development of large-scale functional brain networks in children.** PLoS Biol. 2009 Jul; 7(7):e1000157
[69] Minati L, Chan D, Mastropasqua C, Serra L, Spanò B, Marra C, Caltagirone C, Cercignani M, Bozzali MJ (2014) **Widespread alterations in functional brain network architecture in amnestic mild cognitive impairment.** Alzheimers Dis, 2014; 40(1):213-20
[70] Onias H, Viol A, Palhano-Fontes F, Andrade KC, Sturzbecher M, Viswanathan G, de Araujo DB (2013) **Brain complex network analysis by means of resting state fMRI and graph analysis: Will it be helpful in clinical epilepsy?** Epilepsy & Behavior, 38, 71-80
[71] Maccotta L, He BJ, Snyder AZ, Eisenman LN, Benzinger TL, Ances BM, Corbetta M, Hogan RE (2013) **Impaired and facilitated functional networks in temporal lobe epilepsy.** NeuroImage: Clinical, 2, 862-872
[72] Bedny M, Pascual-Leone A, Dodell-Feder D, Fedorenko E & Saxe R (2011) **Language processing in the occipital cortex of congenitally blind adults.** Proceedings of the National Academy of Sciences, 108(11), 4429-4434
[73] Mayberg HS (2009) **Targeted electrode-based modulation of neural circuits for depression.** The Journal of clinical investigation, 119(4), 717-725
[74] Bharath RD (2014) **Functional MRI: Genesis, State of the art and the Sequel.** The Indian journal of radiology & imaging, 24(1), 6
[75] Meyer-Lindenberg A (2012) **The future of fMRI and genetics research.** Neuroimage, 62(2), 1286-1292
[76] Peeters (2002) **High Resolution Functional Magnetic Resonance Imaging (fMRI) and Image Analysis Performed on a Modelsystem in the Rat: Localisation of Tactile Input-Projections in the Cerebellum**
[77] Menon RS, Kim SG, Hu X, Ogawa S, Ugurbil K (1995) **Functional MR imaging using the BOLD approach: Field strength and sequence issues**. In: Le Bihan D, editor. Diffusion and Perfusion Magnetic Resonance Imaging. New York: Raven Press, Ltd.; 1995. p 327-34
[78] **Infinity UGent** (2015) Retrieved October 18, 2014, from http://www.infinityugent.be/research-development/preclinical-small-animal-imaging
[79] Pirko I, Fricke ST, Johnson AJ, Rodriguez M & Macura SI (2005) **Magnetic resonance imaging, microscopy, and spectroscopy of the central nervous system in experimental animals.** NeuroRx, 2(2), 250-264
[80] Uludag K, Muller-Bierl B, Ugurbil K (2009) **An integrative model for neuronal activity-induced signal changes for gradient and spin echo functional imaging.** Neuroimage. 48(2):150-165
[81] Peeters (2002) **High Resolution Functional Magnetic Resonance Imaging (fMRI) and Image**

Analysis Performed on a Modelsystem in the Rat: Localisation of Tactile Input-Projections in the Cerebellum

[82] Burke M, Schwindt W, Ludwig U, Hennig J, Hoehn M. (2000) **Facilitation of electric forepaw stimulation-induced somatosensory activation in rats by additional acoustic stimulation: an fMRI investigation.** Magn Reson Med 2000 Aug;44(2):317-21

[83] Chao THH, Chen JH & Yen CT (2014) **Repeated BOLD-fMRI imaging of deep brain stimulation responses in rats.** PloS one, 9(5), e97305

[84] Masamoto K, Kim T, Fukuda M, Wang P, Kim SG (2007) **Relationship between neural, vascular, and BOLD signals in isoflurane-anesthetized rat somatosensory cortex.** Cereb Cortex 2007;17(4):942–50

[85] Liu ZM, Schmidt KF, Sicard KM & Duong TQ (2004) **Imaging oxygen consumption in forepaw somatosensory stimulation in rats under isoflurane anesthesia.** Magnetic resonance in medicine, 52(2), 277-285

[86] Lukasik VM & Gillies RJ (2003) **Animal anaesthesia for in vivo magnetic resonance.** NMR in Biomedicine, 16(8), 459-467

[87] Watts AD, Herrick IA, McLachlan RS, Craen RA & Gelb AW (1999) **The effect of sevoflurane and isoflurane anesthesia on interictal spike activity among patients with refractory epilepsy.** Anesthesia & Analgesia, 89(5), 1275-1281

[88] Ferron JF, Kroeger D, Chever O & Amzica F (2009) **Cortical inhibition during burst suppression induced with isoflurane anesthesia.** The Journal of Neuroscience, 29(31), 9850-9860

[89] Sommers MG, Pikkemaat JA, Booij LHDJ & Heerschap A (2002) **Improved anesthesia protocols for fMRI studies in rats: The use of medetomidine for stable, reversible sedation.** In Proc Intl Soc Mag Reson Med Vol. 10, p. 393

[90] Chao THH, Chen JH & Yen CT (2014) **Repeated BOLD-fMRI imaging of deep brain stimulation responses in rats.** PloS one, 9(5), e97305

[91] Ueki M, Linn F & Hossmann KA (1988) **Functional activation of cerebral blood flow and metabolism before and after global ischemia of rat brain.** Journal of Cerebral Blood Flow & Metabolism, 8(4), 486-494

[92] Weber R, Ramos-Cabrer P, Wiedermann D, van Camp N & Hoehn M (2006) **A fully noninvasive and robust experimental protocol for longitudinal fMRI studies in the rat.** Neuroimage, 29(4), 1303-1310

[93] Silverman J, Muir W 3rd (1993) A review of laboratory animal anesthesia with chloral hydrate and chloralose. Laboratory animal science 43: 210

[94] Hau J, Schapiro SJ (2011) **Handbook of laboratory animal science.** Boca Raton, FL: CRC Press. v. p.

[95] de Celis Alonso B, Makarova T, Hess A (2011) **On the use of a-chloralose for repeated BOLD fMRI measurements in rats.** Journal of Neuroscience Methods 195: 236–240

[96] Weber R, Ramos-Cabrer P, Wiedermann D, Van Camp N, Hoehn M (2006) **A fully noninvasive and robust experimental protocol for longitudinal fMRI studies in the rat.** NeuroImage 29: 1303–1310

[97] Zhao F, Zhao T, Zhou L, Wu Q & Hu X (2008) **BOLD study of stimulation-induced neural activity and resting-state connectivity in medetomidine-sedated rat.** Neuroimage, 39(1), 248-260

[98] Sinclair MD (2003) **A review of the physiological effects of α2-agonists related to the clinical use of medetomidine in small animal practice.** The Canadian veterinary journal, 44(11), 885

[99] Sinclair MD (2003) **A review of the physiological effects of a2-agonists related to the clinical use of medetomidine in small animal practice.** The Canadian Veterinary Journal 44: 885

[100] Pawela CP, Biswal BB, Hudetz AG, Schulte ML, Li R, Jones SR & Hyde JS (2009) **A protocol for use of medetomidine anesthesia in rats for extended studies using task-induced BOLD contrast and resting-state functional connectivity.** Neuroimage, 46(4), 1137-1147
[101] Zong X, Fukuda M, Vazquez A, Kim S-G (2013) **Effects of the a2-adrenergic receptor agonist dexmedetomidine on neural, vascular and BOLD fMRI responses in the somatosensory cortex**. 2013 20–26 April; Salt Lack City
[102] Mirski MA, Rossell LA, McPherson RW & Traystman RJ (1994) **Dexmedetomidine decreases seizure threshold in a rat model of experimental generalized epilepsy.** Anesthesiology, 81(6), 1422-1428
[103] Vandenberghe S (2014) **Biomedical Imaging.**
[104] Huang S-C, Phelps ME (1986) **Principles of tracer kinetic modeling in positron emission tomography and autoradiography.** In: Phelps M, Mazziotta J, Schelbert H, eds. Positron Emission Tomography and Autoradiography. New York: Raven Press, p 287-346
[105] VERMEULEN S (2012) **Moleculaire en Functionele Beeldvorming met Magnetische Resonantie Beeldvorming (MRI).**
[106] Acton PD, Zhuang H & Alavi A (2004) **Quantification in PET.** Radiologic Clinics of North America, 42(6), 1055-1062
[107] Fischer G, Seibold U, Schirrmacher R, Wängler B & Wängler C (2013) **89Zr, a radiometal nuclide with high potential for molecular imaging with PET: chemistry, applications and remaining challenges.** Molecules, 18(6), 6469-6490
[108] Cherry SR & Gambhir SS (2001) **Use of positron emission tomography in animal research.** ILAR journal, 42(3), 219-232.
[109] Mawlawi O & Townsend DW (2009) **Multimodality imaging: an update on PET/CT technology.** European journal of nuclear medicine and molecular imaging, 36(1), 15-29
[110] Wienhard K, Schmand M, Casey ME, Baker K, Bao J, Eriksson L et al. (2002) **The ECAT HRRT: performance and first clinical application of the new high resolution research tomograph**. IEEE Trans Nucl Sci 2002;49:104–10
[111] Bertolli O, Cecchetti M, Camarlinghi N, Eleftheriou A, Belcari N & Tsoumpas C (2014) **Iterative reconstruction incorporating positron range correction within STIR framework.** EJNMMI Physics, 1(1), 1-2
[112] Jødal L, Le Loirec C & Champion C (2012) **Positron range in PET imaging: an alternative approach for assessing and correcting the blurring.** Physics in medicine and biology, 57(12), 3931
[113] Shibuya K, Yoshida E, Nishikido F, Suzuki T, Tsuda T, Inadama N, ... & Murayama H (2007) **Annihilation photon acollinearity in PET: volunteer and phantom FDG studies.** Physics in medicine and biology, 52(17), 5249
[114] American Clinical Neurophysiology Society (2008) **Guideline One: Minimum Technical Requirements for Performing Clinical Electroencephalography.**
[115] 住吉晃 (2011) **Simultaneous EEG and fMRI recording in small animals.**
[116] Volkmann J, Allert N Voges J, Sturm V, Schnitzler A, Freund HJ (2004) **Long-term results of bilateral pallidal stimulation in Parkinson's disease.** Annals of Neurology 55:871–875
[117] Benabid, A L, Pollak P, Gross C, Hoffmann D, Benazzouz A, Gao D. M, et al. (1994) **Acute and long- term effects of subthalamic nucleus stimulation in Parkinson's disease.** Stereotactic and functional neurosurgery,62(1-4),76–84
[118] Pollak P, Fraix V, Krack P, Moro E, Mendes A, Chabardes S, Kouds A, Benabid AL. (2002) **Treatment results: Parkinson's disease.** Movement Disorders 17(suppl 3):S75–S83
[119] Bereznai B, Steude U, Seelos K, Botzel K (2002) **Chronic high-frequency globus pallidus internus stimulation in different types of dystonia: a clinical, video, and MRI report of six**

patients presenting with segmental, cervical, and generalized dystonia. Mov Disord. 2002 Jan;17(1):138–144
[120] Kupsch A, Benecke R, Muller J, et al. (2006) **Pallidal deep-brain stimulation in primary generalized or segmental dystonia.** N Engl J Med. 2006 Nov 9;355(19):1978–1990
[121] Ngyuen JP, Lefaucher JP, Le Guerinel C, Eizenbaum JF, Nakano N, Carpentier A, Brugieres P, Pollin B, Rostaing S, Keravel Y (2000) **Motor cortex stimulation in treatment of central and neuropathic pain.** Archives of Medical Research 31:263–265
[122] Gray AM, Pounds-Cornish E, Eccles FJ, Aziz TZ, Green AL & Scott RB (2014) **Deep brain stimulation as a treatment for neuropathic pain: a longitudinal study addressing neuropsychological outcomes.** The Journal of Pain, 15(3), 283-292
[123] Malone DA, Jr, Dougherty DD, Rezai AR, et al. (2009) **Deep brain stimulation of the ventral capsule/ventral striatum for treatment-resistant depression.** Biol Psychiatry. 2009 Feb 15;65(4):267–275
[124] Schlaepfer TE, Cohen MX, Frick C, et al. (2008) **Deep brain stimulation to reward circuitry alleviates anhedonia in refractory major depression.** Neuropsychopharmacology. 2008 Jan;33(2):368–377
[125] Lipsman N, Neimat JS, Lozano AM (2007) **Deep brain stimulation for treatment-refractory obsessive-compulsive disorder: the search for a valid target.** Neurosurgery. 2007 Jul;61(1):1–11. discussion 11-13
[126] Greenberg BD, Malone DA, Friehs GM, et al. (2006) **Three-year outcomes in deep brain stimulation for highly resistant obsessive-compulsive disorder.** Neuropsychopharmacology. 2006 Nov;31(11):2384–2393
[127] Boon P, Vonck K, De Herdt V, Van Dycke A, Goethals M, Goossens L, ... & Van Roost D (2007) **Deep brain stimulation in patients with refractory temporal lobe epilepsy.** Epilepsia, 48(8), 1551-1560
[128] Cukiert A, Cukiert CM, Burattini JA & Lima AM (2014) **Seizure outcome after hippocampal deep brain stimulation in a prospective cohort of patients with refractory temporal lobe epilepsy.** Seizure, 23(1), 6-9
[129] Walsh V & Cowey A (2000) **Transcranial magnetic stimulation and cognitive neuroscience.** NaturereviewsNeuroscience,1(1),73–80
[130] Vandenberghe S (2014) **Neuromodulation and imaging.**
[131] Kwan P, and Brodie MJ (2000) **Early identification of refractory epilepsy.** New England Journal of Medicine 342: 314–319
[132] Laxpati NG, Kasoff WS & Gross RE (2014) **Deep brain stimulation for the treatment of epilepsy: circuits, targets, and trials.** Neurotherapeutics, 11(3), 508-526
[133] Wyckhuys T, Geerts PJ, Raedt R, Vonck K, Wadman W & Boon P (2009) **Deep brain stimulation for epilepsy: knowledge gained from experimental animal models.** Acta Neurol Belg, 109(2), 63-80
[134] Canals S, Beyerlein M, Murayama Y, Logothetis N.K (2008) **Electrical stimulation fMRI of the perforant pathway to the rat hippocampus.** Magnetic Resonance Imaging, 26, 2008, pp. 978-986
[135] Wyckhuys T, De Smedt T, Claeys P, Raedt R, Waterschoot L, Vonck K, Van Den Broecke C, Mabilde C, Leybaert L, Wadman W, and Boon P (2007) **High frequency deep brain stimulation in the hippocampus modifies seizure characteristics in kindled rats.** Epilepsia, 48, 2007, pp. 1543-1550
[136] Wyckhuys T, Boon P, Raed R, Van Nieuwenhuyse B, Vonck K, and Wadman W (2010) **Suppression of hippocampal epileptic seizures in the kainate rat by Poisson distributed stimulation.** Epilepsia, 51(11), 2010, pp. 2297-2304

[137] Van Nieuwenhuyse B, Raedt R, Delbeke J, Wadman WJ, Boon P & Vonck K (2014) **In Search of Optimal DBS Paradigms to Treat Epilepsy: Bilateral Versus Unilateral Hippocampal Stimulation in a Rat Model for Temporal Lobe Epilepsy.** Brain stimulation 8, 192-199

[138] Deli G, Balas I, Nagy, Balazs E, Janszky J, Komoly S, Kovacs N (2011) **Comparison of the efficacy of unipolar and bipolar electrode configuration during subthalamic deep brain stimulation.**

[139] Fisher R, Salanova V, Witt T, Worth R, Henry T, Gross R, ... & Graves N (2010) **Electrical stimulation of the anterior nucleus of thalamus for treatment of refractory epilepsy**. Epilepsia, 51(5), 899-908

[140] Andrade DM, Zumsteg D, Hamani C et al. (2006) **Long-term follow-up of patients with thalamic deep brain stimulation for epilepsy.** Neurology. 2006;66(10):1571-1573

[141] Hodaie M, Wennberg R, Dostrovsky JO, Lozano A (2002) **Chronic anterior nucleus stimulation for intractable epilepsy.** Epilepsia 43:603–608

[142] Lega BC, Halpern CH, Jaggi JL & Baltuch GH (2010) **Deep brain stimulation in the treatment of refractory epilepsy: update on current data and future directions.** Neurobiology of disease, 38(3), 354-360

[143] Handforth A, DeSalles AA, Krahl SE (2006) **Deep brain stimulation of the subthalamic nucleus as adjunct treatment for refractory epilepsy.** Epilepsia. 2006;47(7):1239-1241

[144] Velasco F, Carrillo-Ruiz JD, Brito F, Velasco M, Velasco AL, Marquez I et al. (2005) **Double-blind, randomized controlled pilot study of bilateral cerebellar stimulation for treatment of intractable motor seizures.** Epilepsia 2005; 46: 1071-1081

[145] Chkhenkeli SA, Sramka M, Lortkipanidze GS, Rakviashvili TN, Bregvadze ESh, Magalashvili GE et al (2004) **Electrophysiological effects and clinical results of direct brain stimulation for intractable epilepsy.** Clin Neurol Neurosurg 2004; 106: 318-329

[146] Fisher RS & Velasco AL (2014) **Electrical brain stimulation for epilepsy.** Nature Reviews Neurology, 10(5), 261-270

[147] McIntyre CC, Savasta M, Kerkerian-Le Goff L & Vitek JL (2004) **Uncovering the mechanism (s) of action of deep brain stimulation: activation, inhibition, or both.** Clinical neurophysiology, 115(6), 1239-1248

[148] Vandenberghe S (2014) **Neuromodulation and imaging.**

[149] Ranck JJB (1975) **Which elements are excited in electrical stimulation of mammalian central nervous system: A review**. Brain Res 1975;98:417-440

[150] Fenoy AJ, Goetz L, Chabardès S & Xia Y (2014) **Deep brain stimulation: are astrocytes a key driver behind the scene?** CNS neuroscience & therapeutics, 20(3), 191-201

[151] Tawfik VL, Chang SY, Hitti FL, Roberts DW, Leiter JC, Jovanovic S & Lee KH (2010) **Deep brain stimulation results in local glutamate and adenosine release: investigation into the role of astrocytes.** Neurosurgery, 67(2), 367

[152] Kang J, Jiang L, Goldman SA, Nedergaard M (1998) **Astrocyte-mediated potentiation of inhibitory synaptic transmission.** Nat Neurosci 1998;1:683–692

[153] Krautwald K, Min H-K, Lee KH, Angenstein F (2013) **Synchronized electrical stimulation of the rat medial forebrain bundle and perforant pathway generates an additive BOLD response in the nucleus accumbens and prefrontal cortex.** Neuroimage, 77, 14-25

[154] Alvarez-Salvado E, Pallare´s V, Moreno A, Canals S (2014) **Functional MRI of long-term potentiation: imaging network plasticity.** Philosophical Transactions of the Royal Society B: Biological Sciences 369: 20130152

[155] Canals S, Beyerlein M, Merkle H, Logothetis NK (2009) **Functional MRI evidence for LTP-induced neural network reorganization.** Current Biology 19: 398–403

[156] Shih Y YI, Yash TV, Rogers B & Duong TQ (2014) **FMRI of deep brain stimulation at the rat ventral posteromedial thalamus.** Brain stimulation, 7(2), 190-193
[157] Shyu BC, Lin CY, Sun JJ, Chen SL, and Chang C (2004) **Bold response to direct thalamic stimulation reveals a functional connection between the medial thalamus and the anterior cingulate cortex in the rat.** Magnetic Resonance in Medicine, 52, 2004, pp.47-55
[158] Yang PF, Chen YY, Chen DY, Hu JW, Chen J-H, et al. (2013) **Comparison of fMRI BOLD Response Patterns by Electrical Stimulation of the Ventroposterior Complex and Medial Thalamus of the Rat**. PLoS ONE, 8, 2013, e66821
[159] Dunn JF, Tuor UI, Kmech J, Young NA, Henderson AK, et al. (2009) **Functional brain mapping at 9.4 T using a new MRI-compatible electrode chronically implanted in rats.** Magnetic Resonance in Medicine 61: 222–228
[160] Van Den Berge N, Keereman V, Vanhove C, Van Nieuwenhuyse B, van Mierlo P, Raedt R, ... & Van Holen R (2014) **Hippocampal Deep Brain Stimulation Reduces Glucose Utilization in the Healthy Rat Brain.** Molecular Imaging and Biology, 1-11
[161] Hershey T, Revilla FJ, Wernle AR et al (2003) **Cortical and subcortical blood flow effects of subthalamic nucleus stimulation in PD.** Neurology 61(6):816–821
[162] Asanuma K, Tang C, Ma Y et al (2006) **Network modulation in the treatment of Parkinson's disease.** Brain 129:2667–2678
[163] Trost M, Su S, Su P et al (2006) **Network modulation by the subthalamic nucleus in the treatment of Parkinson's disease.** Neuroimage 31:301–307
[164] Goerendt K, Lawrence AD, Mehta MA et al (2006) **Distributed neural actions of anti-parkinsonian therapies as revealed by PET.** J Neural Transm 113:75–86
[165] Karimi M, Golchin N, Tabbal SD et al (2008) **Subthalamic nucleus stimulation-induced regional blood flow responses correlate with improvement of motor signs in Parkinson disease.** Brain 131:2710–2719
[166] Thobois S & Broussolle E (2012) **PET functional imaging of deep brain stimulation in Parkinson's disease.** Journal of Neurolinguistics, 25(2), 133-138
[167] Borghammer P, Cumming P, Aanerud J & Gjedde A (2009) **Artefactual subcortical hyperperfusion in PET studies normalized to global mean: lessons from Parkinson's disease.** Neuroimage, 45(2), 249-257
[168] Klein J, Soto-Montenegro ML, Pascau J, et al. (2011) **A novel approach to investigate neuronal network activity patterns affected by deep brain stimulation in rats.** Jour of Psych Res 45: 927-930
[169] Wyckhuys T, Staelens S, Van Nieuwenhuyse B, et al. (2010) **Hippocampal deep brain stimulation induces decreased rCBF in the hippocampal formation of the rat.** Neuroimage 52(1): 55-61
[170] Lai HY, Albaugh DL, Kao YCJ, Younce JR & Shih YYI (2014) **Robust deep brain stimulation functional MRI procedures in rats and mice using an MRcompatible tungsten microwire electrode.** Magnetic Resonance in Medicine.
[171] Analysis Group, FMRIB, Oxford, UK (2015) **FSLwiki**. Retrieved October 23, 2014, from http://fsl.fmrib.ox.ac.uk/fsl/fslwiki/
[172] Vink M (2014) **fMRI pre-processing and analysis.** Retrieved October 20, 2014, from http://matthijs-vink.com/yahoo_site_admin/assets/docs/fmri_pre-processing_and_analysis_20.16093218.pdf
[173] **Brainvoyager support**. (2014) Retrieved October 20, 2014, from http://support.brainvoyager.com/functional-analysis-preparation/27-pre-processing/279-spatial-smoothing-in-preparation.html
[174] The FIL Methods Group (2013) **SPM8 Manual.** Retrieved October 5, 2014, from http://www.fil.ion.ucl.ac.uk/spm/

[175] **Brainvoyager support**. (2014) Retrieved October 20, 2014, from http://www.brainvoyager.com/bvqx/doc/UsersGuide/Pre-processing/SliceScanTimeCorrection.html
[176] Tsujimura H & Wu HC (2011-12) **1st Level Analysis: Design matrix, Contrasts & Inference.** *Methods for dummies.*
[177] Wager TD. **Contrasts in the GLM and single-subject inference.** Retrieved October 17, 2014, from http://psych.colorado.edu/~tor
[178] Field D. **Thresholding using FEAT.** Retrieved October 17, 2014, from http://www.google.be/url?sa=t&rct=j&q=&esrc=s&source=web&cd=1&ved=0CCQQFjAA&url=http%3A%2F%2Fwww.personal.rdg.ac.uk%2F~sxs02dtf%2FPYM0FM%2Fweek_5_TJ.ppt&ei=8JxYVcvVOoLgywOaxYCIBw&usg=AFQjCNFrSJWNemJtzojBXhN4HLv7xIeYCg&sig2=hwk4Wnp9a2ejA73HcE3F3A&bvm=bv.93564037,d.bGQ
[179] Moeller F, LeVan P & Gotman J (2011) **Independent component analysis (ICA) of generalized spike wave discharges in fMRI: Comparison with general linear model based EEG fMRI.** Human brain mapping, 32(2), 209-217
[180] Robinson SD, Schöpf V, Cardoso P, Geissler A, Fischmeister FPS, Wurnig M ... & Beisteiner R (2013) **Applying independent component analysis to clinical fMRI at 7 T.** Frontiers in human neuroscience, 7
[181] Bordier C, Dojat M & De Micheaux PL (2011) **Temporal and spatial independent component analysis for fMRI data sets embedded in the AnalyzeFMRI R package.** Journal of Statistical Software, 44(9), 1-24
[182] Calhoun VD, Adali T, Hansen LK, Larsen J & Pekar JJ (2003) **ICA of functional MRI data: an overview.**
[183] **Revise MRI.** (2015) Retrieved October 12, 2014, from http://www.revisemri.com/questions/safety/safe_compatible
[184] Jupp B, Williams JP, Tesiram YA, Vosmansky M & O'Brien TJ (2006) **MRI compatible electrodes for the induction of amygdala kindling in rats.** Journal of neuroscience methods, 155(1), 72-76
[185] De Bruyne C (2014) **Design and validation of an MR-compatible stimulation unit.**
[186] Palvin T (2013) Retrieved October 12, 2014, from https://wiki.uib.no/mriwiki/images/b/b8/ProtocolDescriptions.pdf
[187] Macey PM, Macey KE, Kumar R & Harper RM (2004) **A method for removal of global effects from fMRI time series.** Neuroimage, 22(1), 360-366

[188] Hermans E. **SPM8 Starters Guide.**
[189] Siegel AM, Culver JP, Mandeville JB & Boas DA (2003) **Temporal comparison of functional brain imaging with diffuse optical tomography and fMRI during rat forepaw stimulation.** Physics in medicine and biology, 48(10), 1391
[190] Lindquist M (2013) **Statistical methods in functional MRI. Lecture 5: Single-level Analysis.** Retrieved October 15, 2014, from http://www.stat.columbia.edu/~martin/Tools/Lec5-SingleLevel.pdf
[191] Paxinos G & Watson C (2007) **The rat brain in stereotactic coordinates.** (6th edition). Academic Press
[192] Rajmohan V & Mohandas E (2007) **The limbic system.** Indian journal of psychiatry, 49(2), 132
[193] Furtak SC, Wei SM, Agster KL & Burwell RD (2007) **Functional neuroanatomy of the parahippocampal region in the rat: the perirhinal and postrhinal cortices.** Hippocampus, 17(9), 709-722
[194] Becerra L, Pendse G, Chang PC et al (2011) **Robust reproducible resting state networks in the awake rodent brain.** PLoS One 6(10):e25701

[195] Jonckers E, Van Audekerke J, De Visscher G et al (2011) **Functional connectivity of the rodent brain: comparison of functional connectivity networks in rat and mouse.** PLoS One 6(4):e18876
[196] Zhang N, Rane P, Huang W, Liang Z, Kennedy D, Frazier JA & King J. (2010) **Mapping resting-state brain networks in conscious animals.** Journal of neuroscience methods, 189(2), 186-196
[197] Buchhalter JR, Fieles A, Dichter MA (1990) **Hippocampal commissural connections in the neonatal rat.** Dev Brain Res 56:211–216
[198] Swanson LW & Cowan WM (1977) **An autoradiographic study of the organization of the efferet connections of the hippocampal formation in the rat.** Journal of Comparative Neurology, 172(1), 49-84
[199] Handwerker DA, Ollinger JM & D'Esposito M (2004) **Variation of BOLD hemodynamic responses across subjects and brain regions and their effects on statistical analyses.** Neuroimage, 21(4), 1639-1651
[200] Heeger DJ & Ress D (2002) **What does fMRI tell us about neuronal activity?** Nature Reviews Neuroscience, 3(2), 142-151
[201] Logothetis NK (2008) **What we can do and what we cannot do with fMRI.** Nature, 453(7197), 869-878
[202] Younce JR, Albaugh DL & Shih YYI (2014) **Deep brain stimulation with simultaneous FMRI in rodents.** JoVE (Journal of Visualized Experiments), (84), e51271-e51271
[203] Huttunen JK, Gröhn O & Penttonen M (2008) **Coupling between simultaneously recorded BOLD response and neuronal activity in the rat somatosensory cortex.** Neuroimage, 39(2), 775-785
[204] Buxton RB, Griffeth VE, Simon AB & Moradi F (2014) **Variability of the coupling of blood flow and oxygen metabolism responses in the brain: a problem for interpreting BOLD studies but potentially a new window on the underlying neural activity.** Frontiers in neuroscience, 8
[205] Beurrier C, Bioulac B, Audin J, Hammond C (2001) **High-frequency stimulation produces a transient blockade of voltage-gated currents in subthalamic neurons.** J Neurophysiol 2001;85:1351–6
[206] Dostrovsky JO, Levy R, Wu JP, Hutchison WD, Tasker RR, Lozano AM (2000) **Microstimulation-induced inhibition of neuronal firing in human globus pallidus.** J Neurophysiol 2000;84:570–4
[207] van Welie I, van Hooft JA & Wadman WJ (2004) **Homeostatic scaling of neuronal excitability by synaptic modulation of somatic hyperpolarization-activated I-h channels.** Proc Natl Acad Sci (USA) 101: 5123-5128
[208] Vedam-Mai V, van Battum EY, Kamphuis W, et al. (2012) **Deep brain stimulation and the role of astrocytes.** Mol Psych 17: 124–131
[209] Vonck K, Boon P, Claeys P, Dedeurwaerdere S, Achten R & Van Roost D (2005) **Long-term deep brain stimulation for refractory temporal lobe epilepsy.** Epilepsia, 46(s5), 98-99
[210] Spencer SS (2002) **Neural networks in human epilepsy: evidence of and implications for treatment.** Epilepsia. 2002;43:219-27
[211] Vonck K, Sprengers M, Carrette E, Dauwe I, Miatton M, Meurs A ... & Boon P (2013) **A decade of experience with deep brain stimulation for patients with refractory medial temporal lobe epilepsy.** International journal of neural systems, 23(01)

[212] Vonck K, Boon P, Achten E, De Reuck J, Caemaert J (2002) **Longterm amygdalohippocampal stimulation for refractory temporal lobe epilepsy.** Annals of Neurology 19:461–468
[213] Velasco M, Velasco F, Velasco AL, Boleaga B, Jimenez F, Brito F, Marquez I (2000) **Subacute electrical stimulation of the hippocampus blocks intractable temporal lobe seizures and paroxysmal EEG activities.** Epilepsia 41:158–151
[214] Tyrand R, Seeck M, Spinelli L, Pralong E, Vulliémoz S, Foletti G, ... & Boëx C (2012) **Effects of amygdala–hippocampal stimulation on interictal epileptic discharges.** Epilepsy research, 99(1), 87-93
[215] Harnack D, Winter C, Meissner W, Reum T, Kupsch A, Morgenstern R (2004) **The effects of electrode material, charge density and stimulation duration on the safety of high-frequency stimulation of the subthalamic nucleus in rats.** J Neurosci Methods. 2004;138:207-216
[216] Piallat B, Chabardès S, Devergnas A, Torres N, Allain M, Barrat E & Benabid AL (2009) **Monophasic but not biphasic pulses induce brain tissue damage during monopolar high-frequency deep brain stimulation.** Neurosurgery, 64(1), 156-163
[217] McIntyre CC, Savasta M, Walter BL & Vitek JL (2004) **How does deep brain stimulation work? Present understanding and future questions.** Journal of Clinical Neurophysiology, 21(1), 40-50
[218] Stefan H, Theodore WH (2012) **Epilepsy: Basic principles and diagnosis.** (First edition) The Netherlands: Elsevier B.V.

Appendix

Matlab script for correlation analysis

```
clc,clear

%%
path = 'G:\Data\PtIr14\session1';
fn = strcat('G:\Data\PtIr14\session1\');
%% Loading functional data (4D matrix)
scans=150;
fMRI_data=zeros(276,320,49,scans);
fmri_files= dir( 'G:\Data\PtIr14\session1' );
for i=3:152
    header=spm_vol(strcat(fn,fmri_files(i,1).name));
    [fMRI_data(:,:,:,i-2),XYZ]=spm_read_vols(header);
end

%% Masking to maintain only brain slices of interest (mask is drawn in
amira and loaded in NIFTI-format)
brainmask = 'G:\Data\PtIr14\mask_sl15-33.nii';
maskfile =spm_vol(brainmask);
[labels,XYZ]=spm_read_vols(maskfile);
labels_new=zeros(276,320,49);
for i=1:49
labels_new(:,:,i)= labels(:,:,50-i);
end

vol=spm_vol('f00000001.nii');
[beeld,xyz]=spm_read_vols(vol);

for i=1:150
  RR=fMRI_data(:,:,:,i).*labels_new;
    beeld=RR;
    if i<10
       vol.fname=strcat('00',int2str(i),'testloop.nii');
    elseif (i>9)&&(i<100)
       vol.fname=strcat('0',int2str(i),'testloop.nii');
    else
       vol.fname=strcat(int2str(i),'testloop.nii');
    end
  spm_write_vol(vol,beeld);
end

%%
num_voxels = 276*320*49;
time_series=zeros(num_voxels,scans);
%%
for j=1:scans
time_series(:,j)=reshape(fMRI_data(:,:,:,j),num_voxels,1);
end
%%
som_time=sum(abs(time_series),2);
time_series2=time_series(som_time>0,:);
activevoxels=length(time_series2);
```

```
%% Determine mean intensities over all sessions in 1 rat. Calculate
first the mean intensity and standard deviation within each session.
timeseriesmean=mean(time_series2,1);
meanintensity=mean(timeseriesmean);
timeseriesstanddev=std(time_series2,1);
meanstanddev=mean(timeseriesstanddev);
%% Repeat this for each session and save each time as time_series2,
time_series3, time_series4, ...
timeseries_mean_1=(time_series2-meanintensity)/meanstanddev;
%% Take their mean
time_series2=(timeseries_mean_1+timeseries_mean_2+timeseries_mean_3+tim
eseries_mean_4)/4;

%% Determine mean time series of seed
brainmask = 'G:\Data\PtIr14\ROI1.nii';
maskfile =spm_vol(brainmask);
[labels,XYZ2]=spm_read_vols(maskfile);
eln=find(labels==1);
timeseries_ROI_mean=zeros(num_voxels,150);
k=1;
for i=1:num_voxels
    if som_time(i,1)>0
       timeseries_ROI_mean(i,:)=time_series2(k,:);
       k=k+1;
    else
       timeseries_ROI_mean(i,:)=0;
    end
end
Yseed=mean(timeseries_ROI_mean(eln,:),1);

%%
K= zeros(activevoxels+1,scans);
K(1,:)=Yseed;
K(2:activevoxels+1,:)=time_series2;
%%
firstrow=zeros(1,activevoxels);
for i=2:activevoxels+1
    [R2 p] = corrcoef(K(1,:)',K(i,:)');
    %if p(1,2)<0.001
    firstrow(1,i-1)=R2(1,2);
    %else firstrow(1,i-1)=0;
    %end
end
threshold=0;
places=find(abs(firstrow)>threshold);
%%
timeseries_new=zeros(1,num_voxels);
k=1;
for i=1:num_voxels
if som_time(i,1)>0
    timeseries_new(1,i)=firstrow(1,k);
    k=k+1;
else timeseries_new(1,i)=0;
end
end
%%
places2=find(abs(timeseries_new)>threshold);
```

```
[x,y,z]= ind2sub(size(fMRI_data),places2);
%%
NEW=zeros(276,320,49);
for i=1:length(x)
    NEW(x(1,i),y(1,i),z(1,i))=firstrow(1,places(1,i));
end
%%
NEW2=zeros(276,320,49);
for i=1:49
NEW2(:,:,i)=NEW(:,:,50-i);
end

%%
vol=spm_vol('f00000001.nii');
[beeld,xyz]=spm_read_vols(vol);
beeld=NEW2;
vol.fname='Correlatie.Stim90.ROI1.nii';
spm_write_vol(vol,beeld);

%%
figure(1);  imagesc(NEW2(:,:,5));
title('text to include',...
  'FontWeight','bold')
colormap('jet'); colorbar;caxis([-1 1])
set(gca,'XTick',[1:num_voxels])
set(gca,'YTick',[1:num_voxels])
set(gca,'XTicklabel','')
set(gca,'YTicklabel','')
```